UNIVERSIDAD DE INVESTIGACIÓN DE TECNOLOGÍA EXPERIMENTAL YACHAY

Escuela de Ciencias Químicas e Ingeniería

ENGINEERING OF HYBRID CATALYSTS: PHOTO-PIEZO CATALYSIS BASED ON BiFeO₃/BiOCl NANOSHEETS

Trabajo de titulación presentado como requisito para la obtención del título de Magíster en Ciencias Químicas con mención en Ciencia e Ingeniería de los Materiales

Autor:

FIERRO PITA OSCAR ALEXANDER
oscar.fierro@yachaytech.edu.ec

Tutor:

Juan Pablo Saucedo, Ph.D.
jsaucedo@yachaytech.edu.ec

Co-tutor:

Pablo Cisneros-Pérez, Ph.D.
pcisneros@yachaytech.edu.ec

Urcuquí, septiembre 2024

AUTORIA

Yo, **Oscar Alexander Fierro Pita**, con cédula de identidad 1004296008, declaro que las ideas, juicios, valoraciones, interpretaciones, consultas bibliográficas, definiciones y conceptualizaciones expuestas en el presente trabajo; así cómo, los procedimientos y herramientas utilizadas en la investigación, son de absoluta responsabilidad de el/la autora (a) del trabajo de integración curricular. Así mismo, me acojo a los reglamentos internos de la Universidad de Investigación de Tecnología Experimental Yachay.

Urcuquí, septiembre 2024

_____
Oscar Alexander Fierro Pita
CI: 1004296008

AUTORIZACION DE PUBLICACION

Yo, **Oscar Alexander Fierro Pita**, con cédula de identidad 1004296008, cedo a la Universidad de Investigación de Tecnología Experimental Yachay, los derechos de publicación de la presente obra, sin que deba haber un reconocimiento económico por este concepto. Declaro además que el texto del presente trabajo de titulación no podrá ser cedido a ninguna empresa editorial para su publicación u otros fines, sin contar previamente con la autorización escrita de la Universidad.

Asimismo, autorizo a la Universidad que realice la digitalización y publicación de este trabajo de integración curricular en el repositorio virtual, de conformidad a lo dispuesto en el Art. 144 de la Ley Orgánica de Educación Superior.

Urcuquí, septiembre 2024

_____
Oscar Alexander Fierro Pita
CI: 1004296008

DEDICATION

To my Father and Mother, Fabian and Alicia, to my wife Katherine, to my little son Samuel, to my sisters Gaby, Jessy and Betty, to my brother Jairo, and my whole family.

Oscar Alexander Fierro Pita

ACKNOWLEDGEMENTS

To my parents, Fabián and Alicia, I am deeply grateful for being my support and giving me strength when I needed it most. Your unconditional love and support have been my greatest strength. To my wife Katherine and my son Samuel, I owe you a lifetime of joy for your understanding, patience and unconditional love. I am very sorry for having been absent at important moments, but I hope this achievement brings you happiness and pride.

To my sisters Gaby, Betty and Jessy, and my nephews Mile, Nico, Ney and Emy, thank you for your company and constant support. To my brother Jairo, I want to say that this would not have been possible without him. He has been my best friend in the most difficult moments, and although I will never be able to repay everything he did for me, I hope this gives him pride as a small compensation. To my in-laws Angel and Sandra, for their unconditional support, to my brothers-in-law, and to all my family and friends, who have always been a fundamental pillar, I am deeply grateful.

Oscar Alexander Fierro Pita

ABSTRACT

Catalysis is a transcendental process that occupies a fundamental place in chemical synthesis, industry and biological processes. In particular, photocatalysis is an advanced process with a wide field of application in green chemistry, however, the effectiveness of this process is limited to the recombination of the photogenerated hole-electron pair in the catalyst surface. On the other hand, piezo catalysis has a high degree of mechanical energy conversion used for catalytic activity. If these two forms of catalysis are combined, higher catalytic efficiency is expected.

This study aims to synthesize a novel hybrid photo-piezo-catalyst based on $BiFeO_3$ and $BiOCl$. Hybrid catalyst $BiFeO_3/BiOCl$ was synthesized via hydrothermal synthesis from the bismuth precursors with high purity and yield. Chemical composition of the hybrid catalyst was determined by spectroscopic techniques as FTIR, XRD, EDS and XPS demonstrating the presence of Bi, Fe, O, and Cl in a stable material. Morphologic analysis was performed with TEM and SEM microscopies, micrograph shows the presence of nanometric and micrometric structures with morphologies intermediate to those observed for $BiFeO_3$ and $BiOCl$ precursors. Band-gaps of 2.3 eV and 2.78 eV were determined (UV-Vis) for $BiFeO_3$ and $BiOCl$ inside the hybrid material respectively.

The photo-piezo catalysis activity of the hybrid was determined by Rhodamine B degradation assays (UV-Vis) using a homemade photoreactor equipped with a Xenon lamp and an ultrasonic bath. Degradation assays with $BiFeO_3/BiOCl$ hybrid catalyst demonstrated the synergic activity of photo and piezo stimulation as the degradation of Rhodamine reached 98%, whereas 58% and 89% of degradation were reached with piezo catalysis ($BiFeO_3$) and photocatalysis ($BiOCl$) respectively. Scavengers assays with $AgNO_3$, tert-butanol, 2-propanol and formic acid demonstrated that degradation catalysis goes *via* superoxide production as tert-butanol test inhibited 100% of Rhodamine degradation.

Finally, the hybrid material demonstrated effective antibacterial activity against *Escherichia coli*. This capability suggests its potential use in applications requiring antimicrobial properties, such as water purification, medical devices, and coatings, contributing to improved health and safety outcomes.

Keywords: BiOCl, BiFeO3, photocatalysis, piezo catalysis, photo-piezo catalysis.

RESUMEN

La catálisis es un proceso trascendental que ocupa un lugar fundamental en la síntesis química, la industria y en los procesos biológicos. En particular, la fotocatálisis es un proceso avanzado con un amplio campo de aplicación en la química verde, sin embargo, la eficacia de este proceso está limitada a la recombinación del par agujero-electrón fotogenerado en la superficie del catalizador. Por otro lado, la piezo catálisis tiene un alto grado de conversión de energía mecánica utilizada para la actividad catalítica. Si se combinan estas dos formas de catálisis, se espera una mayor eficiencia catalítica.

El objetivo de este estudio es sintetizar un nuevo foto-piezo catalizador híbrido basado en $BiFeO_3$ y $BiOCl$. El catalizador híbrido $BiFeO_3/BiOCl$ se obtuvo con alta pureza y rendimiento mediante síntesis hidrotérmica a partir de los precursores de bismuto. La composición química del catalizador híbrido se determinó mediante técnicas espectroscópicas como FTIR, XRD, EDS y XPS demostrando la presencia de Bi, Fe, O, y Cl en el material estable. El análisis morfológico se realizó con microscopías TEM y SEM, las micrografías muestra la presencia de estructuras nanométricas y micrométricas con morfologías intermedias a las observadas para los precursores de $BiFeO_3$ y $BiOCl$. Se determinaron los band-gaps de 2,3 eV y 2,78 eV (UV-Vis) para $BiFeO_3$ y $BiOCl$ en el interior del material híbrido, respectivamente.

La actividad foto-piezo catalítica del híbrido se determinó mediante ensayos de degradación de Rodamina B (UV-Vis) utilizando un foto reactor casero equipado con una lámpara de Xenón y un baño ultrasónico. Los ensayos de degradación con el catalizador híbrido $BiFeO_3/BiOCl$ demostraron la actividad sinérgica de la foto y la piezo estimulación, ya que la degradación de la rodamina alcanzó el 98%, mientras que con la piezo catálisis ($BiFeO_3$) y la fotocatálisis ($BiOCl$) se alcanzó un 58% y un 89% de degradación respectivamente. Los ensayos con $AgNO_3$, tert-butanol, 2-propanol y ácido fórmico demostraron que la catálisis de la degradación pasa por la producción de superóxido, ya que en el ensayo con tert-butanol se inhibió el 100% de la degradación de la rodamina.

Finalmente, el material híbrido demostró una eficaz actividad antibacteriana frente a *Escherichia coli*. Esta capacidad sugiere su uso potencial en aplicaciones que requieren propiedades antimicrobianas, como la purificación del agua, los dispositivos médicos y los revestimientos, lo que contribuye a mejorar la salud y la seguridad.

Palabras clave: BiOCl, BiFeO3, fotocatálisis, piezo catálisis, foto-piezo catálisis.

I

LIST OF FIGURES

LIST OF TABLES

VI

CHAPTER 1. INTRODUCTION - JUSTIFICATION

1.1. Introduction-justification

Catalysis is a transcendental process that occupies a fundamental place in chemical industry, and in everyday life. Every year, many of researchers present new and novel catalytic processes, as a function of changes in economic models, optimization of production processes, energy transition and in general, in search of the development of the so-called Green Chemistry [1]. In this sense, catalysis is used for many applications such as hydrogen generation, air/water purification, dye degradation, battery manufacturing [2], virus and pathogenic bacteria elimination [3], etc.

In heterogeneous catalysis the most widely used catalytic process today is called photocatalysis [4], [5]. In this process, the catalyst is activated by the irradiation of photons, generated in an electromagnetic radiation source [6], [7], [8]. On the other hand, a catalytic process that is gaining momentum, especially in the last decade, is piezocatalysis. This process is characterized by the activation of the catalyst through the application of ultrasonic vibrations. These can even be generated by the vibration generated by an electric toothbrush [9], [10], [11], [12].

Photocatalysis is an advanced process with a wide field of application in Green Chemistry. However, the effectiveness of this technique is limited to the recombination of the photogenerated hole-electron pair in the catalyst surface [13], [14]. On the other hand, piezo catalysis has a high degree of mechanical energy conversion, which can be used to increase the amount of acid sites in the whole system [12], [15]. If these two features are combined, higher catalytic efficiency is expected. That is, the photocatalyst can generate an electric field inside the photocatalyst, helping the regeneration of the so-called hole-electron pair.

The hybrid photo-piezo catalyst of this research project is synthetized from two catalytic precursors ($BiFeO_3$ and $BiOCl$), which have moderate activity highlight. However, the hybrid catalyst ($BiFeO_3/BiOCl$) must show substantial improvements in the three fundamental characteristics of a catalytic material. That is, it must be superior in efficiency, selectivity and stability [1], [3], [16] compared to its precursors. In relation to efficiency, the hybrid material must have a lower activation energy. Therefore, the reaction rate should be higher. In terms of selectivity, the material must have a structural conformation that allows it to select the best path, in terms of energy investment, to carry out the chemical reaction. Finally, in terms of stability, the hybrid catalyst must not affect the thermodynamic equilibrium of the chemical reaction. However, it must be able to modify the kinetic components of the reaction [17], [18].

The activation of a catalyst is generated by the action of an energy source that can be: electromagnetic radiation, ultrasonic vibrations, enzymatic interactions, etc. The hybrid photo-piezo hybrid can be activated by irradiation with sunlight, ultrasonic vibrations or both simultaneously. This innovative set of features makes the catalyst suitable for a wide range of specific applications, among which water decontamination processes stand out. In this context, the hybrid can catalyze the degradation of complex contaminants such as strong dyes (e.g., Rhodamine B), bacteria harmful to health (e.g., *Escherichia coli*), among others [19], [20].

The need for access to pure water is one of the most discussed topics worldwide [21], [22]. This premise is the fundamental reason for selecting the application of the hybrid catalyst. Water pollution due to effluents contaminated with dyes is one of the major challenges of today. Dyes such as Rhodamine B (RhB) are widely used in the paper industry, in pigment manufacturing, paints, and especially in the textile industry. However, direct contact of the dye with biological organisms can cause skin irritation, eye irritation, and respiratory system issues. Additionally, the presence of dyes in water prevents the passage of light, directly affecting the ecosystem and its biological processes [23], [24], [25].

The presence of pathogenic bacteria in freshwater sources is also a global problem that affects the supply of drinking water and public health. One of the bacteria most commonly found is *Escherichia coli* (*E. coli*), a member of the Enterobacteriaceae family and part of the microbiota of the gastrointestinal tract of warm-blooded animals, such as humans. Global statistics indicate that conditions caused by *E. coli* range from stomach pain, diarrhea, urinary tract infections, respiratory diseases, to bloodstream infections [26], [27]. These conditions are lethal in children under five years old, as around 380,000 infant deaths are reported each year due to this pathogen. It is a high-risk strain since its elimination occurs at a temperature above 70 °C with a pH below 4. This fact renders most conventional sanitization methods ineffective [28].

Based on the descriptions provided in the previous paragraphs, the present thesis aims to focus on the synthesis, characterization, and evaluation of the photocatalytic, piezocatalytic, and photo-piezocatalytic efficiency of the hybrid catalyst ($BiFeO_3/BiOCl$) in the degradation of RhB and *E. coli* bacteria. This will be achieved by utilizing a visible light source and ultrasonic bath as activation sources.

1.2. Problem statement

The synthesis of new semiconductor materials with innovative catalytic properties is of great interest for modern science, especially when referring to the development of Green Chemistry. In this context, the development of photocatalytic and, recently, piezocatalytic chemical reactions have a fundamental importance. If we search in scientific databases, we can find a large number of catalytic reactions at which the catalyst is activated by electromagnetic radiation (photocatalysis) or ultrasonic vibrations (piezocatalysis). However, the interest of the present research is to develop a hybrid catalyst that can be activated with sunlight and ultrasonic vibrations or both simultaneously (photo-piezo catalysis). The hybrid catalyst exhibits significant improvements over its precursors in terms of efficiency, selectivity, and stability. Therefore, it can be used in degradation and disinfection reactions of more complex and resistant contaminants such as *E. coli* bacteria and RhB dye. Thus, the synthesis of the hybrid catalyst not only represents a significant development for the study of photo-piezocatalytic reactions, but also has an impact on the advancement of materials science, water purification processes, and the health of the population in general.

1.3. Objectives

1.3.1. General objective

Synthesize an innovative material with photo-piezocatalytic properties, designed to be activated by irradiation with visible light, ultrasonic vibrations, or both simultaneously, with the aim of efficiently degrading strong dyes such as Rhodamine B (RhB) and eliminating pathogenic bacteria such as *E. coli*, thereby contributing to the improvement materials science, water purification processes and the protection of public health.

1.3.2. Specific objectives

- Synthesize $BiFeO_3$ piezocatalyst, which can be activated by ultrasonic vibrations.
- Synthesize BiOCl photocatalyst, which can be activated by visible light.
- Develop a synthesis process from $BiFeO_3$ and BiOCl catalysts to obtain a hybrid photo-piezo catalyst ($BiFeO_3$/BiOCl) that can be activated with visible light, ultrasonic vibrations, or both simultaneously.
- Characterize the catalyst by XRD, SEM, UV-VIS spectroscopy, and XPS, FT-IR, TGA,
- Perform the photo-piezo catalytic activity of the hybrid in degradation of RhB.
- Perform the antibacterial activity of the hybrid in disinfection of *E. coli* bacteria.

CHAPTER 2. THEORETICAL BACKGROUND

2.1 Advanced oxidation process (AOPs)

Advanced oxidation poses (AOPs) are defined as those oxidation processes in which reactive oxygen species (ROS) are generated from water molecules and molecular oxygen. The species commonly generated by AOPs are: hydroxyl radical ($O\dot{~}H$), superoxide radical ($\cdot O_2^-$) and hydroperoxyl radical ($HOO\cdot$). However, it is also possible for compounds such as hydrogen peroxide to be generated [23], [29]. The ROS present in the medium are sufficient to come into contact with external molecules, organic matter or microorganisms and degrade them faster than natural biological biodegradability. In this context, it is important to note that AOPs are not applied directly to contaminated waters, but to waters that have undergone primary purification processes. This chemical phenomenon makes advanced oxidation processes widely used for the treatment of contaminated water. AOPs stand out from more traditional water purification methods because their mechanism degrades complex molecules and pathogenic microorganisms to less harmful and less noxious compounds such as CO_2 and H_2O. Whereas, common methods such as chemical precipitation by flocculants or direct adsorption are not able to generate disinfection or degradation [30], [31].

2.2.1. Homogeneous and heterogeneous advanced oxidation process (AOPs)

Advanced oxidation processes (AOPs) can be classified into two main groups: heterogeneous advanced oxidation process (HE-AOPs) and homogeneous advances oxidation process (HO-AOPs) [32]. An HO-AOPs system is characterized by the catalyst and the medium being in a single phase. This can be solid, liquid or gas. On the other hand, an HE-AOPs system the catalyst is in a different phase than the medium phase. Therefore, the chemical reactions take place at the interfacial boundary of both phases. This system can be of solid-liquid, liquid-liquid, solid-gas or liquid-gas type [32], [33].

Heterogeneous advances oxidation process are more widely used in the treatment of contaminated water with respect to homogeneous AOPs, as they offer a solution with greater advantages for the removal of recalcitrant organic compounds and emerging contaminants such as dyes and pathogenic bacteria. As mentioned above, in HE-AOPs, the catalyst is in a different phase from the medium. This fundamental characteristic means that its recovery does not require expensive or complex systems. Decanting or filtration are generally very effective methods for catalyst recovery. Additionally, the catalysts synthesized for HE-AOPs are more stable and have a longer lifetime. This makes them a more effective alternative in long-term continuous processes [34], [35].

2.2 Principles of heterogenous advanced oxidation process (AOPs)

In heterogeneous AOPs, the degradation of compounds, organic matter or microorganisms takes place on the surface of the catalyst, which is generally in a solid state. In this process, the catalyst needs to be active, and this activation is carried out using an external energy source. To activate the catalyst, the energy incident on it must necessarily be equal to or greater than the band gap energy (E_g) of the catalyst. In this sense, and according to Braslavsky's official definition, the band gap is defined as: "*Energy difference between the nonconductive and the conductive state of the material. In semiconductors and insulators, it is the energy difference between the bottom of the conduction band (CB) and the top of the valence band (VB)* " [36] Therefore, if this energetic condition is met, we can infer that the catalyst will be activated [37].

Catalyst activation involves an excitation phenomenon that triggers an electronic jump from the valence band (*VB*) to the conduction band (*CB*) of the material. This process generates a positively charged hole in the valence band (h^+) and a negative charge in the conduction band (e^-). This effect is commonly known as electron-hole pair formation (see Figure 1). The number of pairs and the energy required to generate them are two fundamental characteristics to describe the efficiency, stability and selectivity of a catalyst [8], [38].

The role of the catalyst in the HE-AOPs process is fundamental, as it is responsible for reducing the activation energy of a given chemical reaction. Specifically, once the hole-electron pair is formed, the water and oxygen molecules present in the medium are adsorbed onto the surface of the catalyst, due to the attraction generated by the positive charge (h^+) and electrons (e^-) (see Figure 1). This interfacial interaction produces radical species such as hydroxyl radical ($HO^·$), superoxide radical ($·O_2^-$), and hydroperoxyl radical ($HOO·$) [23]. Subsequently, a series of oxidation and reduction (REDOX) reactions are triggered, transforming the present compounds (inorganic compounds, organic matter, or pathogenic microorganisms) into compounds with simpler chemical structures, which are less harmful and, thus, less polluting. When the oxidation is fully achieved CO_2 and H_2O are produced. Once the system has reached its thermodynamic equilibrium and the most stable products have formed, the catalyst is regenerated. This ensures that it does not interfere with the reaction products, is highly stable, selective, and can be reactivated to be applied in another degradation or disinfection process [38], [39].
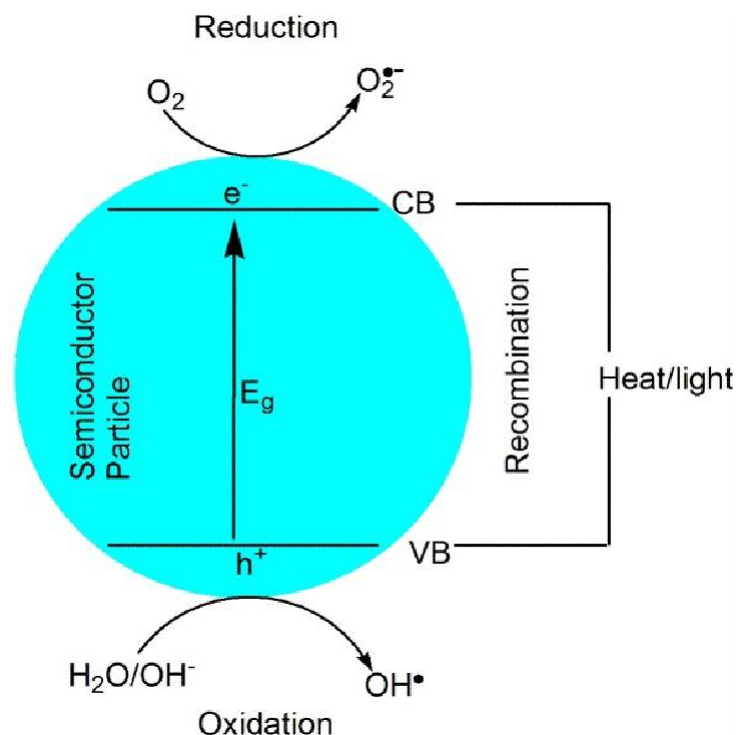
Figure 1. Schematic hole-electron pair formation [40].

2.3.1. Heterogeneous photocatalysis principles

Photocatalysis can be defined as the enhancement in the acceleration of a chemical reaction in the presence of a photo-excited catalyst, where the catalyst is not permanently involved but is regenerated in the final step of the reaction. Infrared, visible, or ultraviolet radiation can be used in photocatalysis, but the energy of the incident photon must be large enough to transfer electrons from the valence band to the conduction band [14], [41]. At this point, it is important to mention that very high energy from photons can be detrimental to a photocatalytic system. This is because very high energies can cause a photolysis effect, which is the degradation of the reactant due to light without the presence or intervention of a photocatalyst [42].

As we have seen so far, when a photocatalyst absorbs photons from a light source, an electronic transition occurs, reaching an excited or activated state. From a structural analysis of the catalyst molecules, the electrons in the HOMO (Highest Occupied Molecular Orbital) increase in energy and are able to migrate to the LUMO (Lowest Unoccupied Molecular Orbital) of a chromophore, also described as the light-absorbing entity [43]. The energy difference between HOMO and LUMO is what we define as the band gap (E_g). As the process continues, the energy absorbed by the electrons is lost almost immediately. Typically, heat emission or photon emission are the most common pathways for this re-emitted energy. A graphical representation helps to understand more deeply the operating principle of photocatalysis (Figure 2). This representation highlights the

formation of the hole-electron pair to reach the excited state. Additionally, it shows how energy loss or emission in the form of heat or photons allows for either bulk recombination or surface recombination of the catalyst [44].
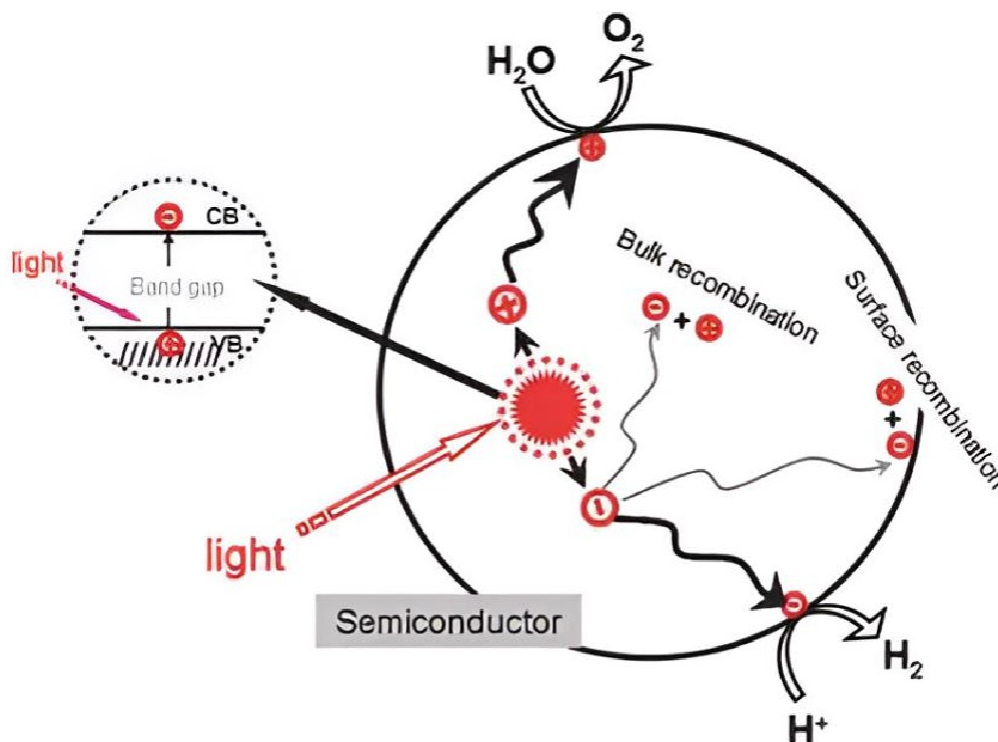
Figure 2. Heterogeneous Photocatalytic mechanism [44]

The active sites generated on the surface of the catalyst surface are in charge of interacting with external compounds, through oxidation and reduction reactions. In addition, it has been reported that the permanence of these sites is in the millisecond range. For this reason, it is possible to infer the radicals formed in the photocatalytic process also have an extremely short lifetime. By comparing the lifetime of an active site with the time required for recombination of volume and surface area in the catalyst, we can deduce that the recombination phenomenon takes longer. However, the shorter the recombination time, the more active, selective and stable the photocatalyst [45], [46].

2.3.1.1. Heterogeneous photocatalytic materials

The photocatalyst to be used in a given chemical reaction is an extremely important aspect in the design of efficient systems for photocatalytic applications. In this context, Table 1 provides a comprehensive compilation of the most relevant photocatalysts, including their band gap energy, synthesis method and crystalline system. These parameters are fundamental to understand and predict the photocatalytic performance of each material. The proper choice of photocatalyst can not only improve the efficiency of photocatalytic reactions, but also optimize the utilization of solar energy as a renewable source. Therefore, the table is applied as an effective guide in the

selection of materials for the present thesis, allowing the identification of the most suitable candidate, depending on our objectives and applications.

Table 1. *Inorganic Materials commonly used as photocatalysts*

Photocatalyst		Crystal system	Eg (Ev)	Synthesis methods	Ref.
TiO$_2$	Rutile	Tetragonal	~3.0	Sol-gel method, Microemulsion, Hydrothermal method	[47]
	Anatase	Tetragonal	~3.2		[47]
ZnO		Hexagonal	~3.2	Sol-gel method, Microemulsion, Hydrothermal method	[47]
CeO$_2$		Cubic	~3.2	Sol-gel method, Microemulsion, Hydrothermal method	[47]
ZrO$_2$		Monoclinic	~5.0	Sol-gel method, Precipitation, Hydrothermal method	[47]
SnO$_2$		Tetragonal	~3.5	Sol-gel method, Hydrothermal method, Solvothermal method, Thermal, decomposition, Molten	[47]
WO$_3$		Monoclinic	~2.7	Sol-gel method, Microemulsion, Hydrothermal method	[47]
α-Fe$_2$O$_3$		Trigonal	~2.2	Sol-gel method, Hydrothermal method, Solvothermal method, Precipitation, Hydrolysis, Ionic	[47]
BiVO$_4$		Monoclinic	~2.4	Sol-gel method, Hydrothermal method, Thermal, decomposition, Organometallic, decomposition, Oxide, melting, Hydrolysis	[47]
SrTiO$_3$		Cubic	~3.4	Sol-gel method, Hydrothermal method	[47]
Ag$_3$PO$_4$		Cubic	~2.4	Hydrothermal method, Precipitation, Ion exchange, Oxidation.	[47]
CdS		Hexagonal	~2.4	Sol-gel method, Hydrothermal method, Solvothermal method, Aqueous chemical	[47]
BiOCl		Tetragonal	~ 2.8	Solvothermal method	[48], [49]

2.3.1.2. BiOCl as photocatalyst

Bismuth oxychloride (BiOCl) stands out from the aforementioned materials, mainly due to its ability to be activated by visible light (400 nm - 700 nm). Additionally, it is synthesized by solvothermal method and has bismuth nitrate pentahydrate (Bi(NO$_3$)* 5H$_2$O). The synthesis process by the solvothermal method is carried out at a specific temperature, commonly around 160 °C, resulting in the formation of well-defined crystals of high purity, fundamental characteristics for the optimum photocatalytic performance of the material. Additionally, this semiconductor has been extensively characterized and evaluated in dye degradation systems such as RhB and bacteria such as *E. coli*, with positive results [50], [51].

BiOCl catalyst exhibits a band gap energy band within the visible light range, generally 2.8 eV (442 nm), which allows it to efficiently absorb photons from this region of the electromagnetic spectrum. This property makes it the ideal candidate for the photocatalytic applications we seek, since it is possible to harness solar energy as a renewable energy source [52], [53], [54].

2.3.2. Heterogeneous piezocatalysis principles

Piezocatalysis is defined as the change in the rate of a chemical reaction in the presence of a piezo activated, non-center symmetric catalyst. Its importance lies in the fact that it is a very recent technique, which has generated interesting results in terms of catalytic dye degradation, hydrogen generation, and, bacterial disinfection. The piezocatalysis phenomenon stands out when it refers to the activation energy of the catalyst. This energy can come from a piezoelectric effect (transformation of mechanical energy into electric energy) [55]. It can also come from ultrasonic vibrations, from natural movements produced by wind or waves, and even the activation of piezocatalyst through the redundant vibrations of industrial systems has been reported. Therefore, this technique can be considered as a green catalysis process, which favors the care of the environment [55], [56].

Piezocatalysis is a recent and novel technique in the scientific world. Therefore, the mechanism by which this process is carried out is under constant analysis and development. In this section, two outstanding mechanisms are analyzed, which explain how the flow of electrons from the valence band to the conduction band is developed, in an analogous way to the mechanism that proceeds in a photocatalytic process. That is, by means of piezocatalysis it is possible to directly convert mechanical energy into chemical energy, resulting in piezoelectric polarization. In this way, the polarized charges and the intrinsic free charges of the catalyst generate the consecutive oxidation and reduction reactions (see Figure 3) [57], [58].
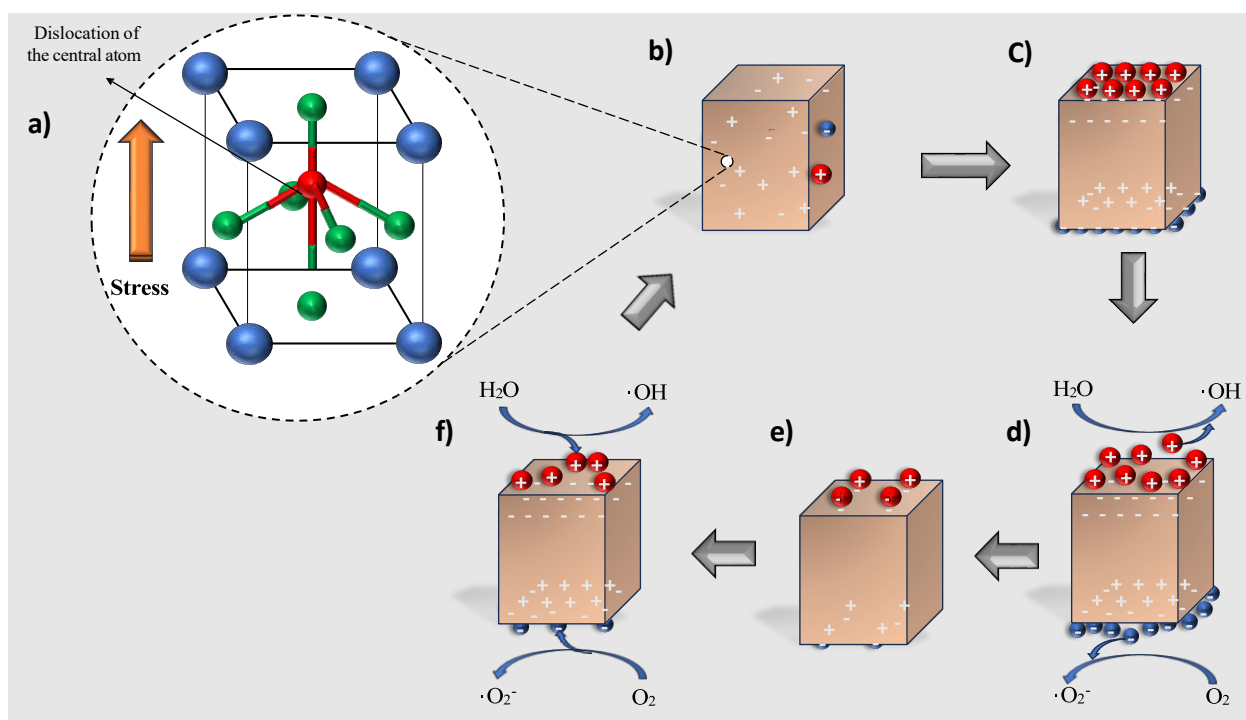
Figure 3. *Heterogeneous Piezocatalytic mechanism* [57]

Figure 3 a) represents the crystal structure of the piezocatalytic material, highlighting the remarkable ability of the central atom to dislocate under stress generated by ultrasonic vibrations or mechanical energy, generating a density of positive and negative charges. Therefore, this dislocation of the central atom is a crucial event in the piezocatalytic process, since it is fundamental for the activation of the material and the initiation of the reactions. Subsequently, in Figure 3 b), it is observed how this dislocation leads to the polarization of the material, resulting in a flow of positive and negative charges. This phenomenon is essential for initiating piezocatalytic reactions, as it creates an environment conducive to interaction with molecules in the medium [57], [59]. (Figure 3 c) represents the moment when the electrostatic equilibrium of the material is reached, with the formation of two very well-defined poles, which compensate the opposite charges. This equilibrium is crucial to maintain the stability of the material during the piezocatalytic process. Figure 3 d) shows the interaction between the charges of the material and the water and oxygen molecules, leading to the generation of radicals such as hydroxyl ($\cdot$OH) and superoxide ($\cdot O_2^-$).

These radicals are responsible for the oxidation and reduction reactions of dyes, bacteria or organic matter. (Figure 3 e) represents the modification of the electrostatic balance when the material is under maximum stress, which intensifies the piezocatalytic activity of the material. Finally, (Figure 3f) shows how the ions of the medium compensate the charges of the material, restoring its electrostatic balance and stability. Once the piezocatalytic reaction has concluded and the vibration source has been turned off [57], [58], [59].

2.3.2.1. Heterogeneous piezocatalytic materials

The piezocatalyst to be used in a system, whether for dye degradation or bacterial disinfection, is a crucial point in the design of efficient systems. In this context, Table 2 presents a detailed compilation of the most relevant piezocatalyst, highlighting their band gap energy, catalytic conditions and their synthesis method. These data are essential to understand and anticipate the piezocatalytic performance. The proper selection of the piezocatalyst can not only enhance the efficiency of the piezocatalytic reactions, but also optimize the synthesis of a hybrid catalyst, such as the one required in the present thesis.

Table 2. Materials commonly used as piezocatalyst

Piezocatalyst	Eg (Ev)	Catalytic conditions	Synthesis method	Ref
$KNbO_3$ nanosheets	~ 3.22	Xenon lamp (300 W) + ultrasound (40 kHz, 110 W)	Transitional solid state synthesis	[60], [61]
$BiFeO_3$ nanowires	~ 2.5	Xenon lamp (300 W) + ultrasound (132 kHz, 80 W)	Colloidal dispersion capillary force-induced template-assisted synthesis	[60], [62]
ZnO nanowires	~ 3.37	Mercury lamp (50 W) + swing	Hydrothermal synthesis	[60], [63], [64]
$NaNbO_3$ nanorods	~ 2.89	UV light + ultrasound (40 kHz, 100 W)	Hydrothermal synthesis	[60], [65]
$BaTiO_3$ nanowires	~ 3.2	Ultrasound (40 kHz, 80 W)	Hydrothermal synthesis	[60], [66]
ZnO nanorods	~ 3.3	UV irradiation (24 W) + ultrasound (40 kHz, 150 W)	Gas-phase synthesis on oxidized silicon substrates (550°C)	[60], [67]
$Pb(Zr,Ti)O_3/TiO_2$	~ nd	LED (15 mW·cm^{-2}) + stirring	Solvothermal alcoholysis synthesis of hierarchical TiO_2	[60], [68]
$ZnSnO_3$ nanowires	~ 3.7	Xenon lamp (150 W) + Ultrasound (40 kHz, 250 W)	Single-step hydrothermal synthesis	[60], [69]
<u>$BiFeO_3$ nanosheets</u>	<u>~ 2.2</u>	<u>Ultrasonic (40 kHz, 100 W)</u>	<u>Solvothermal synthesis</u>	[60], [70]
$MAPbI_3$	~ 1.57	Tungsten−halogen lamp (500 W) + ultrasound	Colloidal dispersion capillary force-induced template-assisted synthesis	[60], [71]
Bi_4NbO_8X (X = Cl, Br)	~ 2.48	Xenon lamp (300 W, $\lambda > 420$ nm) + ultrasound (240 W)	Synthesis by flux method with NaCl and KCl (1:1) as molten salts	[60], [72]

2.3.2.2. BiFeO₃ as piezocatalyst

Bismuth ferrite (BiFeO$_3$) has been selected for this research project due to its specific properties and characteristics. Similar to BiOCl, BiFeO$_3$ is synthesized by the solvothermal method. An important detail is that in this case the synthesis is carried out at a slightly higher temperature (180 °C) [73]. In addition, they share another common feature, which is that bismuth nitrate pentahydrate (Bi(NO$_3$)* 5H$_2$O) is used as the main reagent in their synthesis [74], [75]. Given that BiFeO$_3$ shares fundamental characteristics with BiOCl and the aim is to synthesize a hybrid catalyst that improves the synergy between both materials, its selection is considered crucial to improve the efficiency and performance of the hybrid catalyst. In addition, there are other materials that can be activated with ultrasound for piezocatalysis applications (see Table 2). However, it should be mentioned that the synthesis of a hybrid catalyst from two materials with different synthetical methodologies and reagents presents even stronger challenges.

The activation of bismuth ferrite by ultrasonic vibrations represents a crucial aspect in its application in piezocatalysis. With a band gap of 2.2 Ev (563.57 nm), this property makes it particularly suitable for the generation of reactive species under ultrasound stimulation. In this context, it has been reported that BiFeO$_3$ can be efficiently activated with ultrasound at a frequency of 40 kHz and at a power of 100 W, which can be generated by a typical ultrasonic bath. The combination of the piezocatalytic capability of BiFeO$_3$ with its activation by ultrasound positions it as a promising candidate for applications in green chemistry and innovative catalytic [73].

2.3.3. Heterogeneous photo-piezo catalysis principles

Photo-piezo catalysis is defined as the change in the rate of a chemical reaction in the presence of an activated photo-piezo catalyst. Under this premise, ferroelectric materials acquire great relevance, due to their electrochemical properties, but especially to their catalytic photo-piezo properties. For this reason, although this topic is relatively new, its field of application is extremely wide, including dye degradation, or bacterial disinfection. This is because, as in a photocatalytic process or a piezocatalytic process, the photo-piezo catalysis involves highly reactive radical species, such as hydroxyl and superoxide [76].

The combination of photocatalysis and piezocatalysis is proposed as a method to optimize the process of photogeneration of reactive oxygen species (ROS). This is because it has been proven that when a photocatalyst is placed in the presence of an external or internal electric field, it can alter the energy landscape either at the interface or inside the photocatalyst. Because of this effect, the formation of the hole-electron pair is favored, increasing the reaction yield and avoiding

reorganization in the material matrix. On the other hand, by analyzing the interaction between the electrons and the negative charges of the matrix, it has been determined that the formation of the hole-electron pair also promotes the transfer of these negative charges to the right ends, favoring the formation of ROS. Thus, photo-piezo catalysis is defined as a synergy between two materials that enhance their properties to form reactive species, increasing the performance in degradation or disinfection reactions [77], [78].

A plausible mechanism for this effect is shown in Figure 4. The process starts when the material is exposed to ultrasound, with which the catalyst can generate an induced electric field due to the dislocation of the central atom (piezocatalysis principle). Subsequently, the positive and negative charges migrate along the matrix to generate the poles (polarization). The generated charges interact with water and molecular oxygen molecules to generate radicals, especially hydroxyl and superoxide radicals. Simultaneously, the photons emitted by the visible light source cause the electrons in the valence band to increase their energy, jumping towards the conduction band (principle of photocatalysis). This generates the electron-hole pair, which, when in contact with water and molecular oxygen, it generates the radical species mentioned above [78], [79].

As we defined photocatalysis in a previous section, it was noted that the recombination and migration of the hole-electron pair is a slow process (seconds), compared to the time it takes for the formation of the radicals (milliseconds). This process is enhanced when using a catalytic photo-piezo catalyst. This argument is supported by the fact that the polarization of the material, as a result of the dislocation of the central atom, generates positive and negative charges. The latter interacts with the electrons displaced by the photocatalytic effect, by means of repulsion forces (equal charges repel each other). This effect favors the flow and migration of electrons, increasing the number of positive holes in the valence band and, therefore, the number of electrons in the conduction band. In addition, the need for surface recombination is eliminated, since the space for electron flow increases considerably. Thus, the process generates a greater number of active sites, a greater number of radical species and consequently a greater degradation or disinfection effect (Figure 4) [80], [81], [82], [83].
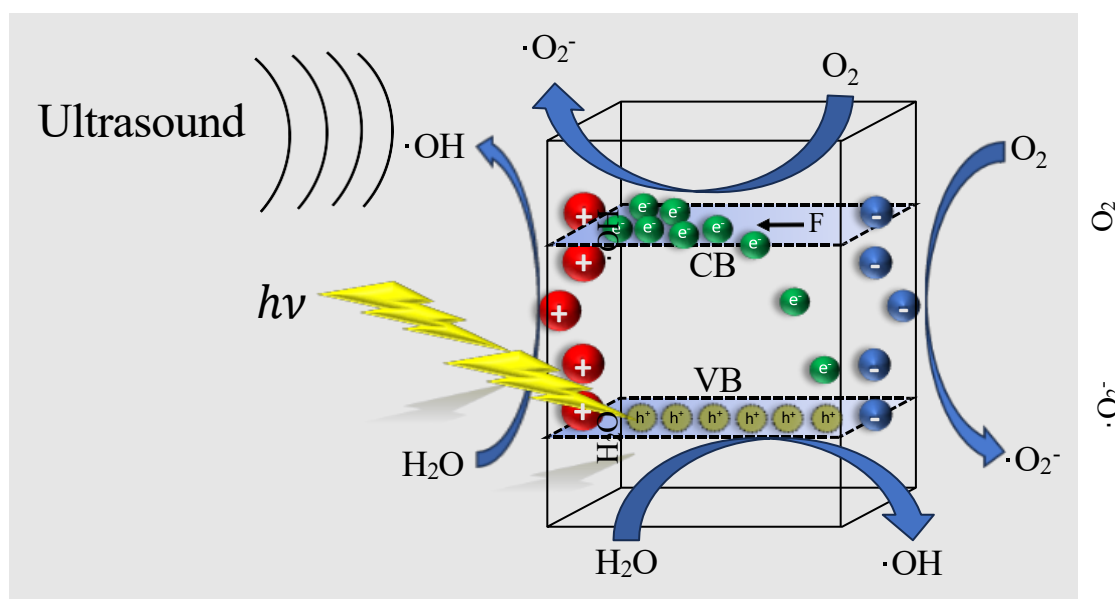
Figure 4. *Heterogeneous Photo-piezo catalytic mechanism in the hybrid catalyst*

It is interesting to analyze also the effect of the energy sources (ultrasound and visible light) separately, in order to have a solid theoretical foundation on the hybrid material. Regarding the principle of operation of the hybrid catalyst, exposed only to ultrasound, Figure 5a shows how the polarization effect of the matrix is produced, caused by the dislocation of the central atom. Subsequently, the positive and negative charges are responsible for generating ROS which, when interacting with organic matter, dyes or bacteria, generate the degradation or disinfection effect. However, it can be observed that the valence band electrons remain in place. Therefore, the so-called hole-electron pair is not generated. In other words, the photocatalysis effect is not evident, but only the piezocatalytic effect [84], [85].

When the hybrid catalyst is stimulated by visible light (Figure 5 b), it is not polarized. That is to say, the separation of positive and negative charges that migrate towards the ends of the matrix is not generated. However, what happens is that the incident photons on the material are absorbed by the electrons in the valence band. These electrons consequently increase their energy and jump to the conduction band, generating the hole-electron pair. This effect, typical of photocatalysis, is responsible for generating ROS to trigger oxidation and reduction reactions of organic matter, dyes and bacteria. [77], [86], [87].
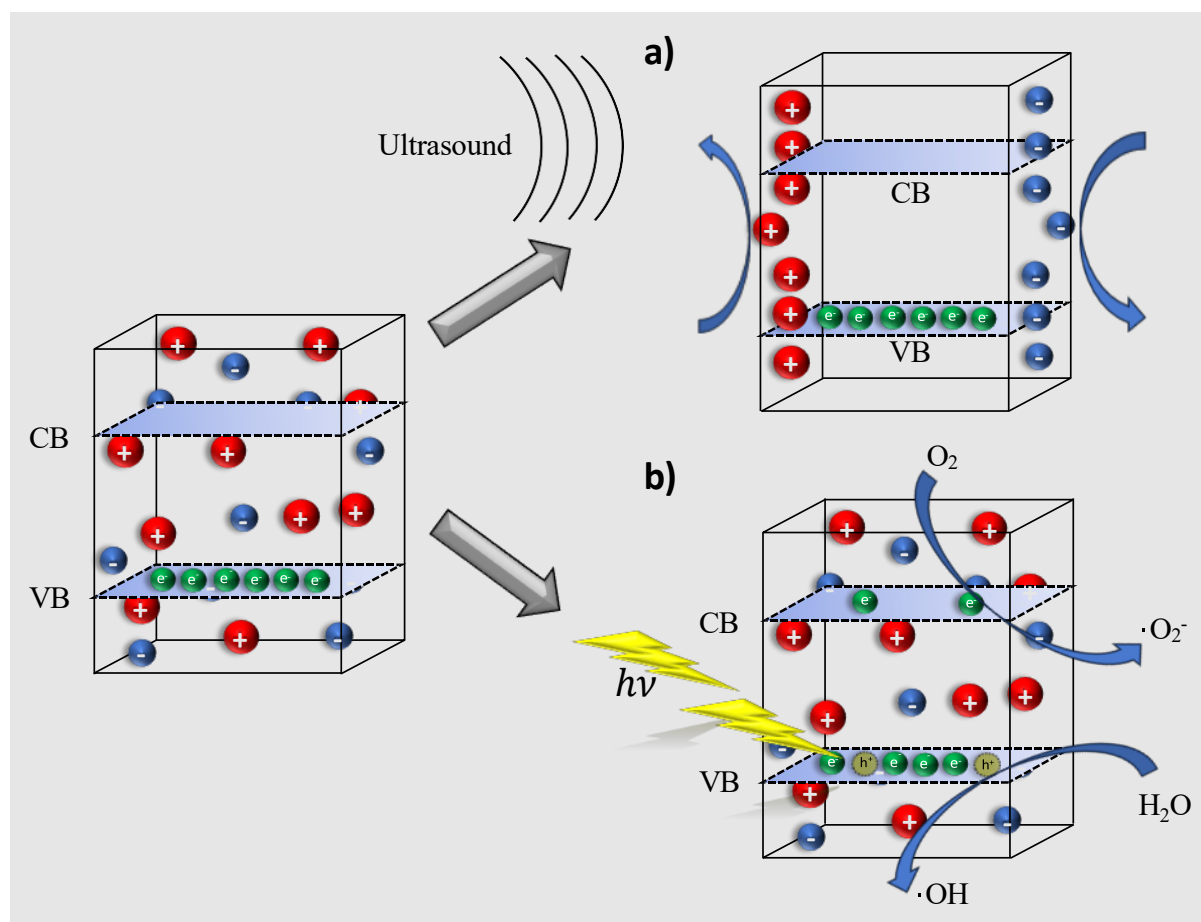
Figure 5. *Heterogeneous Photocatalytic and Heterogeneous Piezocatalytic mechanisms in the hybrid catalyst*

2.3.3.1. Heterogeneous photo-piezo catalytic materials

Photo-piezo catalysis is a recent technique with a high scientific and environmental interest. For this reason, the number of publications on this topic is still conservative. In table 3 is shown a list of tested materials with catalytic photo-piezo properties, whose importance lies in the catalyst concentration and activation conditions. With this information, a theoretical basis is obtained to employ a suitable methodology, which can be used as a guide to the hybrid catalyst synthesized in this thesis. This approach could lead to innovative solutions for future energy production and environmental remediation.

Table 3. *Materials reported as photo-piezo catalysts for rhodamine (RhB) degradation*

Piezocatalyst	Dye	Catalytic conditions	Initial dye concentration	Ref
0.01Li-BT NSs	RhB	Light: 300 W Xe lamp Ultrasonic: 40 kHz, 100W	5 mg/L	[80]

0.02La-BT NSs	RhB	Light: 300 W Xe lamp Ultrasonic: 40 kHz, 100W	5 mg/L	[80]
$Bi_{0.5}Na_{0.5}TiO_3$ nanorods	RhB	Light: 300 W Xe lamp Ultrasonic: 28 kHz, 200W	5 mg/L	[80]
$BiFeO_3$ nanowires	RhB	Light: 300 W Xe lamp Ultrasonic: 132 kHz, 80W	4 mg/L	[80]
Bi_2WO_6/g-C_3N_4/ZnO	RhB	Light: 100 W Xe lamp Ultrasonic: 40 kHz, 120 W	5 mg/L	[80]
Cl doped ZnO nanorods	RhB	Light: 300 W Xe lamp Ultrasonic: 40 kHz, 100W	10 mg/L	[80]
Au/$AgNbO_3$ nanocubes	RhB	Light: 300 W Xe lamp Ultrasonic: 40 kHz, 110W	10 mg/L	[80]
$BiOIO_3$ nanoparticles	RhB	Light: 150 W Xe lamp Ultrasonic: 40 kHz, 120W	5 mg/L	[80]
NBT-BNT@ Ag powders	RhB	Light: 300 W Xe lamp Ultrasonic: 40 kHz, 200W	10 mg/L	[80]
$Bi_4Ti_3O_{12}$ nanoplates	RhB	Light: 300 W Xe lamp Ultrasonic: 40 kHz, 300W	5 mg/L	[80]
BT@TiO_2 nanowires	RhB	Light: 300 W Xe lamp Ultrasonic:45 kHz, 200 W	5 mg/L	[80]

2.3.3.2. $BiFeO_3$/BiOCl hybrid catalyst

The hybrid catalyst ($BiFeO_3$/BiOCl), is synthesized from the two components selected in the previous sections: the photocatalyst is bismuth oxychloride (BiOCl) and the piezocatalyst is bismuth ferrite ($BiFeO_3$). Consequently, the hybrid catalyst can be activated in multiple ways. On the one hand, it can be activated by visible light, in the wavelength range from 400 nm to 700 nm. On the other hand, it can also be activated by ultrasound, whose conditions, tested by literature, are using a frequency of 40 kHz and an approximate power of 120 W. These characteristics allow environmentally friendly catalytic processes, useful for the industry. Since, sunlight can be the energy source that activates the photocatalytic function. Since, the vibrations generated by industrial equipment can carry out the activation of the piezocatalyst [74].

The selection of the precursors is not a random work, but they were selected because they coincide in several aspects such as: the synthesis method is solvothermal, the main reagent is

bismuth nitrate pentahydrate and the synthesis temperatures are slightly different. These characteristics make the hybrid catalyst have a different chemical structure with respect to its precursors. Additionally, parameters such as band gap, crystal structure, atomic bonds and macroscopic characteristics are also notably different. In terms of chemical activity, the hybrid has a higher capacity for active site formation, and thus a higher ROS formation. This makes the material suitable for the treatment of complex structures and more resistant microorganisms. Additionally, the synthesized hybrid catalyst has not been reported previously, which significantly increases its scientific interest and potential for this and future research.

CHAPTER 3. METHODOLOGY

3.1 Materials

Bismuth nitrate pentahydrate (Bi(NO$_3$)* 5H$_2$O), ferric chloride hexahydrate (FeCl$_3$*6H$_2$O, 98%), ferric nitrate nonahydrate (Fe(NO$_3$)$_3$* 9H$_2$O, 98%), ethylene glycol (C$_2$H$_6$O$_2$, 99%), ammonia hydroxide (NH$_4$OH, 25%), sodium hydroxide (NaOH, %98), potassium chloride (KCl, 98%), ethanol (C$_2$H$_5$OH, %60)), Rhodamine B (RhB, 99%), were purchased from Sigma Aldrich. The deionized water (DI) was produced in a Millipore water purification system.

3.2 Synthesis methods

3.2.1. Synthesis of BiOCl microsheets

BiOCl microsheets were synthesized by the classical solvothermal method. First, 0.49 g Bi(NO$_3$)* 5H$_2$O were dissolved in 21 mL of DI. Then, 0.37 g KCl were added with vigorous stirring for 1 hour (see Figure 6 a)). After this time, the solution was placed in an autoclave reactor, with a volume of 28 mL, and heated in an oven at 160 °C for 24 hours. Then, the reactor was removed from the oven and allowed to cool for approximately 10 hours to reduce the internal pressure and remove the Teflon capsule (see Figure 6 b and 6 c). Subsequently, the synthesized product was centrifuged at 9000 rpm for 1 minute (see Figure 6.d). The precipitate was rinsed three times with deionized water and C$_2$H$_5$OH, respectively (see Figure 6 e). Finally, the product was dried in an oven at 60 °C for 6 hours (see Figure 6 f) and was stored in an amber container and placed in a desiccator, to avoid activation by visible light or structural alterations by humidity.
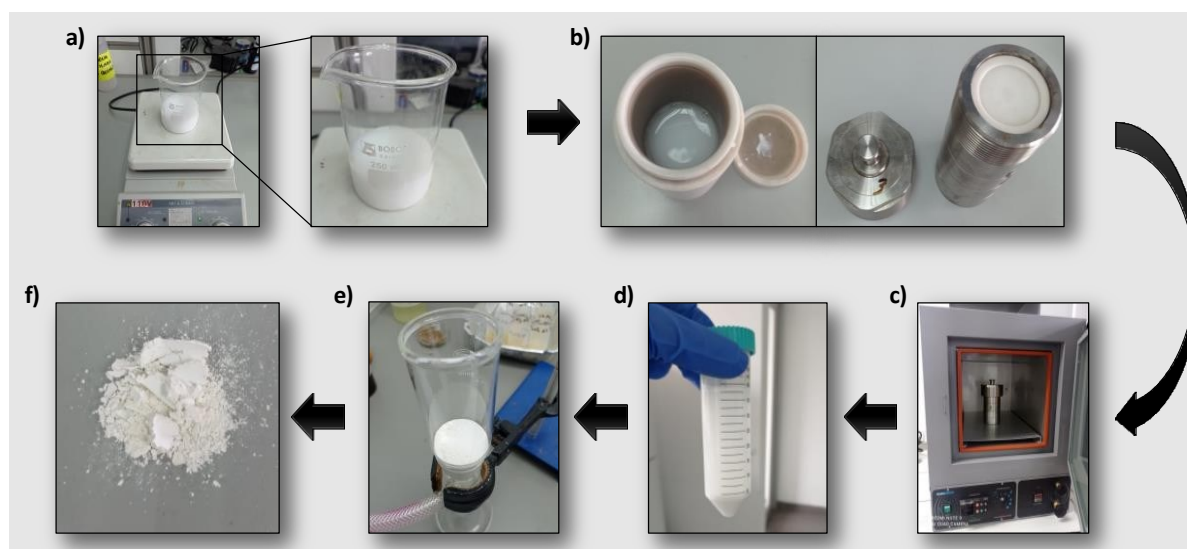
Figure 6. *Scheme of the solvothermal synthesis of BiOCl*

3.2.2. Synthesis of BiFeO₃ nanosheets

BiFeO₃ nanosheets, like the compound in the previous section, were also synthesized by the classical solvothermal method. The synthesis started by dissolving 3.63 g of $Bi(NO_3)* 5H_2O$ in 45 mL of $C_2H_6O_2$, with vigorous stirring (see Figure 7 a). Next, 2.04 g $(NO_3)* 9H_2O$ and 300 mL of DI were added (see Figure 7 b). The next step was to adjust the pH to a value of 11 by adding NH_4OH, 25% dropwise, (Figure 7 c). Subsequently, the obtained solution was centrifuged at 9000 rpm for three minutes (see Figure 7 d). Then, the collected precipitate was washed several times with distilled water and C_2H_5OH (see Figure 7 e). Then, the precipitate was placed again in a beaker, and 90 mL of 5 M NaOH were added with constant stirring (Figure 7 f).

Continuously, the resulting solution was transferred to an autoclave reactor, with a volume of 150 mL, and was heated in an oven at 180°C for 48 hours. After this time, the reactor was removed from the oven and allowed to cool for approximately 10 hours (see Figure 7. g)). The synthesized product was centrifuged at 9000 rpm for one minute and washed three times with distilled water (Figure 7. h). Then, the precipitate was dried in an oven at 60 °C for 12 hours. Finally, the dried solid is calcined at 400 °C for exactly 2 hours to achieve the desired molecular structure (see Figure 7 i and j).
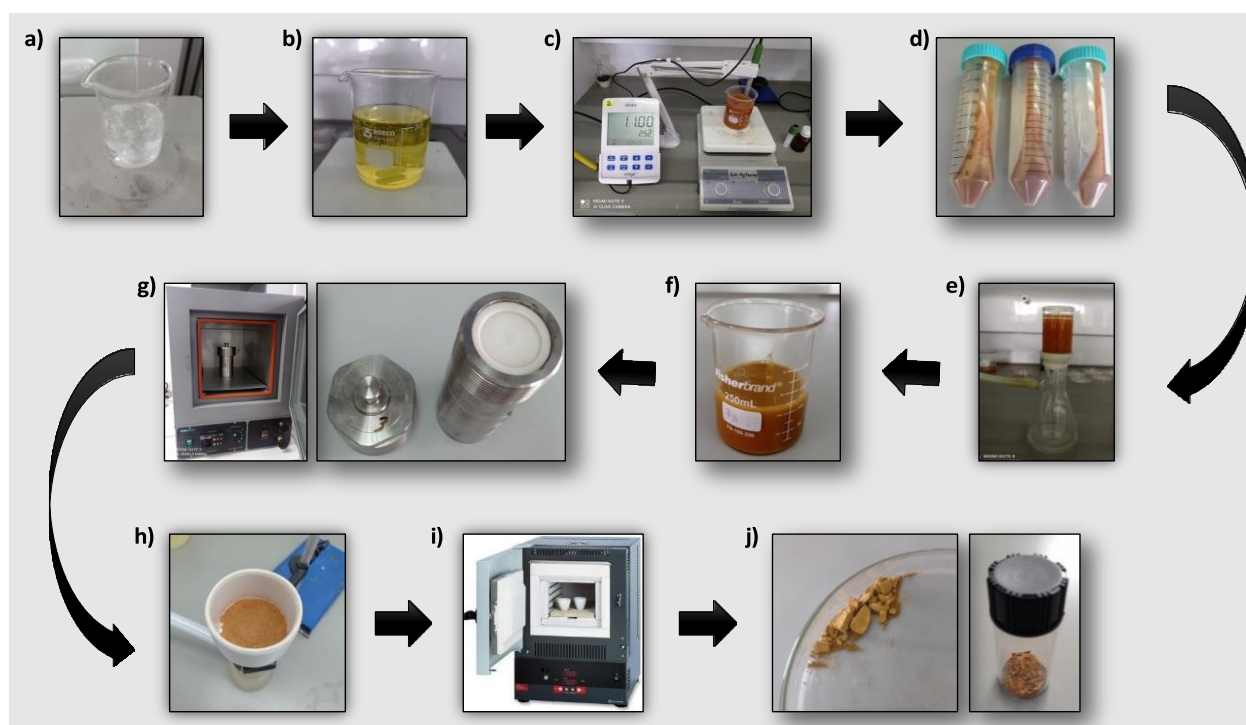
Figure 7. *Scheme of the solvothermal synthesis of BiFeO₃*

3.2.3. Synthesis of BiFeO₃/BiOCl microsheets (hybrid catalyst).

The synthesis of the BiFeO₃/BiOCl microsheets, which form the hybrid catalyst, was carried out by joining the synthesis methods of the BiOCl and BiFeO₃ precursors, indicated in the previous sections. In this context, the synthesis process presented in this section is based on the fact that the BiFeO₃ is synthesized at a temperature at 180 °C for 48 hours. Meanwhile, BiOCl is synthesized at a temperature at 160 °C for 24 hours. As seen, bismuth ferrite synthesis has more drastic conditions in temperature and time. Consequently, if this material is previously synthesized, its structure will not be affected by the bismuth oxychloride synthesis conditions.

The synthesis of the BiFeO₃/BiOCl hybrid (1:1), started by dissolving 0.93 g of bismuth ferrite (BiFeO₃) in 90 mL of DI water with vigorous stirring for 30 min (see Figure 8 a). Subsequently, 7.24 g of $Bi(NO_3)*5H_2O$ was added with 1.11 g of KCl and the solution was stirred for another 30 minutes (see Figure 8 b). Then, the solution was transferred to an autoclave reactor, with a volume of 150 mL, and heated in a muffle at 160 °C, for 24 hours (Figure 8 c). Once the reactor had cooled for approximately 10 hours, the solution was centrifuged at 9000 rpm for 3 minutes. Finally, the precipitate was washed three times with distilled water and ethanol (C_2H_5OH) (see Figure 8 d), and then dried in an oven at 60 °C for about 6 hours. The product obtained is the hybrid catalyst, and must be stored in an amber container, inside a desiccator, to avoid its activation or hydration (Figure 8 e and 8 f).
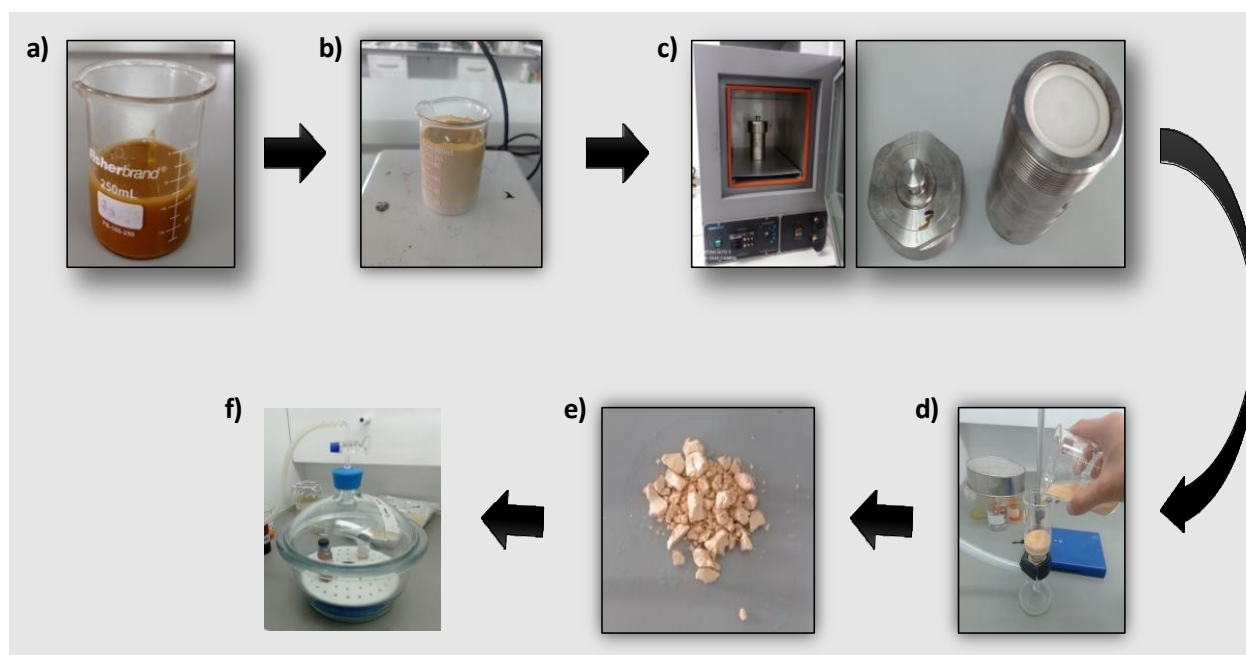
Figure 8. *Scheme of the solvothermal synthesis of BiFeO₃/BiOCl hybrid catalyst*

3.3. Characterization techniques

3.3.1. Structural and elemental analysis

3.3.1.1. X-Ray diffraction (XRD)

X-ray diffraction (XRD) is a widely used technique to determine the crystalline structure, spatial distribution, symmetry, size and distribution of particles in a sample. In this context, for catalysts such as the ones analyzed in this work, it allows determining the atomic arrangement and the distribution of the charge sites, to provide an approximation of the activity of the material. In the present thesis the equipment used for this analysis is the X-ray diffractometer for polycrystalline samples (Rigaku MiniFlex), equipped with a 600W X-ray tube, Bragg-Brentano goniometer with 8-position autosampler, D/teX Ultra detector, SmartLab Studio II software (see Figure 9). The following specifications were established for the analysis: X-ray generator operated at 40 kV and 15 mA, CuK(α) radiation source (sealed tube), $\Theta/2\Theta$ scanning axis, 0.005° pitch width, 10-100° scanning range in Θ and D/tex Ultra2 detector in 1D scanning mode.
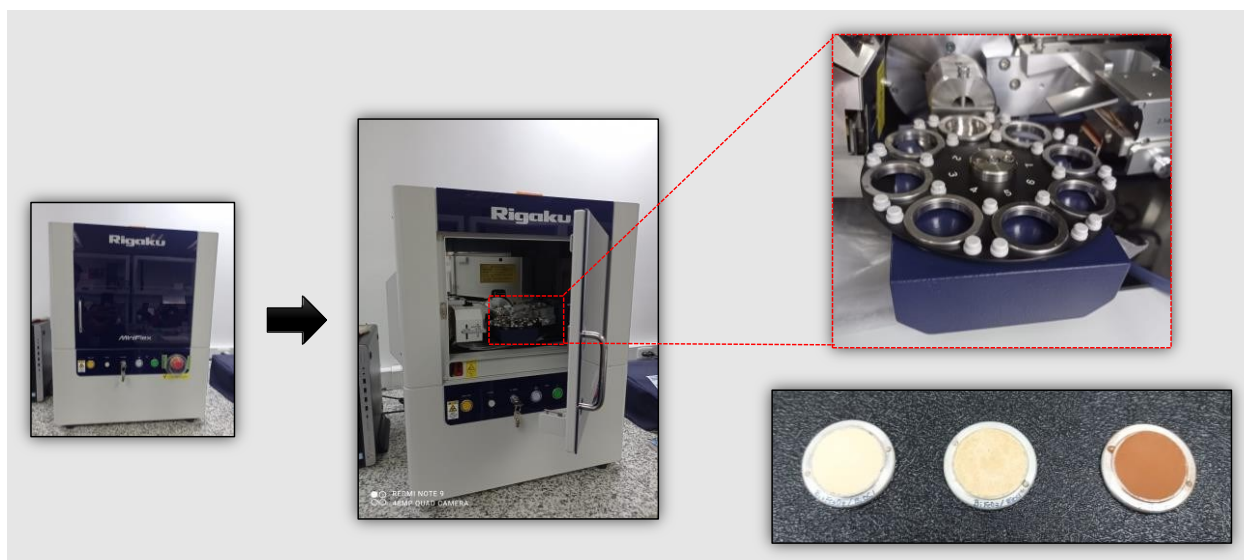
Figure 9. *X-Ray Diffraction (XRD), YACHAY TECH*

3.3.1.2. Fourier transform infrared spectroscopy (FT-IR)

Fourier transform infrared spectroscopy (FT-IR) is a technique for identifying functional groups present in the analyzed sample. Its principle of operation is based on the absorption of infrared radiation by the molecules that comprising the sample, inducing vibrational motions or modes within their chemical bonds. These vibrations are collected by a receiver (detector), and an image is generated with characteristic spectra at certain wavelength values. To perform this characterization, the mid-far range Fourier transform infrared spectrometer (PerkinElmer), standard, high performance, room temperature MIR LiTaO$_3$ (lithium tantalate) detector, high

performance, temperature stabilized MIR DTGS (deuterated triglycine sulfate) detector, standard optical system with KBr windows, were used for data collection in a spectral range of 8300 - 350 cm^{-1} with an optimum resolution of 0.5 cm^{-1}. Diamond ATR accessory for net range 4000 to 650 cm^{-1}, pH range 1-14, automatic recognition and safety screw to avoid overpressure. AVC (Atmospheric Vapor Compensation) standard with APV/AVI (Automatic Performance Verification/Absolute Virtual Instrument) configuration all controlled via Spectrum 10 software (see Figure 10). The following specifications were established for the analysis: ATR accessory, measuring range 4000 to 650 cm^{-1}, 4 accumulations.

Figure 10. Fourier transform infrared spectrometer used in (FT-IR), YACHAY TECH

3.3.1.3. X-Ray photoelectron spectroscopy (XPS)

X-Ray photoelectron spectroscopy (XPS) is a widely used technique to determine the oxidation state of the elements that make up a sample. Moreover, elemental analysis, band gap energies determination, and even morphology characterization using low-resolution images can all be accomplished with this method to perform this characterization, X-ray Photoelectron spectrophotometer (XPS) PHI model VersaProbe III, manufactured by Physical Electronics, was used, with a monochromatized Al Kα radiation source with energy of 1486.6 eV, operating in scanning mode with an energy bandwidth of 255 kV, and with high resolution for the acquisition bandwidth of 55 kV (Figure 11).
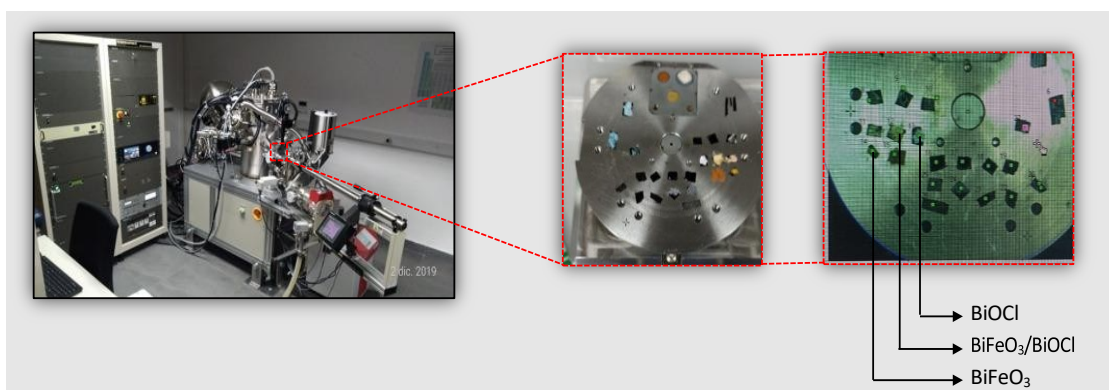
Figure 11. X-Ray photoelectron spectrophotometer (XPS), YACHAY TECH

3.3.1.4. Thermogravimetric analysis (TGA)

Thermogravimetric analysis (TGA) is a technique that allows to determine if chemisorbed water is present in a sample, by a hydration process. Additionally, it allows for determining the stability and thermostability of a given compound. A TGA Instruments thermogravimetric analyzer, model TGA 55 was used. The equipment is equipped with an automatic loader, a furnace (Pt/Rh), a double-inlet gas collector, operates in a temperature range from ambient to 1000 °C, linear heating rate-controlled modes (from 0.1 to 100 °C/min) or ballistic heating rate-controlled modes (> 600 °C/min), platinum and alumina sample vessels with a maximum capacity of 1000 mg and a resolution of 0.1 µg, was used to perform this analysis. The following specifications were established for the analysis: heating ramp from room temperature to 800 °C, heating rate 10 °C per minute, air atmosphere, platinum crucible (Figure 12).

Figure 12. Thermogravimetric Analyzer (TGA), YACHAY TECH

3.3.2. Size and morphology analysis

3.3.2.1. Scanning electron microscope (SEM)

Scanning electron microscopy (SEM) (see Figure 13) consists of shining a beam of electrons onto the surface of a sample. This interaction between the sample and the electrons generates a pulse-like response, which is captured by a receiver. In this way, information can be obtained about the external structure or morphology, the spatial orientation of the components, and even the chemical composition of the sample. Using this technique, a specific area can be analyzed and a two-dimensional image of the morphology in that area (dimension and depth) can be generated. To perform this characterization, each of the samples was placed on a scanning electron microscopy pin fixed with a double layer of double-sided carbon tape. Morphology evaluation was performed using a TESCAN model MIRA 3 field emission scanning electron microscope FEG-

SEM. Images were obtained at various magnifications operating at 10 kV. Additionally, semi-quantitative analysis of the elemental composition of each sample was performed in the SEM chamber operating at 35 kV using the Bruker X-Flash 6|30 Energy Dispersive X-Ray detector with 123 eV resolution for MnKα.

Figure 13. Scanning electron microscope (SEM), ESPE

3.3.3. Band gap energy determination (UV-Vis Diffuse Reflectance spectroscopy)

The band gap energy of a material can be calculated by its reflectance spectrum. In short, the reflectance spectrum can measure the percentage of light reflected by a sample at different wavelengths. For characterization, the sample must first be prepared, which must be in the form of a 1 cm diameter and 2 mm thick pellet. This process was carried out using a hydraulic press and a metal mold (see Figure 14 a). It is important to mention that the compaction of the material is achieved by pressure, and no binder should be used. Next, the equipment was calibrated; in this case a Horiba MicroHR monochromator spectrophotometer coupled to a DSS-SIGA (2.2) 020A detector was used. This spectrometer is equipped with a 75 W Xenon lamp (PTI PowerArc Fiber Iluminator, Horiba), wavelength range: 200 nm – 1100 nm (Figure 14 c). Then, the measurement parameters were established. In this context, the samples were analyzed in diffuse reflectance, with a wavelength range from 350 nm to 750 nm. The spectra recording process starts by measuring the spectrum of the target (Teflon). Subsequently, the spectrum of the sample is measured (Figure 14 b), in order to determine the percentage of reflectance (R%) with the equation (1):

$$R\% = \frac{I_{sample}}{I_{reference}} \cdot 100\% \qquad (1)$$

Subsequently, the Kubelka-Munk function (F) is determined by means of equation (2). Continuing with the mathematical treatment, the energy is determined, based on the multiplication of the Planck's constant ($h = 6.626 \cdot 10^{-34} J \cdot s$) by the frequency of light ($\nu\ (Hz)$), which is calculated from the wavelength ($\lambda\ (nm)$), as shown in equation (3). Finally, it is necessary to multiply the energy by the ($h\nu\ (eV)$) by the absorption coefficient of the material (F) and to square this term. This allows obtaining the Tauc graph, which has the energy ($h\nu$) on its x-axis, and the factor ($F \cdot h \cdot \nu)^2$ on its y-axis.

$$F = \frac{(1-R)^2}{2R} \tag{2}$$

$$E = h\nu = \frac{1240}{\lambda(nm)} \quad (eV) \tag{3}$$

Estimation of the band gap can be done by extrapolating the linear part of the Tauc diagram. This process involves drawing a straight line along the linear section of the curve and extending it until it crosses the energy axis or x-axis; the crossing point represents the band gap. This value is key to understanding the electronic and photoelectric properties of the material. In our study, this method was fundamental to estimate the band gap of three different catalysts.
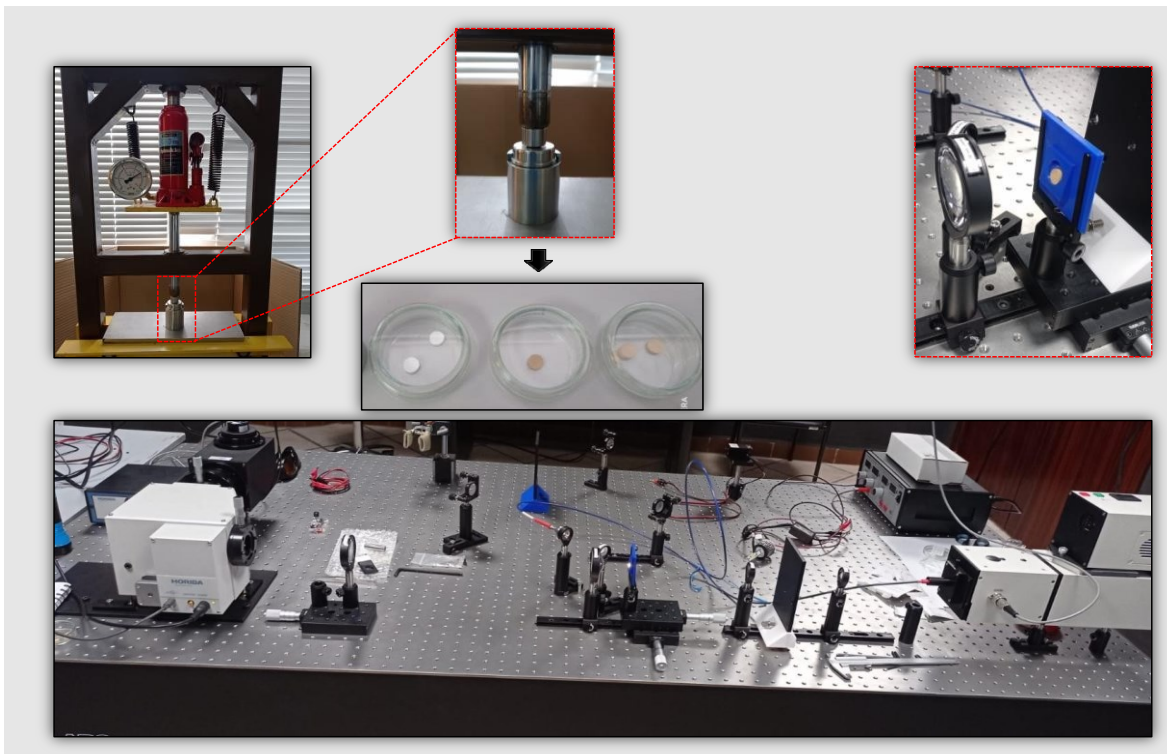
Figure 14. *Multifunctional optical system used for the Band gap analysis, PUCE*

3.4. Design and fabrication of the reactors for photocatalytic and piezocatalytic tests

3.4.1. Materials

The reactor structure is made of compressed wood (eco veneer), with a thickness of 8 mm. It has a power source of 9-12 Volts, in direct current. The light source is a Xenon lamp, with a power of 100 W, a luminous intensity of 8000 lumens and works in the white or visible light range (400 nm to 700 nm). Finally, black dye (Decorlac), double-sided tape, two electrical connectors and putty with high impact desiccant were used.

3.4.2. Photo reactor, piezo reactor and photo-piezo reactor design

The dimensions of the reactor were set based on the volume of the available stir plates, due to the fact that the photocatalysis process requires constant agitation and simultaneous irradiation. Thus, the dimensions established were 40 cm in length, 35 cm in high and 25 cm in width. The reactor was designed with two movable parts, which are the upper lid and the front lid. The for an adequately handle the materials inside the reactor. A wooden support was placed on the upper lid, which, with the help of the double-sided tape, allowed fixing the xenon light source. Next, small perforations were made in the back wall of the reactor to guide the cables of the light and power sources. Finally, the entire reactor was coated with black dye to favor the adsorption-desorption equilibrium required by the material in the photocatalytic process (see Figure 15).
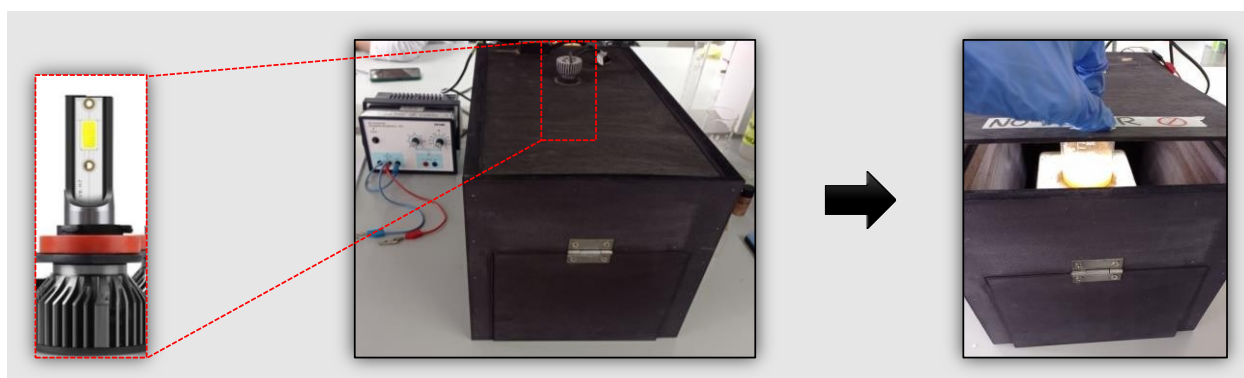
Figure 15. Photocatalytic reactor, YACHAY TECH

The reactor for photo-piezo catalysis was made using the same methodology mentioned in the previous paragraph. However, the dimensions were calculated based on the ultrasound equipment. Thus, the reactor is 40 cm long, 25 cm wide and 35 cm high. Additionally, this reactor was not coated with dye, because no major effect of incident light is expected in this system. This reactor was used to perform the photo-piezo catalysis tests, and therefore has a xenon light source at the top of its structure (see Figure 16). It is important to mention that the piezo catalysis reactions were carried out in this same reactor, with the difference that the light source was deactivated.
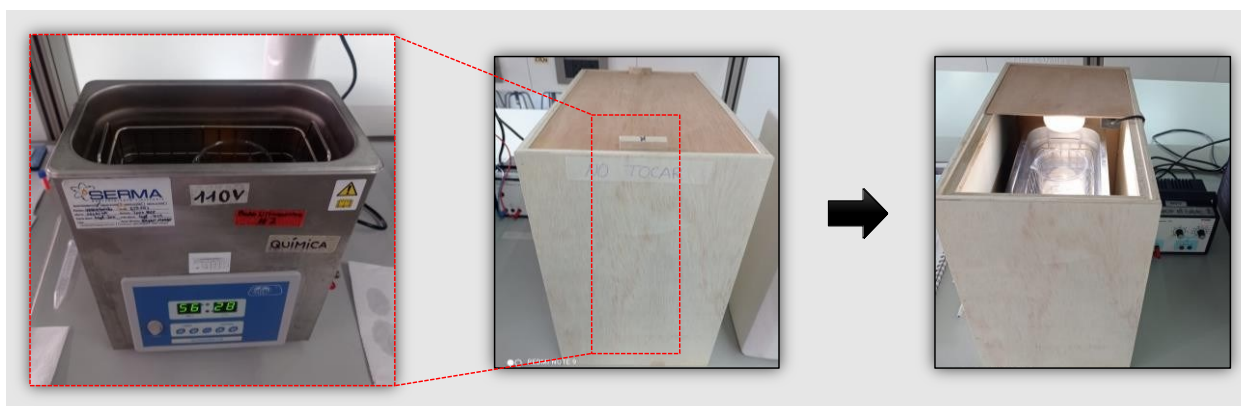
Figure 16. Photo-piezo catalytic reactor, YACHAY TECH

3.4.3. Characterization of the LED light source

To characterize the light source of the photocatalytic reactor it is necessary to measure its emission spectrum. For this purpose, the spectrophotometer described in section 3.3.3. was used, with a different configuration (see Figure 17). For this, first the necessary parameters such as the wavelength range 350 nm to 700 nm were established. Subsequently, the appropriate voltage and current values were set (9 V and 0.27 A), to avoid damage to the LED or variations in the measured spectrum. Subsequently, the LED was connected to the source and mounted on a fixed support to keep it stable during the measurement. This avoids movements that could affect the accuracy of the system. Once the LED was fixed, the beam and lenses were adjusted to ensure proper alignment of the entire system. Finally, the resolution of the spectrophotometer was adjusted, and the emission spectrum was measured.
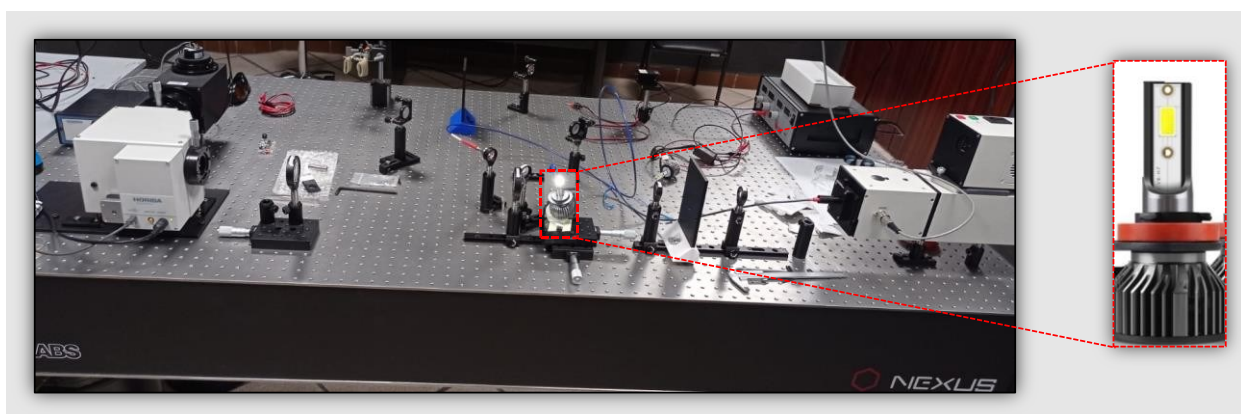
Figure 17. Multifunctional optical system – Light source characterization, PUCE

3.4.4. Characterization of the irradiation source by Photodegradation of TiO$_2$

The degradation test of RhB using TiO$_2$ as photocatalyst was carried out in the photocatalytic test reactor (Figure 15). For this purpose, first 100 mL of a dissolution of deionized water and RhB at a concentration of 2 ppm was prepared in a beaker. That is, 0.2 mg of RhB was dissolved in 100

ml of deionized water, by stirring at 150 rpm. Subsequently, 1 mg of TiO_2 (anatase) was weighed and added to the solution. This mixture was stirred for 30 minutes in complete darkness, to reach the adsorption-desorption equilibrium on the catalyst surface. After this time, the light source was turned on to start the photocatalysis process. From then on, aliquots of 2 mL were taken every 30 minutes, and after centrifugation, they were analyzed in a UV-Vis spectrophotometer to measure the absorption spectrum. This process is repeated for 4 to 5 hours, and allows the change in the absorbance curve, characteristic of the presence of RhB, to be evidenced. In this way, it was possible to determine the effect of the light source on the catalyst in the RhB degradation process.

3.4.5. Photolysis of RhB

The degradation test of RhB by photolysis was carried out in the photocatalytic test reactor designed for this thesis (Figure 15). To perform this process, first 0.2 mg of RhB was weighed and dissolved in 100 mL of deionized water. An aliquot was subtracted from this solution and its absorbance was analyzed using a UV-Vis spectrophotometer. Subsequently, the solution was placed inside the reactor, with agitation at 150 rpm. For 30 minutes, the solution was agitated to replicate the absorption-desorption process, according to the time established in the presence of a photocatalyst. Next, an initial aliquot was taken, and the reactor lamp was turned on to observe the effect of the photons on the RhB structure. Once the source was turned on, aliquots were taken every thirty minutes for 4 hours and their absorbance was measured in the UV-Vis equipment. Finally, a mathematical treatment of the absorbance data obtained was carried out to generate a degradation graph at absolute concentration. In this way, it was possible to determine the effect of the light source on the degradation process of RhB.

3.5. Calibration curve with Rhodamine B (RhB)

The calibration curve with RhB allows relating the absorbance measured in a UV-Vis spectrophotometer (instrumental measurement) to the absolute concentration of RhB contained in a sample. To perform the calibration curve with RhB, a stock solution was first prepared at 100 ppm. For this purpose, 10 mg of RhB were weighed and dissolved in 100 mL of deionized water. Subsequently, calibration solutions were prepared from the stock solution. The objective in this step was to make several 10 mL dilutions at different concentrations, up to a maximum of 2 ppm, as follows (see Table 4):

Table 4. Dilutions of RhB to perform the calibration curve

Concentration (ppm)	Volume of stock solution (µL)	Volume of deionized water (mL)
0.250	25.0	9.975
0.500	50.0	9.950
1.000	100.0	9.900
1.500	150.0	9.850
1.750	175.0	9.825
2.000	200.0	9.800

Once the solutions were prepared, the absorbance of each one of them was measured, taking the solvent (deionized water) as a blank (see Figure 18). Then, the maximum peak absorbance of each solution was plotted as a function of its concentration and a linear regression of all the points obtained was performed. The linear regression resulted in an equation: $y = mx + b$, where y represents the absorbance value, x represents the concentration, m represents the slope of the graph and b represents the intercept of the graph. It is important to validate that the calibration curve is correct. Therefore, it was verified that the R^2 value is very close to 1, to validate the process. Finally, the concentration value $\left(x = \frac{y-b}{m}\right)$, was cleared so that it could be applied in the following steps:
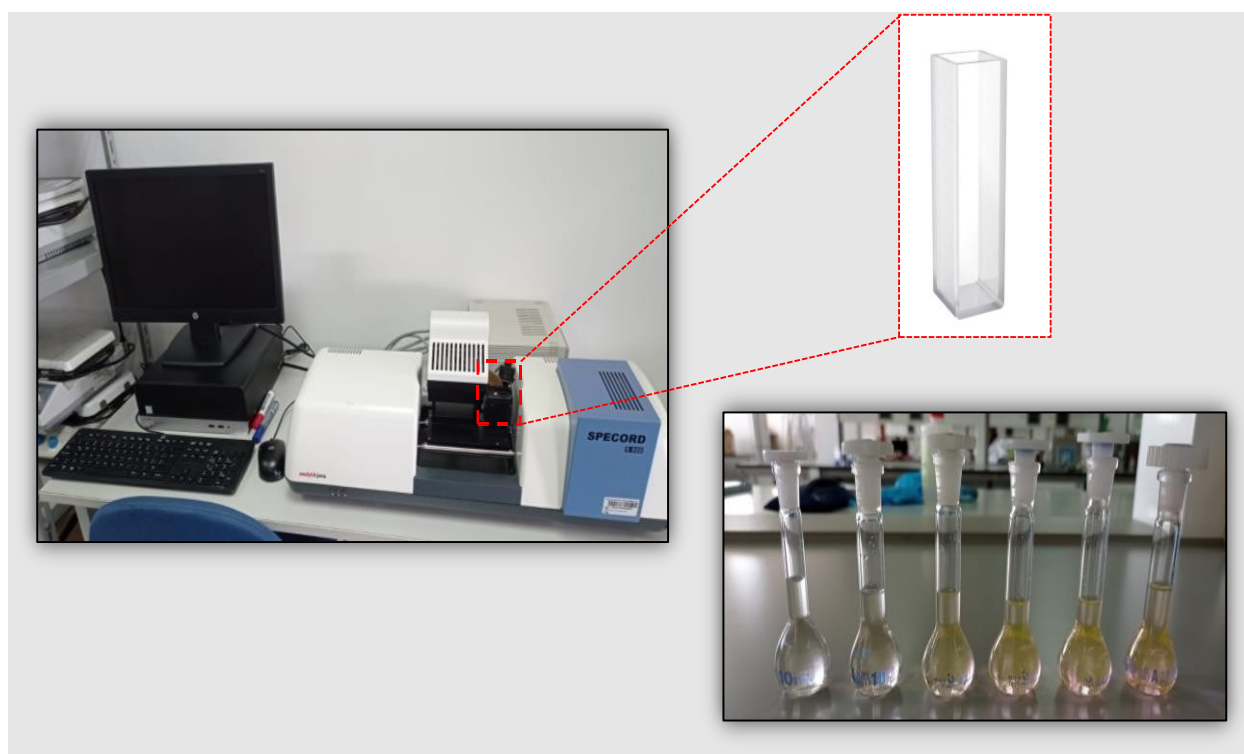
Figure 18. UV-Vis Spectrometer and RhB solutions for calibration curve. YACHAY TECH

3.6. Photocatalytic activity test

Photocatalytic degradation of RhB involves the use of a photocatalyst and a light source to induce the decomposition of this dye. The objective is to observe and measure the decrease in RhB concentration over time, using a UV-Vis spectrophotometer to measure absorbance. The step-by-step methodology performed in this experiment at a RhB concentration of 2 ppm is described below, using first the BiOCl photocatalyst and then the BiFeO$_3$/BiOCl hybrid catalyst. The concentration at which these tests were carried out is 1 mg catalyst per mL of dye solution.

3.6.1. Photocatalytic degradation of RhB with BiOCl and BiFeO$_3$/BiOCl (hybrid)

The first step in this photocatalytic activity test was to prepare the RhB solution at 2 ppm. For this purpose, a stock solution at 100 ppm was prepared by weighing 10 mg of the dye and diluting it in 100 mL of deionized water (Figure 19 a). Subsequently, 2 mL of the stock solution was taken and dissolved in 98 mL of deionized water, thus obtaining a volume of 100 mL of RhB solution at 2 ppm (see Figure 19 b). The next step was the weighing of the photocatalyst (BiOCl), knowing that the concentration of this material, with respect to the dye solution, is 1 mg/mL. In this sense, for a volume of 100 mL, 0.1 g of BiOCl was required (see Figure 19c). Before placing the photocatalyst into the solution, an aliquot was taken and its absorbance was measured, taking deionized water as a blank. This measured value represents the initial absorbance of the solution.

The photocatalyst was added to the RhB solution and placed inside the photocatalytic reactor in complete darkness and stirred at 150 rpm. This achieved the adsorption-desorption equilibrium in exactly 30 minutes (see Figure 19d). Once this time had elapsed, an aliquot was quickly taken, and the light source was switched on in order to start the photocatalysis process. From then on, aliquots of 2 mL were taken every thirty minutes, in a process that lasted 4 hours of irradiation (see Figure 19e). Regarding the aliquots taken in the process, these cannot be measured directly. Instead, they first went through a centrifugation process at 9000 rpm for 3 minutes. This is done to separate the suspended catalyst from the solution. After that, they were placed in a quartz cuvette and their absorbance was measured in the UV-Vis spectrophotometer (Figure 19 f).

Once the absorbance spectra were measured, the concentration equation $\left(x = \frac{y-b}{m} \right)$, described in the previous section, was used to convert the maximum absorbance value into a concentration value. Subsequently, these obtained concentration values are divided for the initial concentration value $\left(\frac{c}{c_0} \right)$, thus determining the absolute concentration value. Finally, the absolute concentration was plotted as a function of time, which represents the photocatalytic activity of the photocatalyst BiOCl.

The process described in this section was again carried out using the BiFeO₃/BiOCl hybrid photocatalyst. In this way, it was possible to obtain data that allowed a real comparison between the photocatalytic activity of both materials.
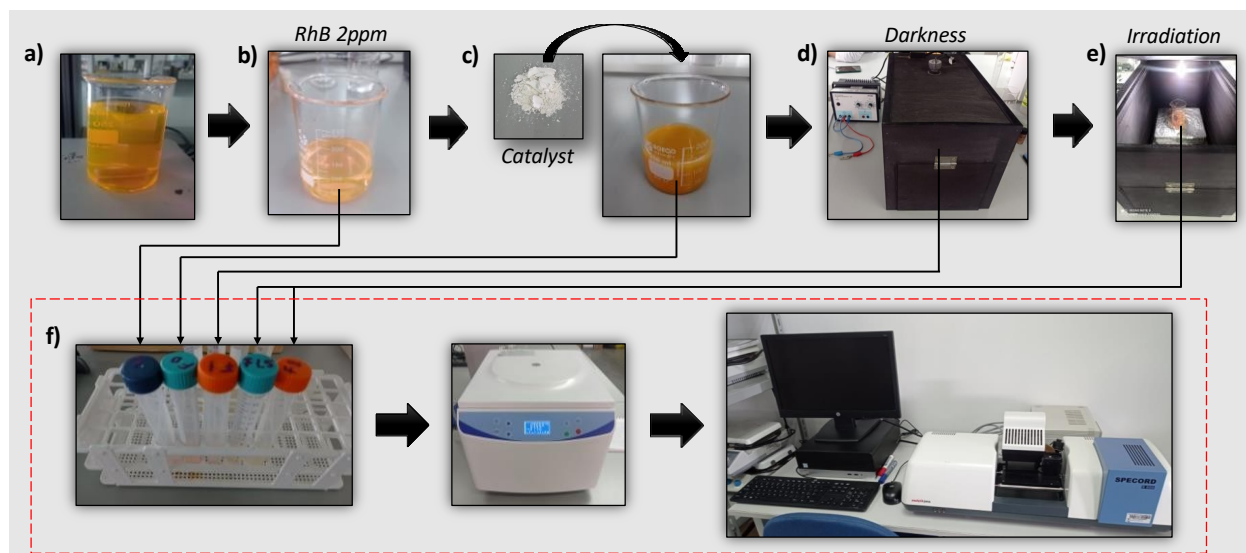
Figure 19. Scheme of the photocatalytic activity test

3.7. Piezocatalitic activity test

Ultrasonic waves were employed to activate the piezocatalyst in a typical RhB degradation experiment by piezocatalysis, thereby promoting the degradation of the dye. Like the process described in the previous section, the objective of this technique is to quantify the decrease in RhB concentration over time, using a spectrophotometer to measure absorbance spectra. The step-by-step methodology performed in this experiment at a generally established RhB concentration (2 ppm) is described below, using first the piezocatalyst $BiFeO_3$ and then the hybrid catalyst $BiFeO_3$/BiOCl.

3.7.1. Piezocatalitic degradation of RhB with BiOCl and BiFeO₃/BiOCl (hybrid)

The methodology described below is very similar to that detailed in the previous section, since both processes have similar characteristics, and it is important to maintain uniform conditions to allow an accurate comparison of the results. Now, the first step in the piezocatalytic activity test is to prepare the RhB solution at 2 ppm. To do this, a stock solution at 100 ppm is created by weighing 10 mg of the dye and dissolving it in 100 mL of deionized water (Figure 2 a). Then, 2 mL of this stock solution is taken and diluted in 98 mL of deionized water, thus generating 100 mL of a RhB solution at 2 ppm (Figure 20 b). The next step is to weigh the piezocatalyst ($BiFeO_3$), ensuring that the concentration with respect to the dye solution is 1 mg/mL. For a volume of 100 mL, 0.1 g of $BiFeO_3$ was required (Figure 20 c). Before introducing the piezocatalyst into the solution, an aliquot

is taken to measure its absorbance, using deionized water as blank**.**

The piezocatalyst was added to the RhB solution and placed in a piezocatalytic reactor, in complete darkness for 30 minutes and stirred, with agitation at 150 rpm to achieve adsorption-desorption equilibrium (Figure 20 d). After this time, an aliquot was taken and the ultrasound equipment was turned on, to start the piezocatalysis process. Thereafter, samples were taken every 30 minutes for a period of 4 hours of irradiation. It is essential to change the water in the ultrasound equipment every 15 to 20 minutes because the vibrations generated by the ultrasound tend to heat the bath water. This increase in temperature can have adverse effects on the piezocatalysis experiments, since thermal variations can alter the concentration of the sample (Figure 20 e).

To measure the absorbance spectrum of the aliquots taken, they were first centrifuged at 9000 rpm for 3 minutes, to separate the suspended piezocatalyst from the solution. Then, the samples were placed in quartz cuvettes and their absorbance was measured in a UV-Vis spectrophotometer (see Figure 20-f). Based on the absorbance spectra, the concentration equation obtained from the calibration curve was applied and the absolute concentration was determined. To conclude the process, absolute concentration was plotted as a function of time to evaluate the piezocatalytic activity of the piezocatalytic $BiFeO_3$. The same methodology was implemented once again, but this time with the hybrid $BiFeO_3/BiOCl$ photocatalyst. This allowed data to be collected for a comparative analysis of the photocatalytic efficiency of both materials.
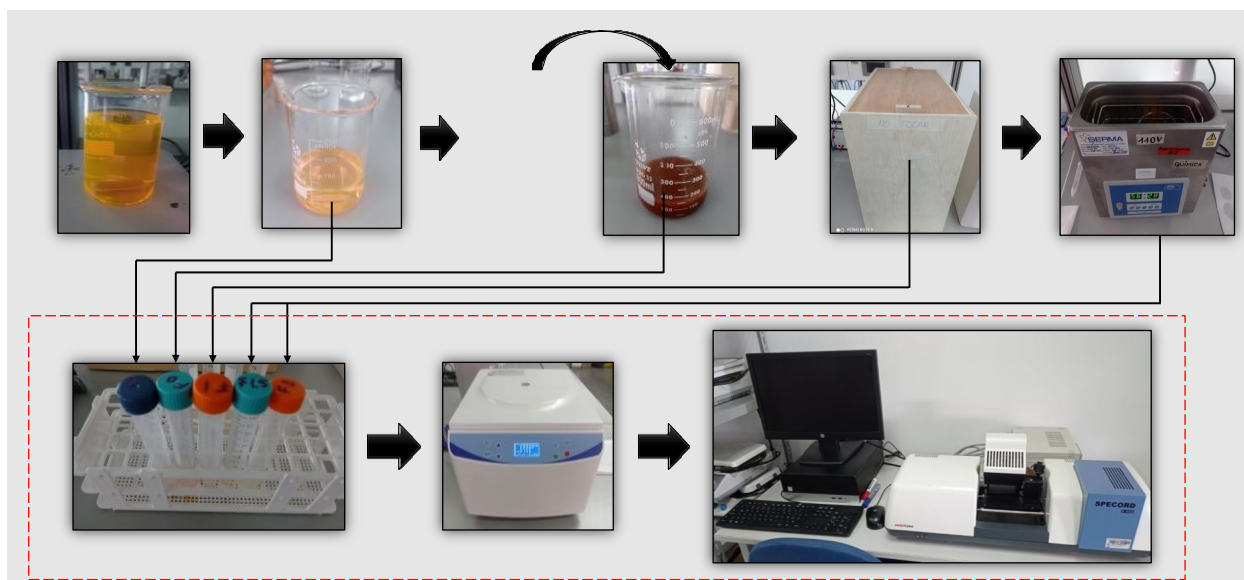
Figure 20. *Piezocatalytic activity test*

3.8. Photo-piezo catalytic activity test

The catalytic photo-piezo activity of the hybrid catalyst (BiFeO$_3$/BiOCl) was measured in the piezocatalysis reactor (Figure 16). This is because it has adequate dimensions for the ultrasound equipment to be placed inside. Additionally, it was incorporated a light source identical to the one used in the photocatalysis reactor. Thus, the process was carried out under the same conditions for the three techniques, which allowed a comparison of the results obtained.

3.8.1. Photo-piezo catalytic degradation of RhB with BiOCl and BiFeO$_3$/BiOCl catalyst

A methodology similar to those detailed in the two previous sections was followed, but using the hybrid catalyst BiFeO$_3$/ BiOCl as the only test material. First, a solution of RhB at 2 ppm was prepared, for which 10 mg of the dye were dissolved in 100 mL of deionized water to obtain a stock solution at 100 ppm. From this, 2 mL were taken and diluted in 98 mL of deionized water, obtaining 100 mL of a solution at 2 ppm. Then, the hybrid catalyst was added to the solution at a ratio of 1 mg per mL. Then, the catalytic photo-piezo reactor was placed in complete darkness and stirred at 150 rpm for 30 min to reach adsorption-desorption equilibrium. Then, an aliquot was taken and the light source and ultrasound were turned on, to start the photo-piezo catalysis. Throughout the 4 hours of irradiation, samples were taken every 30 minutes and the water in the system was constantly changed to avoid evaporation and alteration of the concentrations. Subsequently, before measuring the absorbance spectrum, the samples were centrifuged at 9000 rpm for 3 minutes to separate the catalyst. Then, the absorbance of each sample was measured with a UV-Vis spectrophotometer. Finally, with these data, the absolute concentration of RhB was calculated to analyze the degradation efficiency, comparing these results with the previously performed experiments (Figure 21).
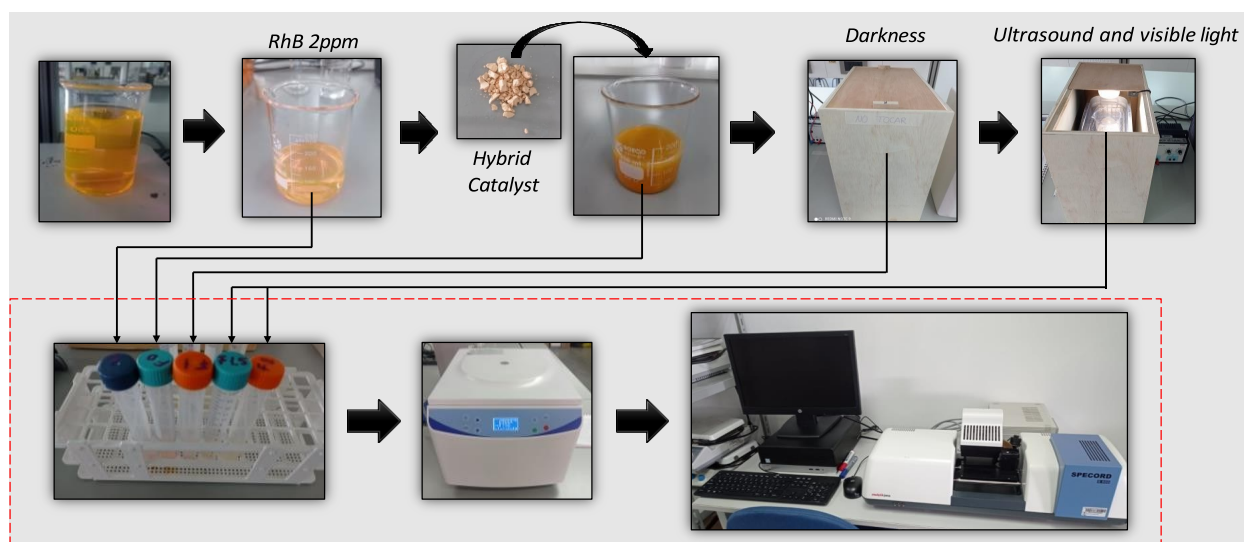
Figure 21. Scheme of the photo-piezo catalytic activity test

3.9. Point of zero charge

The point of zero charge (PZC) is the pH value at which the catalyst surface has no net charge. This point is important to understand the behavior of catalysts in aqueous solutions, since it is closely related to the surface adsorption process. In this section, the PZC of the hybrid catalyst $BiOCl/BiFeO_3$ was determined by the titration method. The process started by preparing 10 solutions of 50 mL, with different pH values, starting at pH 3, up to pH 12. These solutions were made by dissolving either HNO_3 or NH_4OH, 25% in deionized water, and were controlled with a digital pH meter. In each of the solutions 0.1 g of the hybrid catalyst $BiFeO_3/ BiOCl$ was added and stirred at 300 rpm for one hour.

Once this time had elapsed, the agitation was stopped and the solutions were left at rest for 24 hours. Subsequently, the solutions were centrifuged at 9000 rpm for 30 minutes in order to separate the hybrid catalyst from the solution. Once separated, the pH of each solution was measured and these values were recorded. Once the practical part was carried out, the data obtained were processed. For this, the final pH was plotted as a function of the initial pH, resulting in a series of scattered points. Finally, a 45° line was drawn on the graph, and the PZC was determined by finding the point at which the plotted line and the graph of the data intersect.

3.10. Antibacterial activity of BiFeO₃/BiOCl hybrid

The antibacterial activity was performed by two methods of analysis. The first method was the Kirby-Bauer disk diffusion susceptibility test, on Mueller-Hinton (MH) agar medium, where two bacterial strains were tested which are: *E. coli* ATCC 25922 and *Staphylococcus aureus* UITEY-Sa. On the other hand, the second method was the measurement of turbidity by means of the absorbance spectrum through a UV-Vis spectrophotometer, using culture broth as culture medium and only the *E. coli* ATCC 25922 strain was used. The main difference between the two methods used is in the activation process of the hybrid catalyst. In the disk diffusion method, the reactive oxygen species formed on the surface of the catalyst must diffuse through a semi-solid medium. On the other hand, in the turbidity measurement method, the reactive oxygen species diffuse through a liquid medium.

Before starting to measure the antibacterial activity of the hybrid catalyst, it is essential to verify that the bacterial strains are not contaminated. For this purpose, the Gram staining technique was used. This technique began with the inoculation of the bacterial strains on previously disinfected slides (Figure 22 a). Subsequently, the bacteria were fixed to the slide by passing it several times very close to the flame of a burner (Figure 22 b). Once the strains were fixed on the slide, crystal violet was applied to the smear and allowed to act for 1 minute to stain all the bacteria

purple. Then rinsed with distilled water to remove excess stain. Next, iodine was applied as a mordant, left to act for 1 minute and then rinsed again with distilled water**.**

Gram decolorant was then applied for a few seconds to decolorize the Gram-negative bacteria, maintaining the purple dye for the Gram-positive bacteria. It was rinsed again with distilled water to remove the Gram decolorant. Next, safranin was applied for 1 minute to stain the Gram-negative bacteria pink (Figure 22 c). Finally, the slides were rinsed with distilled water, dried and observed under the microscope at 100x resolution with the oil immersion objective (Figure 22 d**).**
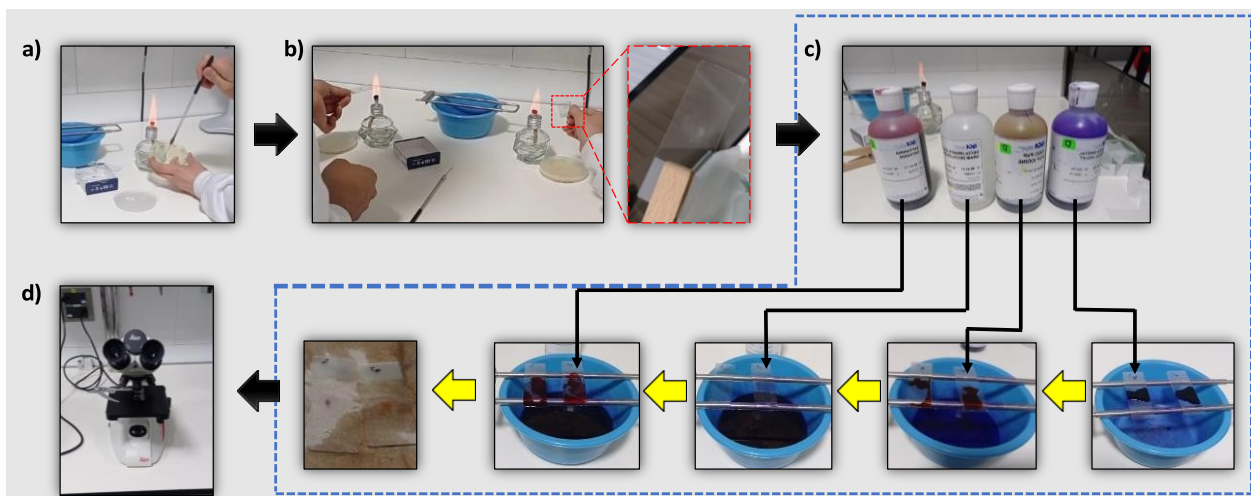
Figure 22. *Scheme of the gram stain technique*

3.10.1. Disk-diffusion assay

The first step was to prepare the inoculum. For this, 2 mL of each bacterium (*E. coli* ATCC 25922 and *Staphylococcus aureus* UITEY-Sa) were added to 100 mL of sterile culture broth, and incubated in a shaker at 120 rpm for 12 hours at 37 °C. Then, the turbidity of the inoculum was adjusted to McFarland's 0.5 standard, corresponding to an absorbance of 0.12 at 625 nm according to the Nanodrop. This suspension was to be used within 15 minutes maximum, to maintain its stability. For bacterial seeding, a sample of the inoculum was taken and plated on Mueller-Hinton agar in each Petri dish. Subsequently, 10 μL of each solution was added to previously sterilized Whatman No. 1 filter paper discs and carefully placed on the surface of the agar in the Petri dishes. Finally, the Petri dishes were divided into two groups. One group was incubated at 35 °C for 16-18 hours without light irradiation (Figure 23 a). The other group of Petri dishes was incubated under the same conditions, but with visible light irradiation (Figure 23 b**).**

Figure 23. Samples for antibacterial activity in Petri dishes groups

3.10.2. Absorbance analysis using UV-VIS spectroscopy

The antibacterial activity by absorbance analysis is based on the turbidity of the culture media analyzed. Similar to the process described in the previous section, for this procedure, 12 mL of the bacterial strain *E. coli* ATCC 25922 was added to 600 mL of sterile culture media and allowed to incubate on a shaker at 120 rpm for 12 hours at a temperature of 37 °C. Then, the turbidity level of the inoculum was adjusted to McFarland's 0.5 standard, which is equivalent to an absorbance of 0.12 at 625 nm using the Nanodrop. Again, the suspension was to be used within a maximum period of 15 minutes to maintain its stability. Subsequently, 6 previously sterilized 500 mL beakers were placed in the laminar flow chamber and 100 mL of nutrient broth was poured into each one. Then, each of the beakers was labeled as follows**:**

Beaker 1: Nutritious broth (CN)

Beaker 2: Nutritious broth (CN) + *E. coli*

Beaker 3: Nutritious broth (CN) + *E. coli* + Ampicillin (Amp)

Beaker 4: Nutritious broth (CN) + $BiFeO_3$/BiOCl (Cat)

Beaker 5: Nutritious broth (CN) + *E. coli* + $BiFeO_3$/BiOCl (Cat)

Beaker 6: Nutritious broth (CN) + *E. coli* + $BiFeO_3$/BiOCl (Cat)

Once this process was completed, a 1 mg/mL ampicillin solution was prepared and placed in beaker 3, to be used as a negative control. On the other hand, 2 mL of the *E. coli* culture was poured into beakers 2, 3, 5 and 6 and immediately, 0.1 mg of the hybrid catalyst was placed in beakers 4, 5 and 6. Once all the samples were in the medium, aliquots of each one were taken and the initial absorbance was measured**.**

Similar to the photocatalysis and piezocatalysis processes, the next step consisted of placing the samples under agitation at 150 rpm, in complete darkness for 30 minutes, to allow the adsorption-desorption equilibrium to be reached. After this period, aliquots were taken to measure absorbance. The reactor light source was then turned on, for beaker 6 only, to start the photocatalysis process, which lasted for 5 hours. During this time, samples were taken from all vessels every 30 minutes to analyze the absorbance. It is important to note that this process was only photocatalytic, not photo-piezo-catalytic, since ultrasound can affect bacterial growth by itself. Once the absorbance values were obtained, the measured results were plotted (Figure 24).
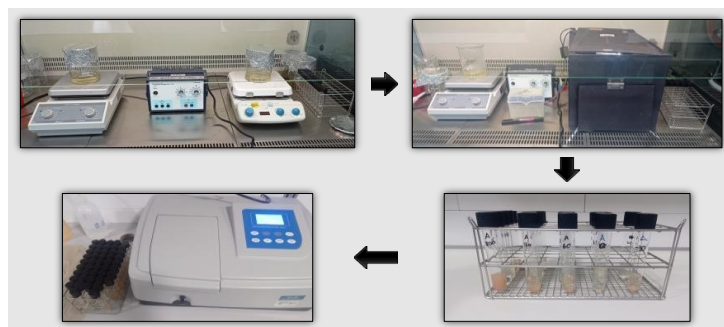
Figure 24. Experimental scheme for antibacterial activity with absorbance analysis

To corroborate the adequacy of the results obtained, the samples were diluted with *E. coli* and seeded on nutrient agar media for colony counting. For this purpose, serial dilutions were first performed to reach the previously determined ideal concentration (105 CFU/mL). For this, a dilution factor of 1:10 was used, where 1 mL of the culture was taken and diluted in 9 mL of saline solution. This process was repeated until the aforementioned concentration was reached. Subsequently, 1 mL of the dilution was spread on the agar surface with a sterile seeding loop, ensuring uniform distribution. Finally, the Petri dishes were incubated at 37 °C for 24 hours in order to count the colonies.

3.11. Cytotoxicity of BiFeO$_3$/BiOCl hybrid

The standard protocol of Promega Corporation (2012) for CellTiter 96 ® Aqueous One Solution cell proliferation assays (MTT) was followed to evaluate the cytotoxicity of the hybrid catalyst BiFeO$_3$/BiOCl. For this purpose, the fibroblast cell culture was prepared beforehand, and unlike the normal protocol, the appropriate amounts of catalyst (0.01 mg and 0.05 mg) were weighed instead of dissolving them, since it is an immiscible material. The catalyst samples were dissolved in Eppendorf vessels containing 1 mL of 1x medium. One of the samples was irradiated with the light source for 1 hour. The other sample was kept in complete darkness for the same time.

The cell line was then harvested with a cell scraper and assessed for viability with trypan blue dye in a Neubauer chamber. Dulbecco's modified Eagle's medium (DMEM), which was supplemented with 1% antibiotics and 10% decomplemented fetal bovine serum, was used. Subsequently, 96-well ELISA plates were prepared, where each well first contained 50 µL of 1x medium, followed by 50 µL of 4x medium, 50 µl of the catalyst (activated or deactivated) and 50 µL of fibroblasts. Subsequently, the plates were incubated at 37 °C for 48 hours in a 5% CO_2 environment (see Figure 24). Finally, 20 µL of MTT reagent was added to each well in an ELISA plate, and then incubated for 4 hours at 37 °C in a humidified chamber. During this period, absorbance was measured at 490 nm using an ELISA reader at 0-, 1-, 2- and 3-hour intervals.
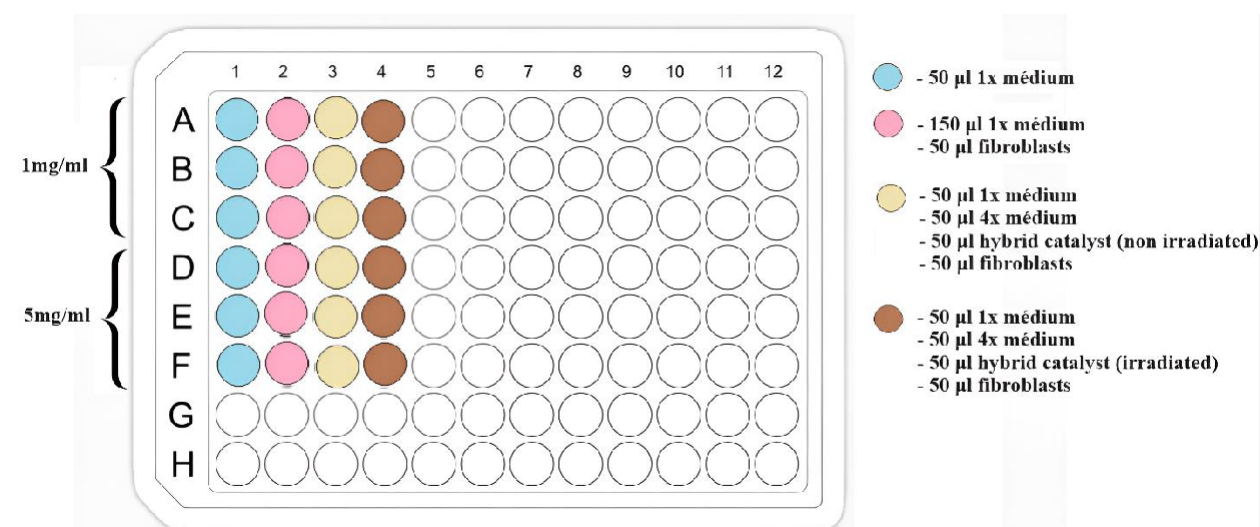
Figure 25. *Compounds distribution scheme for MTT Cytotoxic Assay*

3.12. Determination of ROS species

To perform the scavenging assay to determine ROS species, a 2ppm RhB solutions were prepared incorporating silver nitrate, formic acid and 2-propanol, each in different experiments, at a concentration of 5 mM. These compounds were respectively selected to capture electrons, positive holes and hydroxyl radicals. The experiment was carried out by photo-piezo catalysis using the hybrid catalyst $BiFeO_3/BiOCl$. The evaluation of the activity of the scavengers was performed using UV-Vis spectroscopy, in the same way as the photo-piezo catalysis experiments mentioned in section 3.8.1 were carried out.

CHAPTER 4. RESULTS AND DISCUSSION

4.1. Characterization techniques

4.1.1. Structural and elemental analysis

4.1.1.1. X-Ray diffraction (XRD)

The characterization of the $BiFeO_3$ nanosheets by XRD allowed determining the crystalline structure, purity and particle size of the catalyst. To determine the crystalline structure, Figure 26 shows the XRD spectrum of the catalyst. The intensity peak at 22.42° corresponds to the reflection plane (011). Next, the lower intensity peaks located at 31.77° and 32.07° correspond to the (01-1) (112) planes. Continuing with the spectrum, at values of 37.65° and 38.98° are the typical planes (201) and (020). Subsequently, and with less intensity, there is the peak located at 39.49° typical of the reflection plane (002). Next, there are the peaks corresponding to 45.76°, 49.75° and 51.74° which have a similar intensity value and correspond to the planes (220), (131) and (123) respectively. Next, the peak with the highest intensity is located at 56.4°, corresponding to plane (130). Finally, with a similar intensity are the peaks at 60.88°, 67.08° and 79.39° corresponding to crystallographic planes (023), (224) and (344) in the same order. After the analysis of each peak obtained from the CODINO-2206 database, it has been determined that the compound is $BiFeO_3$, and therefore its card code is 00-433-3972.
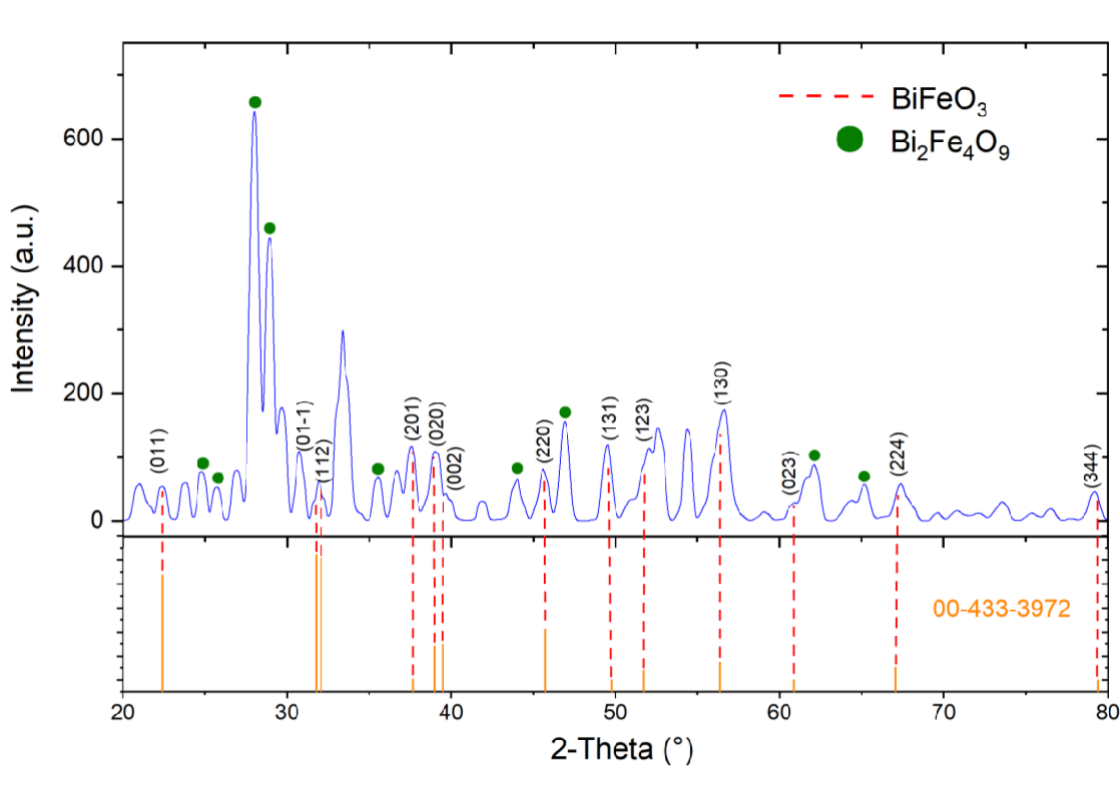
Figure 26. *X-Ray Diffraction result of BiFeO₃ nanosheets*

A total of 9 peaks corresponding to the $Bi_2Fe_4O_9$ compound can be observed in Figure 26. This is due to the synthesis process of the compound, specifically in the calcination stage. As mentioned in section 3.2.2, $BiFeO_3$ is calcined at 400 °C, for exactly 2 hours. This is because, if the time is longer than 2 hours or the calcination is performed at a temperature higher than 400 °C, the structure of the compound is altered from $BiFeO_3$ to $Bi_2Fe_4O_9$. In this context, the synthesis calcination was carried out in a muffle, whose specific requirement is that it can only be opened once it cools down to a temperature of 50°C. Therefore it was not possible to calcine the sample for exactly 2 hours, but it was calcined for approximately 5 hours. This variation generates the presence of the compound $Bi_2Fe_4O_9$, occupying 37% of the total mass.

Continuously, the crystal structure analysis has been performed for the $BiFeO_3$ compound, which is the subject of study of the present thesis. Like the crystallographic planes mentioned above, the crystal structure was obtained from the Qualx software database. As shown in Figure 27, the crystal structure of the catalyst is triclinic (distorted octahedron). In the unit cell it can be observed that the central atom is iron, which has the property of dislocating in the presence of ultrasound, generating the polarization of the material. The location of the iron is fundamental to understand the results obtained by the characterization techniques that will be described in the following sections, especially when analyzing the structure of the hybrid catalyst.
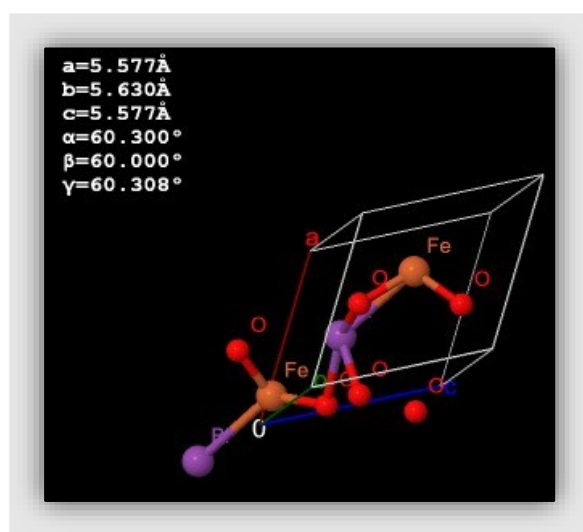
Figure 27. *Unit cell for the crystalline structure of BiFeO₃*

Table 5 presents the particle sizes obtained from the XRD spectra through the Scherrer equation. The data were obtained through peak width analysis (FWHM), using the Scherrer equation:

$$\left(D = \frac{K \cdot \lambda}{\beta \cdot cos} \right)$$

Where:

D = Is the size of the crystal in nanometers (nm).

K = 0.90, is dimensionless (unitless).

λ = 0.15406 (nm) is the wavelength of the X-ray.

β = FWHM, is the width at half peak height (in radians)

θ = Is the Bragg diffraction angle (also in radians).

As can be seen, the average size of the $BiFeO_3$ nanosheets is 96.36 nm on average. This is due to the fact that the nanoparticles are irregular in size, but all are within the nanometer scale. This is a very important factor in the analysis, as it corroborates that the synthesis process has been carried out properly.

Table 5. *$BiFeO_3$ particle size by Scherrer's equation*

2θ (°)	θ	cos θ	K	λ (nm)	FWHM (°)	FWHM (rad)	Crystall Size (nm)
22.42	11.21	0.981	0.9	0.15406	0.12	0.002	67.49
31.77	15.885	0.962	0.9	0.15406	0.08	0.001	103.25
32.07	16.035	0.961	0.9	0.15406	0.16	0.003	51.66
37.65	18.825	0.947	0.9	0.15406	0.07	0.001	119.90
38.98	19.49	0.943	0.9	0.15406	0.16	0.003	52.67
39.49	19.745	0.941	0.9	0.15406	0.08	0.001	105.51
45.76	22.88	0.921	0.9	0.15406	0.11	0.002	78.39
49.75	24.875	0.907	0.9	0.15406	0.05	0.001	175.14
51.74	25.87	0.900	0.9	0.15406	0.13	0.002	67.91
56.4	28.2	0.881	0.9	0.15406	0.24	0.004	37.56
60.88	30.44	0.862	0.9	0.15406	0.08	0.001	115.17
67.08	33.54	0.834	0.9	0.15406	0.09	0.002	105.90
79.39	39.695	0.770	0.9	0.15406	0.06	0.001	172.07
						Average	**96.36**

On the other hand, XRD was performed for the BiOCl sample, obtaining the following planes. As shown in Figure 28, the peak with the highest intensity is located at 12° and corresponds to the crystallographic plane (001). Additionally, the following planes with the highest intensity are located at 24.15°, 33.48° and 36.57° and correspond to planes (002), (102) and (003). From these points, the intensity decreases, and we find new values of 2θ, located at 25.88°, 32.52°, 40.91°, 49.73°, 55.13° and 58.63°. The following planes are associated to these points: (101), (110), (112), (113), (104) and (212) respectively. Finally, in the points with lower intensity are: 60.65°, 63.04°, 68.13°, 75.03°, 77.71° and 86.77°. To these points correspond the crystallographic planes (203), (005), (220), (214), (006) and (116). After the analysis of each peak obtained from the CODINO-2206 database, it has been determined that the compound is BiOCl, and therefore its card code is 00-

101-1175. Once the characteristic peaks have been determined, we can also conclude that the synthesis process described in the methodology was correct, and therefore the variables are adequate.
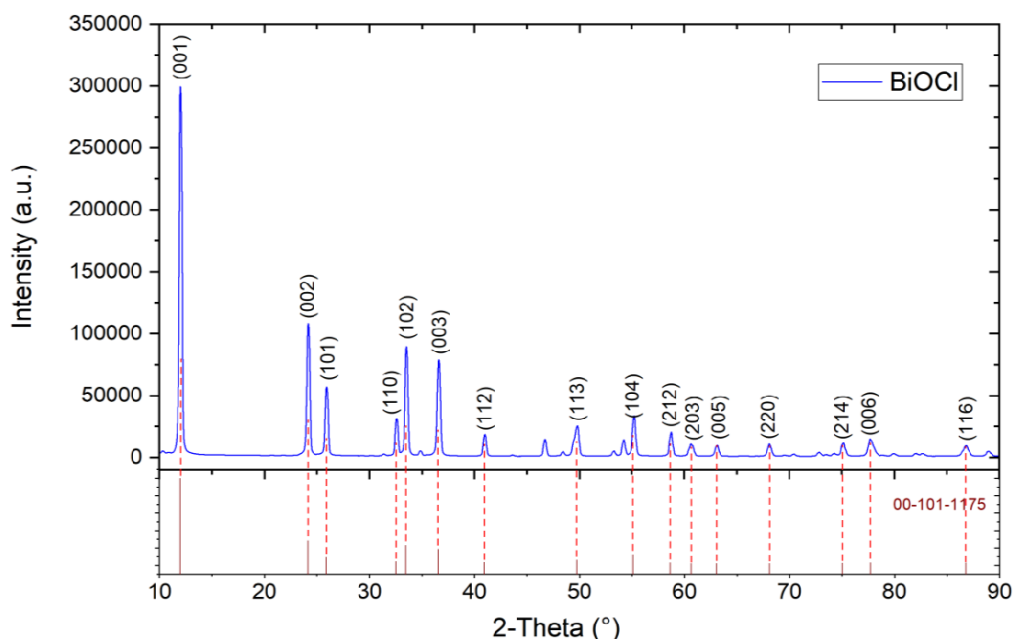
Figure 28. *X-Ray Diffraction result of BiOCl*

The database shows that the crystal structure is of the tetragonal type (see Figure 29), with oxygen atoms located at the edges and chlorine and bismuth atoms distributed in the center of the unit cell. What stands out in the structure is precisely the arrangement of the atoms, in the form of alternating layers of bismuth, chlorine and oxygen. That is, the bismuth atoms are coordinated by oxygen atoms on one side and chlorine atoms on the other side, forming the layered structure. This structure is of vital importance for photocatalytic processes, as it allows efficient charge separation along the layers.
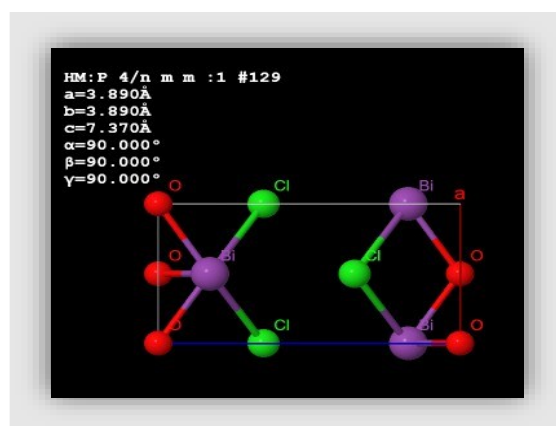
Figure 29. *Unit cell for the crystalline structure of BiOCl*

On the other hand, Table 6 presents the particle size analysis for BiOCl, whose data were obtained from Qualx software to be used in the Scherrer equation. Thus, it can be corroborated that

the particle size is approximately 74.69 nm. However, this value is not consistent with length measurement in SEM, and this is due to the fact that this calculation has been made based on the calculation of the width at half height, which may vary depending on the peak. In addition, the measurement is performed only in coherent crystalline regions. That is, those regions where the crystal structures are perfectly aligned and without significant defects.

Table 6. BiOCl particle size by Scherrer equation

2θ (°)	θ	cos θ	K	λ (nm)	FWHM (°)	FWHM (rad)	Crystall Size (nm)
12	6	0.9945	0.9	0.15406	0.13	0.002	61.45
24.15	12.075	0.9779	0.9	0.15406	0.14	0.002	58.03
25.88	12.94	0.9746	0.9	0.15406	0.14	0.002	58.22
32.52	16.26	0.96	0.9	0.15406	0.1	0.002	82.75
33.48	16.74	0.9576	0.9	0.15406	0.14	0.002	59.26
36.57	18.285	0.9495	0.9	0.15406	0.14	0.002	59.76
40.91	20.455	0.9369	0.9	0.15406	0.11	0.002	77.08
49.73	24.865	0.9073	0.9	0.15406	0.1	0.002	87.56
55.13	27.565	0.8865	0.9	0.15406	0.11	0.002	81.47
58.63	29.315	0.872	0.9	0.15406	0.1	0.002	91.10
60.65	30.325	0.8638	0.9	0.15406	0.13	0.002	70.75
63.04	31.52	0.8524	0.9	0.15406	0.13	0.002	71.69
68.13	34.065	0.8284	0.9	0.15406	0.1	0.002	95.90
75.03	37.515	0.7932	0.9	0.15406	0.12	0.002	83.46
77.71	38.855	0.7787	0.9	0.15406	0.13	0.002	78.48
86.77	43.385	0.7268	0.9	0.15406	0.14	0.002	78.07
						Average	**74.69**

To conclude this characterization technique, Figure 30 shows the XRD spectrum of the hybrid catalyst (BiFeO$_3$/BiOCl). In the spectrum, the characteristic peaks of the BiOCl compound stand out. However, it is also possible to observe, in smaller proportion, some of the characteristic peaks of BiFeO$_3$ (see Table 7). With respect to BiOCl, 15 of the 16 characteristic peaks are found. That is, this corroborates that the structures corresponding to BiOCl are larger and are found in the outermost part of the hybrid material. Thus, the average particle size of BiOCl, present in the hybrid catalyst sample, is 73.83 nm. However, this value is under discussion, since it is not consistent with the reported results for this material following our synthesis protocol. As mentioned in the previous section, this is because the measurement is performed only in the coherent crystalline regions of the material; despite having a larger particle size, it presents large dislocations that affect its structure.

On the other hand, with respect to the BiFeO$_3$ catalyst, only 4 peaks out of a total of 13 peaks could be found. This is due to the fact that the size of these particles should be smaller, with respect

to BiOCl. Additionally, these nanoparticles are immersed in the hybrid catalyst matrix, so the X-ray diffraction equipment cannot penetrate deep enough to detect all the characteristic peaks of the BiFeO3 catalyst. In this context, it is important to emphasize that the XRD equipment has a penetration depth of approximately 1000nm, and as will be seen in later sections, the BiOCl compound is found on a scale greater than this length.

Table 7. *Characteristic peaks of BiOCl and BiFeO₃ in the BiFeO₃/BiOCl hybrid catalyst*

Hybrid catalyst (BiFeO$_3$/BiOCl)			
BiOCl		BiFeO$_3$	
Peaks	Crystall Size (nm)	Peaks	Crystall Size (nm)
12	61,45	22,42	67,49
24,15	58,03	31,77	103,25
25,88	58,22	32,07	51,66
32,52	82,75	37,65	119,90
33,48	59,26	38,98	52,67
36,57	59,76	39,49	105,51
40,91	77,08	45,76	78,39
49,73	87,56	49,75	175,14
55,13	81,47	51,74	67,91
58,63	91,10	56,4	37,56
60,65	70,75	60,88	115,17
63,04	71,69	67,08	105,90
68,13	95,90	79,39	172,07
75,03	83,46		
77,71	78,48		
86,77	78,07		
Average	**73,83**	**Average**	**101,60**

Figure 30 shows the comparison and the presence of characteristic peaks from the CODINO-2206 database using the BiOCl specification card (00-101-1175) and the BiFeO$_3$ specification card (00-433-3972). By means of this information it is possible to evidence and corroborate that the structure of the hybrid catalyst is formed from the structures of its precursors, where the dominant precursor is BiOCl. This in turn allows corroborating that the synthesis method used for the present thesis is adequate, and that the variables used are suitable for the formation of the compound. Further analysis will allow corroborating the data obtained regarding the morphology and structure of the hybrid material, especially to corroborate the presence of the BiFeO$_3$ precursor.
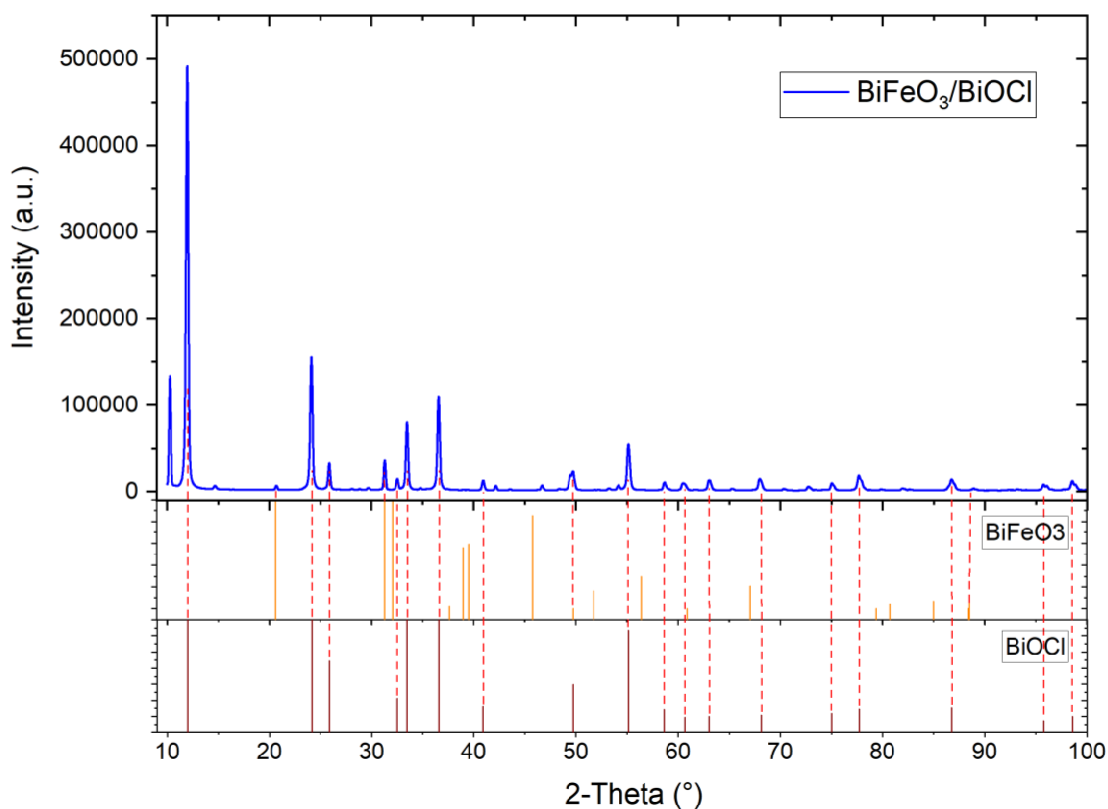
Figure 30. X-Ray Diffraction of the hybrid catalyst BiFeO₃/BiOCl

4.1.1.2. Fourier Transform Infrared Spectroscopy (FT-IR)

The Fourier transform infrared spectrum for the $BiFeO_3$ catalyst is presented in Figure 31. The spectrum is consistent with the literature references [88], [89]. In this context, the band located at 644 cm^{-1} corresponds to the bending vibrations of the Bi-O bond formed by FeO_6 octahedral groups. The band located at 806 cm^{-1} belongs to the stretching vibrations of the Fe-O bond of the tetrahedral building units forming the structure. The other band located at 1040 cm^{-1} corresponds to the vibrations of the C=O double bond, which appear due to the absorption of carbon from CO_2 by the exposure of the sample to air. Finally, the bands located at 1630 cm^{-1} and 3429 cm^{-1} correspond to the bending vibrations of the water molecules.
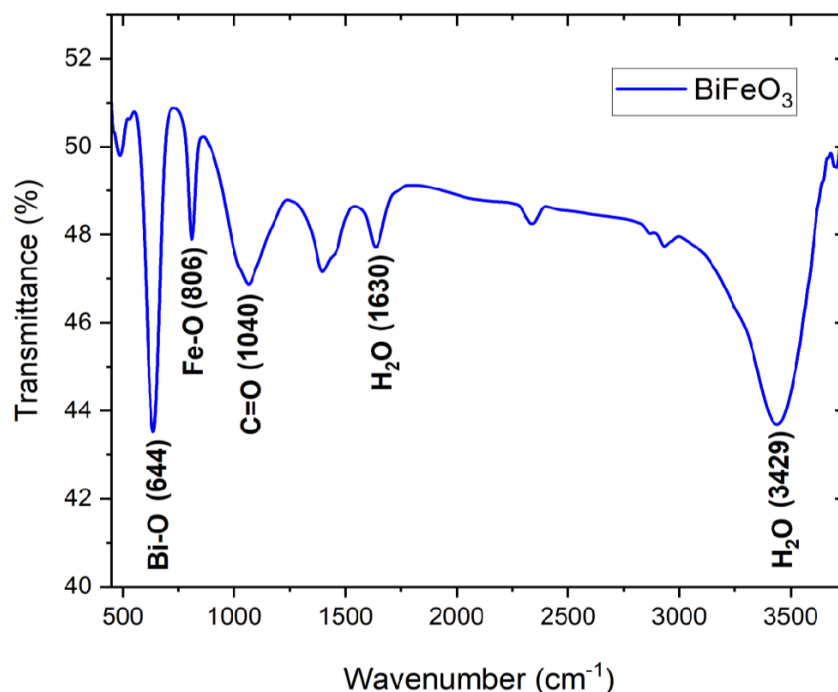
Figure 31. Fourier Transform Infrared Spectra of BiFeO₃

The FTIR spectrum for the BiOCl photocatalyst is presented in Figure 31. The spectrum is consistent with the literature references [53], [90], [91]. In the spectrum, the band located at 522 cm^{-1} corresponds to the symmetric A_{2u}-type valent stretching vibrations of the Bi- O bond, which denotes the high purity of the sample. Next, the bands at 1155 cm^{-1} and 1458 cm^{-1} correspond to the symmetric and asymmetric stretching vibrations of the Bi-Cl bond. Finally, the band located at 1623 cm^{-1} corresponds to the bending vibrations of the water molecules.
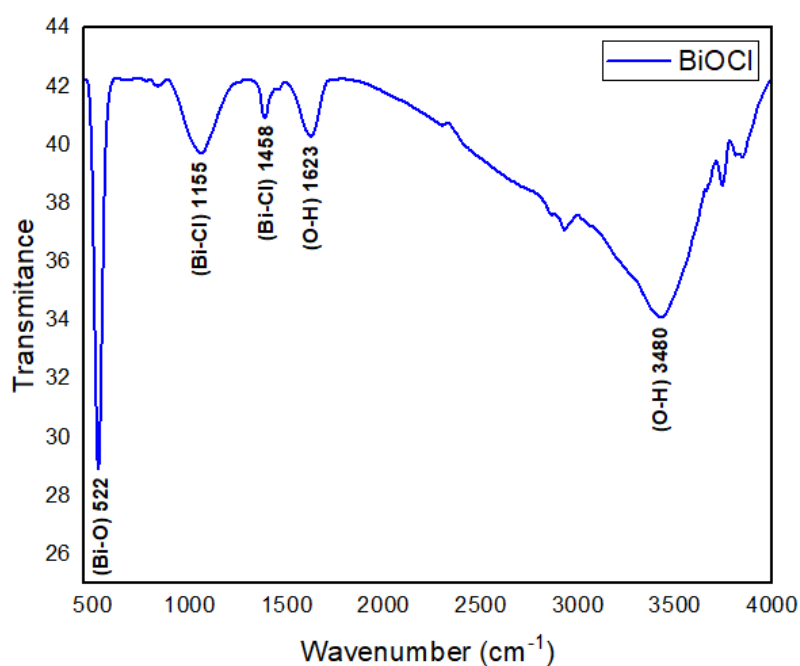
Figure 32. Fourier Transform Infrared Spectra of BiOCl

The Fourier transform infrared spectrum for the BiFeO₃/BiOCl hybrid catalyst is presented in Figure 33. This technique allows the analysis of the complete catalyst structure, since the photon beam passes completely through the matrix. Due to this characteristic, the hybrid presents the characteristic bands of BiOCl and BiFeO₃, as described in the previous sections.

The results obtained in the present section allow us to conclude that there is the formation of the characteristic bonds of each of the precursor catalysts. Likewise, the presence of the bonds of each precursor in the spectrum of the hybrid allows us to conclude that the synthesis of this new material was also carried out correctly. Additionally, the presence of a new band (1732 cm^{-1}) in the spectrum of the hybrid catalyst allows concluding that there is a chemical interaction between both precursors, forming a structure with new characteristics, which therefore has different properties. However, this must be supported with the techniques that are presented in the following sections.
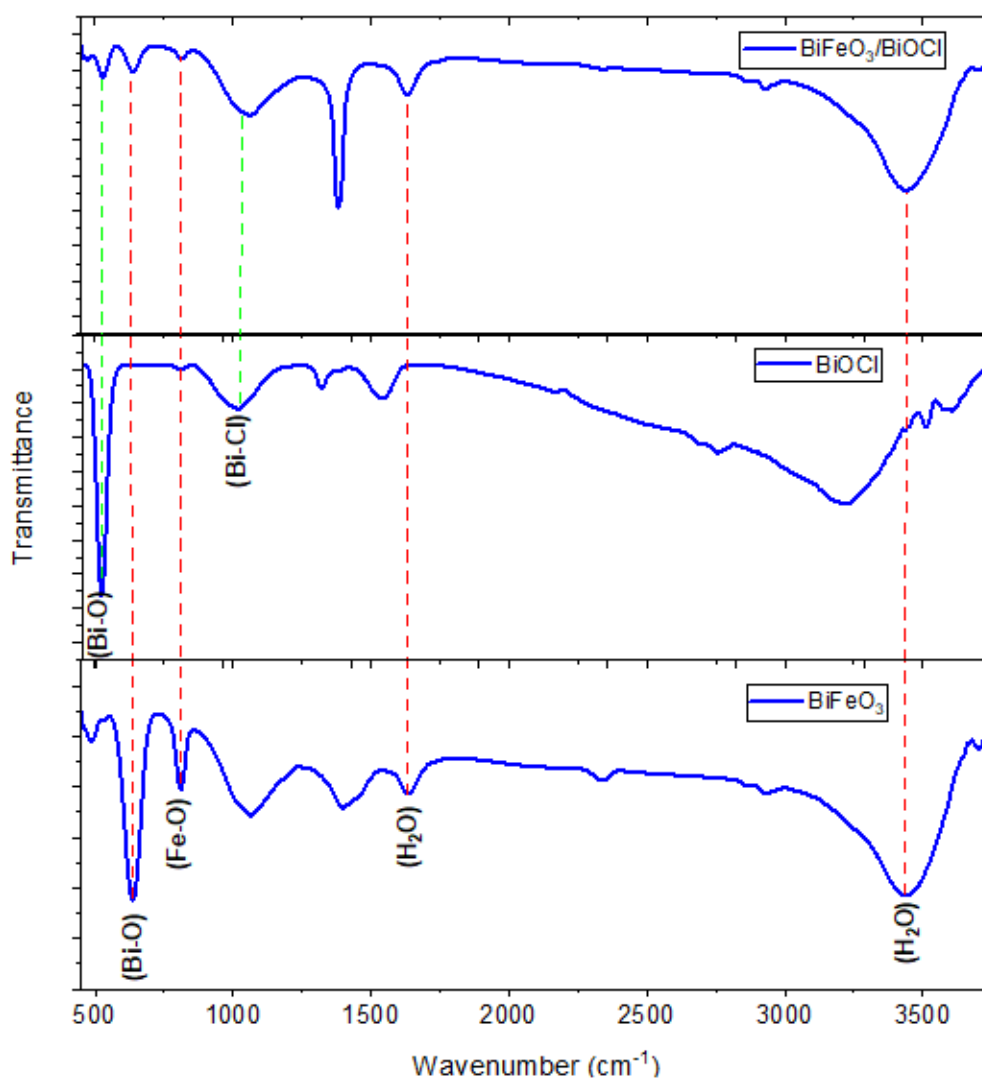
Figure 33. *Fourier Transform Infrared Spectra of the hybrid catalyst BiFeO₃/BiOCl*

4.1.1.3. X-Ray photoelectron spectroscopy (XPS)
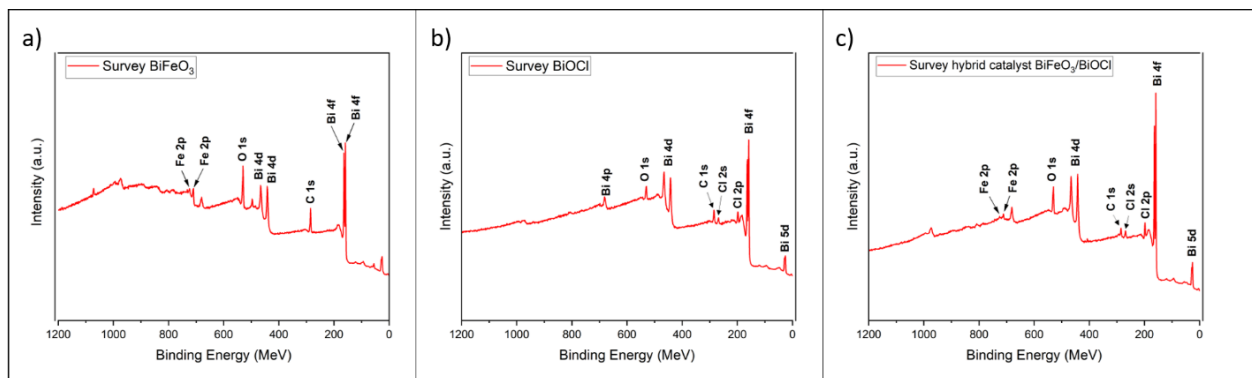
Figure 34. *XPS Survey spectrum for a) BiFeO₃, b) BiOCl and c) BiFeO₃/BiOCl*

To investigate the surface chemical composition and purity of the BiOCl photocatalyst, X-ray emitted photoelectron spectroscopy (XPS) measurements were carried out. The complete analysis of the sample, labeled Survey and presented in Figure 34, reveals the distinct presence of bismuth (Bi), chlorine (Cl) and oxygen (O). It is important to note that, prior to the analysis of the results, the binding energy of carbon at 284.5 eV was used as a reference to calibrate the positions of the peaks in all the XPS spectra.

Starting with the analysis, the characteristic peaks of Bi $4f_{7/2}$ and Bi $4f_{5/2}$ peaks at 159.00eV and 164.32 eV were identified, consistent with the oxidation state of bismuth (Bi^{3+}) in BiFeO₃ (Figure 35 a). On the other hand, for BiOCl were observed at 158.76 eV, 159.85 eV, 164.26 eV and 165.5 eV respectively, indicating the presence of bismuth in the Bi^{3+} oxidation state (Figure 35 b). For the hybrid catalyst BiFeO₃/BiOCl, the Bi 4f peaks at 158.97 eV and 164.3 eV are in line with the Bi 4f peaks observed in the BiFeO₃ and BiOCl precursors, indicating that bismuth retains its Bi^{3+} oxidation state in the hybrid (Figure 35 c).
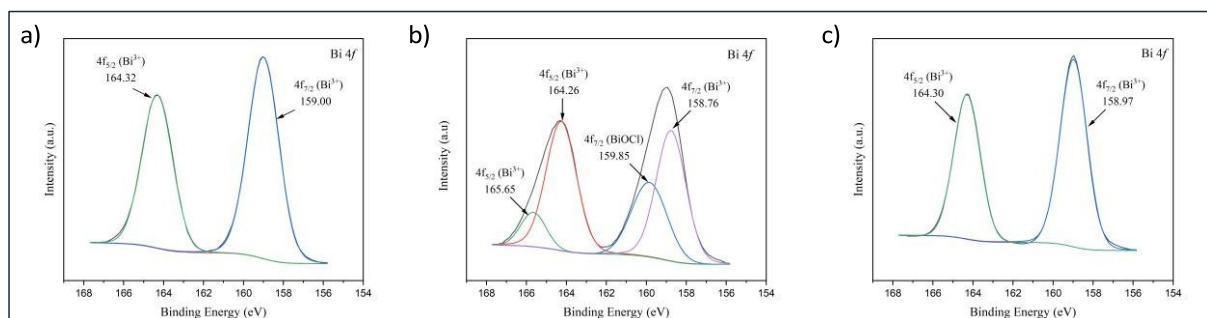
Figure 35. *High-resolution Bi 4f XPS spectrum for a) BiFeO₃, b) BiOCl and c) BiFeO₃/BiOCl*

With respect to the O 1s region, BiOCl exhibited two peaks at 530.92 eV and 532.85 eV, attributed to the presence of oxygen bonded with bismuth (O^{2-} in a Bi-O bond) (Figure 36 a). In this context, for BiFeO₃, O 1s peaks were observed at 529.73 eV and 531.49 eV, indicating the

presence of oxygen both in the crystal lattice (O^{2-}) and on the surface (adsorbed oxygen) (Figure 36 b). Also, for the hybrid catalyst $BiFeO_3/BiOCl$, the O 1s peaks at 531.00 eV and 533.33 eV, agree with the O 1s peaks observed in the precursors (529.2 eV and 531.2 eV), suggesting the presence of oxygen both in the crystal lattice and on the surface of the hybrid (Figure 36 c).
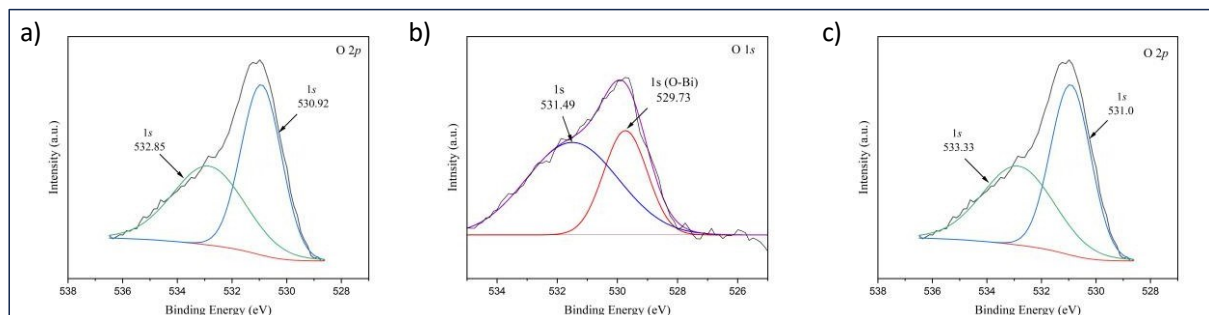
Figure 36. *High-resolution O 1s XPS spectrum for* a) *$BiFeO_3$,* b) *BiOCl and* c) *$BiFeO_3/BiOCl$*

The Fe 2p peaks for $BiFeO_3$, were detected at 710.41 eV and 724.42 eV, indicating the presence of Fe^{3+} in the compound, supported by the existence of a satellite peaks, located around 712.19 eV and 719.28 eV. The presence of this satellite peaks is a clear indication that the oxidation state of iron cannot be Fe^{2+}, since it is not energetically possible (Figure 37 d). On the other hand, the Fe 2p peaks at 709.35 eV and 723.5 eV in the hybrid are consistent with the Fe 2p peaks observed in the $BiFeO_3$ precursor, indicating the presence of iron in the Fe^{3+} oxidation state in the hybrid compound. The detection of the satellite peaks in the hybrid at 711.48 eV and 715.37 eV provides further confirmation of the iron oxidation state Figure 37 d).
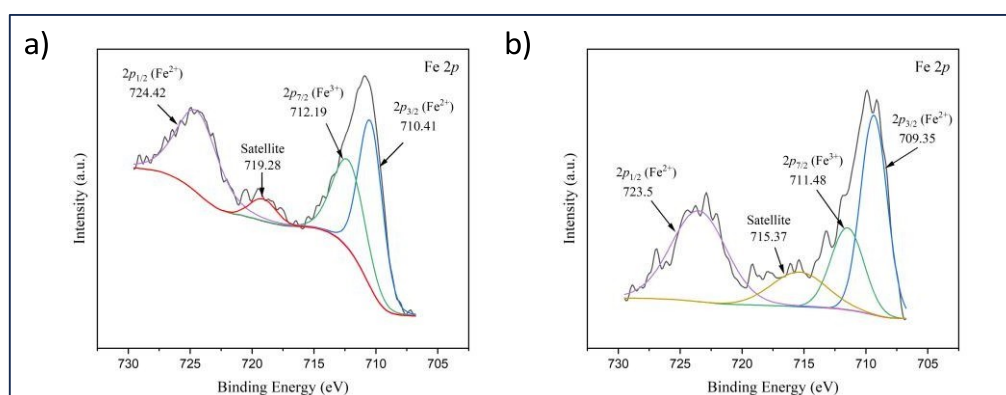
Figure 37. *High-resolution Fe 2p XPS spectrum for* a) *$BiFeO_3$,* b) *$BiFeO_3/BiOCl$*

The Cl $2p_{3/2}$ and Cl $2p_{1/2}$ peaks for BiOCl, were detected at 198.51 eV and 199.91 eV, respectively, confirming the presence of chloride with Cl^- oxidation state (Figure 38 a), evidencing the purity of the synthesized BiOCl. Finally, the Cl 2p peaks at 198.92 eV and 200.49 eV in the hybrid coincide with the Cl 2p peaks observed in the BiOCl precursor, suggesting the presence of chloride Cl^- in the hybrid compound (Figure 38 b).

49
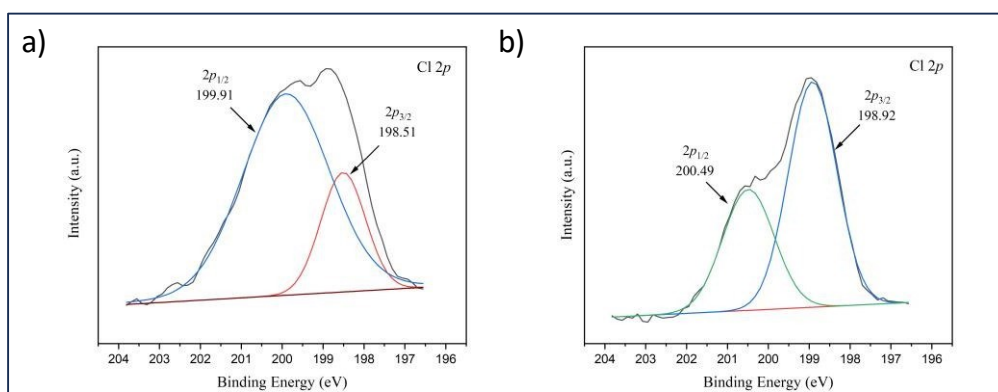
Figure 38. *High-resolution Cl 2p XPS spectrum for a) BiOCl, b) BiFeO₃/BiOCl*

4.1.1.4. Thermogravimetric analysis (TGA)

The thermogravimetric TGA analysis of the hybrid catalyst is shown in Figure 39. The curve obtained in the analysis shows that the catalyst is stable up to a temperature of 600 °C. From this point on, the curve begins to decrease, i.e., it starts to lose weight, until it reaches a temperature of 730°C, where it remains constant again, after losing approximately 20% of its weight. This behavior can be described by analyzing the thermogravimetric analysis of the precursors that make up the material. With respect to BiOCl, it has been reported that the TGA curve begins to lose weight at a temperature of 610 °C, due to the decomposition of BiOCl into bismuth monoxide (Bi-O) and chlorine gas (Cl_2). The material decomposes until it reaches a temperature of 800 °C, where it remains constant again after losing approximately 30% of its weight [92]. With respect to the precursor $BiFeO_3$, it has been reported that the TGA curve remains constant over the whole temperature range. Therefore, there is no decomposition of the structure of this catalyst [93].

The percentage loss of the hybrid catalyst is approximately 10% lower than the percentage loss of BiOCl. Additionally, BiOCl decomposes up to a temperature of 800 °C, whereas the hybrid decomposes up to a temperature of 730 °C. This is because the structure of the hybrid catalyst is composed of $BiFeO_3$ in a 1:1 ratio. The presence of this compound causes the weight loss of the hybrid and the degradation temperature to decrease.
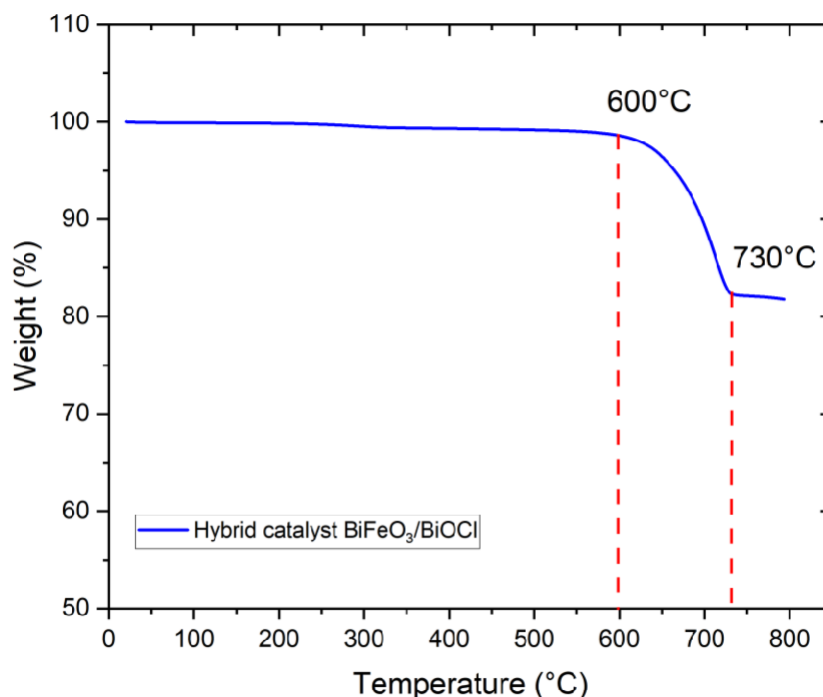
Figure 39. *Thermogravimetric analysis of the hybrid catalyst BiFeO₃/BiOCl*

4.1.2. Size and morphology analysis

4.1.2.1. Scanning electron microscope (SEM)

The images obtained by scanning electron microscopy (SEM) provide a detailed view of the structures at the nanometer level. In Figure 40 a), the nanosheets of the $BiFeO_3$ piezocatalyst are shown. In the image, several characteristic aspects of the nanosheets can be identified, such as their texture, surface and orientation. These details are crucial to corroborate the morphology of the material and how this can influence its performance. In Figure 40 b), an elemental analysis through Energy Dispersive Spectroscopy (EDS) is presented. In this spectrum, peaks corresponding to bismuth (Bi), iron (Fe) and oxygen (O) are observed, confirming the composition of the $BiFeO_3$ material. The clear presence of these elements is an indication that the synthesis of the catalyst was performed correctly.

Figure 40 c) shows an EDS elemental mapping of the surface of the material. In this image, the homogeneous distribution of the Bi, Fe and O elements can be observed, which reinforces the idea that the synthesis process was successful and managed to produce a uniform structure. Elemental mapping is essential to confirm the homogeneity and distribution of the components within the material and corroborates the results previously obtained by XRD, XPS, FT-IR, and TGA characterization techniques.
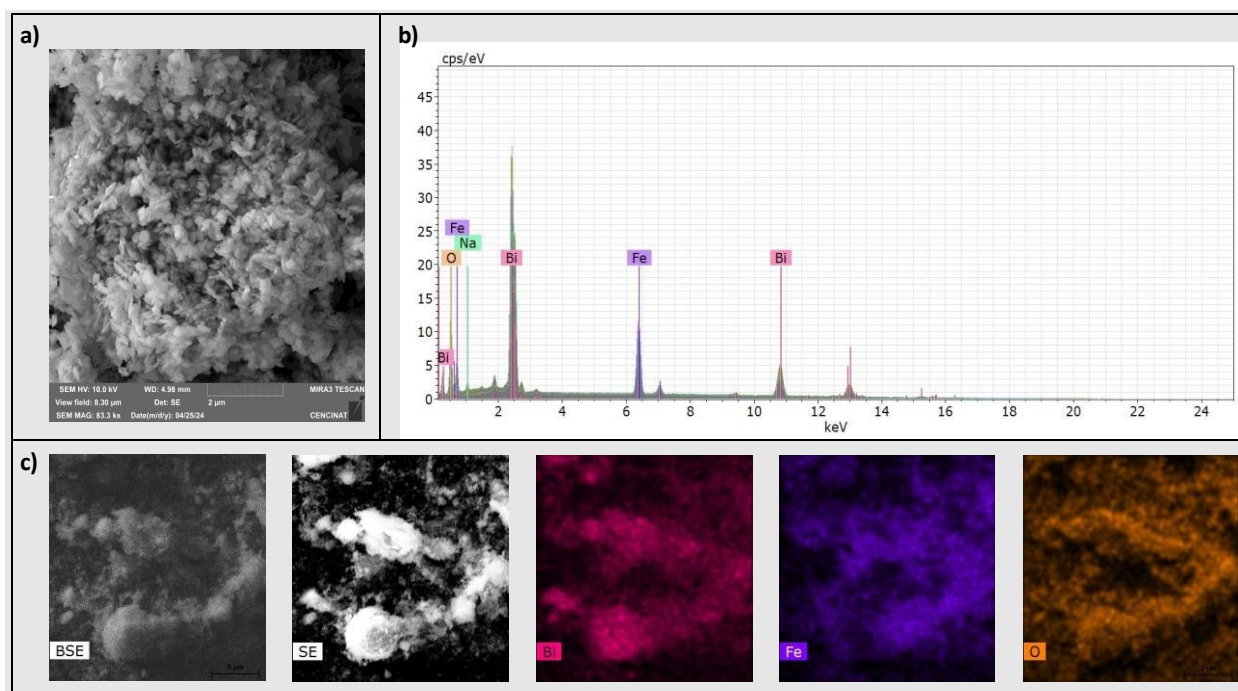
Figure 40. *Scanning Electron Microscope (SEM) and Energy Dispersive Spectroscopy (EDS) of BiFeO₃ nanosheets*

Analogous to the previous analysis, in Figure 41 (a), the presence of BiOCl photocatalyst microsheets is observed by scanning electron microscopy (SEM). Visual analysis of this image reveals key features such as morphology, size and arrangement of the microsheets. Notably, the microsheets show a considerable number of fractures and dislocations. Fractures in BiOCl microsheets can affect the accuracy of measurements made with techniques such as XRD, especially when calculating the average particle size using the Scherrer equation. When the microsheets are fractured, irregular surfaces are generated and internal parts of the material are exposed, which can modify the X-ray diffraction pattern.

In Figure 41 b), EDS spectrum is presented, showing the elemental composition of the material. Here, peaks corresponding to bismuth (Bi), chlorine (Cl) and oxygen (O) are identified, confirming that the synthesis produced the expected material, BiOCl. This elemental analysis is essential to validate the composition and ensure that the correct proportions of each element have been used. Finally, Figure 41 c) presents an EDS elemental mapping of the BiOCl surface. In this image, a uniform distribution of Bi, Cl and O elements is observed throughout the sample. This uniformity is a clear indication that the synthesis was successful and that the resulting material is homogeneous, a crucial quality for its performance in practical applications.
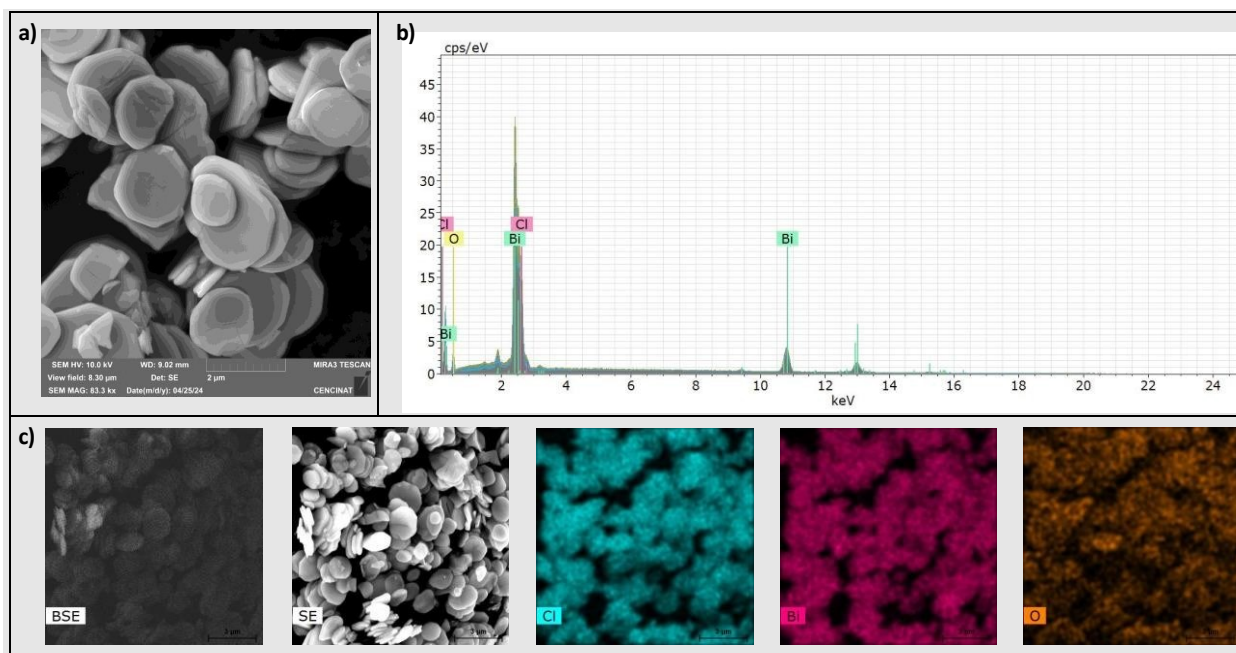
Figure 41. *Scanning Electron Microscope (SEM) and Energy Dispersive Spectroscopy (EDS) of BiOCl microsheets*

To conclude with this characterization technique, Figure 42 a) shows an image of the $BiFeO_3$/BiOCl hybrid catalyst obtained by scanning electron microscopy (SEM). In this image, the general morphology of the material is observed, highlighting the presence of well-defined microsheets that characterize the structure of the BiOCl matrix. In addition, a uniformly distributed texture of nanosheets can be noticed, suggesting the presence of $BiFeO_3$. According to the arrangement, it is considered that the $BiFeO_3$ nanosheets are mainly located in the interior of the hybrid material, while BiOCl forms the outermost surface.

Figure 42 b) presents EDS spectrum, showing the peaks with high intensity corresponding to the constituent elements of the hybrid catalyst. Prominent peaks for bismuth (Bi), chlorine (Cl), iron (Fe) and oxygen (O) are identified, confirming the presence of the characteristic elements of the hybrid catalyst $BiFeO_3$/BiOCl. This pattern of peaks is consistent with the SEM image, where $BiFeO_3$ appears to be mostly integrated within the BiOCl structure, which is evidence of an optimization in the structure, favoring the catalytic photo-piezo processes.

Finally, in Figure 42 c), an EDS elemental mapping of the hybrid catalyst is presented. This mapping shows the distribution of the elements: bismuth (Bi), iron (Fe), chlorine (Cl) and oxygen (O), on the surface of the material. A homogeneous distribution of bismuth, chlorine and oxygen is observed, confirming the predominant external composition of BiOCl. However, iron appears with less intensity and in a more localized form, suggesting that $BiFeO_3$ is mostly within the matrix, with less presence on the surfaces. These results are important, as they indicate that the

hybrid catalyst is composed of both precursors, $BiFeO_3$ and $BiOCl$, but with a structure where $BiFeO_3$ is encapsulated.

This analysis corroborates the absence of many peaks corresponding to $BiFeO_3$ in the XRD spectrum of the hybrid catalyst, since the photons emitted by the equipment do not reach the internal structure of the sample due to the presence of $BiOCl$. Additionally, this analysis has helped to understand the formation and synthesis of the hybrid catalyst $BiFeO_3/BiOCl$. In this context, the results obtained indicate how the elements are distributed and where the precursors are located within the matrix of the hybrid, which provides a solid basis to support the proposed mechanism for the photo-piezo catalysis process. This information is also key to provide a substantiated explanation for the optimization of the catalyst performance.
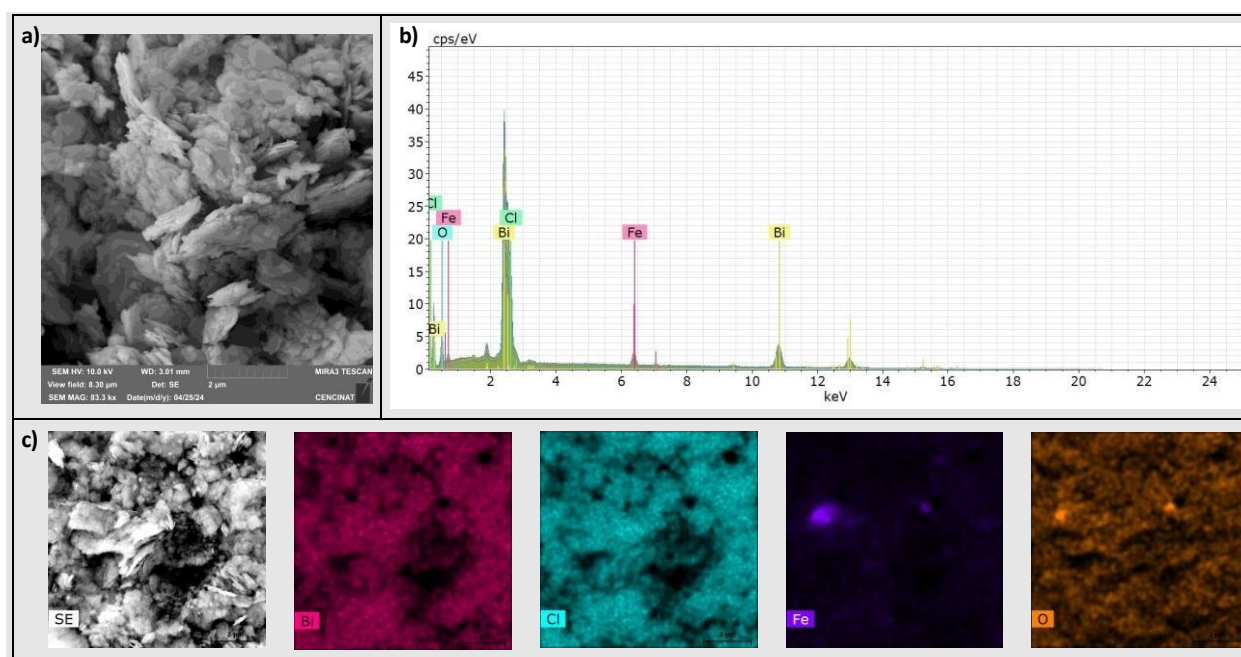
Figure 42. *Scanning Electron Microscope (SEM) and Energy Dispersive Spectroscopy (EDS) of the hybrid catalyst BiFeO₃/BiOCl*

To compare the particle size of the hybrid catalyst, SEM images of both precursors, $BiFeO_3$ and $BiOCl$, as well as the $BiFeO_3/BiOCl$ hybrid catalyst were used (see Figure 43). ImageJ measurement software was used to analyze these images, with a scale reference of 500 nm. As shown in Table 8, for each sample, 10 measurements were performed to obtain an average of the particle size values. The analysis yielded that the average particle size of the BiOCl particles was 2602.21 nm, while the average particle size of the $BiFeO_3$ particles was 96.42 nm. In the case of the hybrid catalyst, the average particle size was 1103.19 nm.

The analysis of these results is congruent with the nature of the hybrid catalyst, as it combines the structure of both precursors. The average particle size for the hybrid reflects the mixture of

BiFeO$_3$ nanosheets and BiOCl microsheets. Also, the BiFeO$_3$ particle size obtained with SEM agrees with the values obtained by XRD and the Scherrer equation, which is consistent with the neat and clean structure presented by the nanosheets of this material. However, the particle size of BiOCl derived from SEM analysis is considerably larger than that obtained by XRD and Scherrer equation. This may be attributed to fractures and dislocations in the BiOCl microsheets, which can affect the accuracy of XRD measurements and lead to inaccurate estimates.
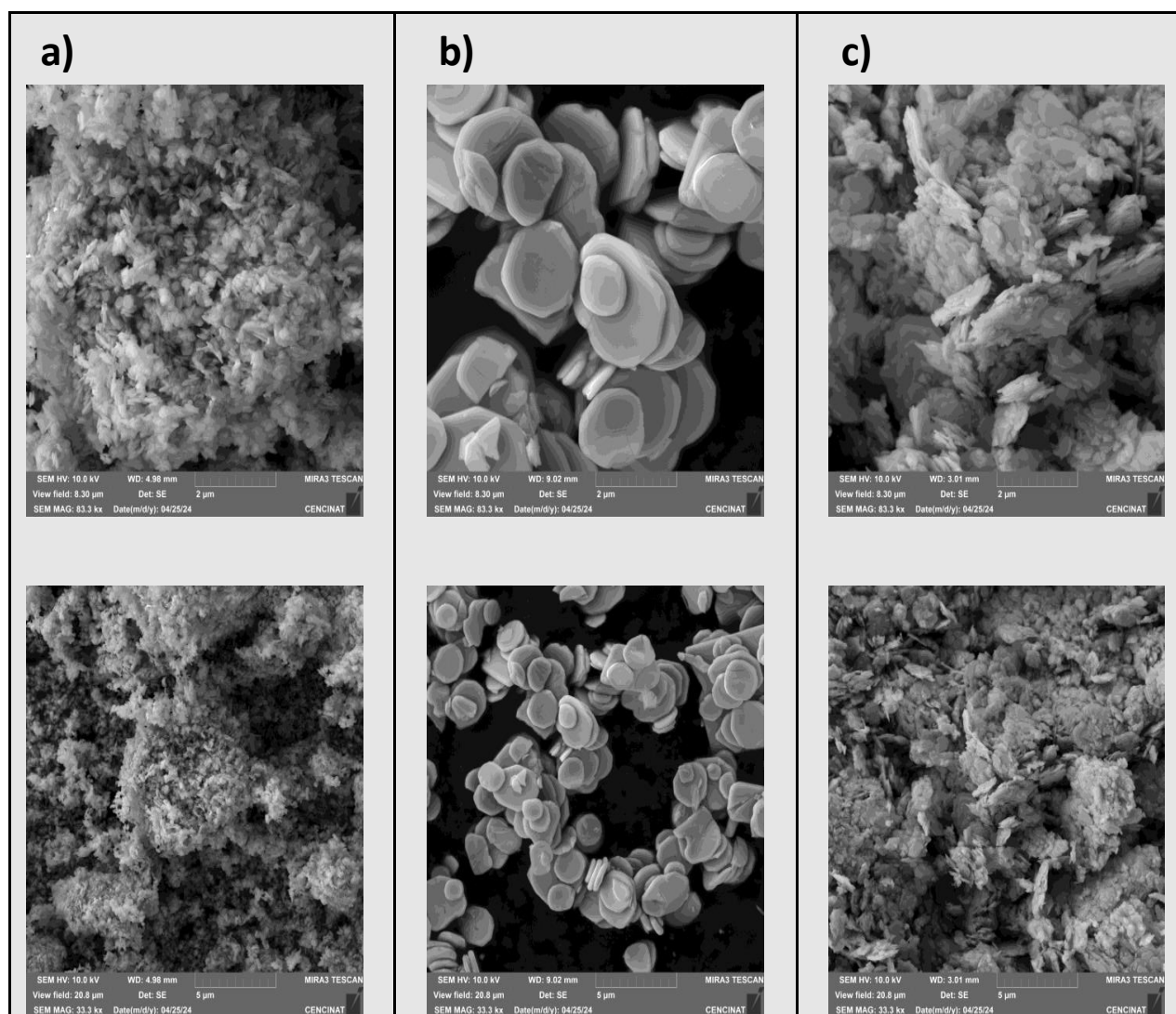
Figure 43. *Comparison of particle size (SEM) for a) BiFeO$_3$ (2μm and 5μm), b) BiOCl (2μm and 5μm), and c) BiFeO$_3$/BiOCl (2μm and 5μm)*

Table 8. *Particle size for BiFeO₃, BiOCl, and BiFeO₃/BiOCl using SEM images*

	BiOCl	BiFeO$_3$	BiFeO$_3$/BiOCl
	Size (nm)	Size (nm)	Size (nm)
1	1735.38	127.97	303.06
2	3368.69	102.43	240.78
3	3452.40	110.53	430.77
4	3359.06	77.74	1332.80
5	2223.41	98.72	1344.92
6	1437.44	108.29	916.68
7	1293.50	56.78	1887.92
8	3244.99	96.65	1589.22
9	2541.73	85.48	1587.20
10	3365.50	99.56	1398.53
Average	2602.21	96.42	1103.19

4.1.3. Band gap energy analysis (Diffuse reflectance spectroscopy)

The band gap (Eg) of the precursors BiFeO$_3$, BiOCl, and the hybrid catalyst BiFeO$_3$/BiOCl is estimated from optical absorption edge, obtained from the reflectance spectrum. As mentioned in the methodology, Eg is determined from the linear deviation plot, where the y-axis is represented by the function $(Fh\upsilon)^2$, while the x-axis is the photon energy (hυ). The band gap of the BiFeO$_3$ piezocatalyst is found to be estimated at 2.48 eV (see Figure 44 a)), which is consistent with the values reported in the literature. This Eg value is important because it allows us to determine that the material was synthesized properly, and verifies its piezocatalytic properties reported in the literature [94], [95].

On the other hand, the band gap of the BiOCl photocatalyst is estimated to be 3.5 eV (Figure 44 b). This band gap value allows it to absorb part of the UV-Vis spectrum and visible spectrum, generating electron-hole pairs when exposed to radiation. In this context, the information reported in the literature reinforces and corroborates the results described above. With this, it supports the fact that the BiOCl synthesis process was carried out properly, and that the material has photocatalytic properties with activation with visible light source, as described previously [96], [97].

Finally, the band gap of the BiFeO$_3$/BiOCl hybrid material presents two different values, clearly indicating the combination of these two compounds (Figure 44 c)). The first value, 2.3 eV, corresponds to the BiFeO$_3$ piezocatalyst, while the second, 2.78 eV, is associated with the BiOCl photocatalyst. These data suggest that the hybrid material has succeeded in integrating the properties of both precursors. In this sense, the reduction in the band gap is remarkable in the case

of BiOCl, which decreases from 3.5 eV to 2.78 eV. This reduction of 0.72 eV means that the hybrid material requires less energy to be activated, which makes it more suitable for light absorption in the visible spectrum. Thus, we conclude that, the $BiFeO_3/BiOCl$ hybrid not only has the ability to be activated by visible light due to the reduction in the band gap, but can also be activated by ultrasound, a characteristic property of $BiFeO_3$. This dual activation capability significantly expands the potential applications of the hybrid material in various fields, such as water purification and pollutant degradation. These band gap values also confirm that the synthesis process has been successful, achieving an effective combination of the properties of both precursors.
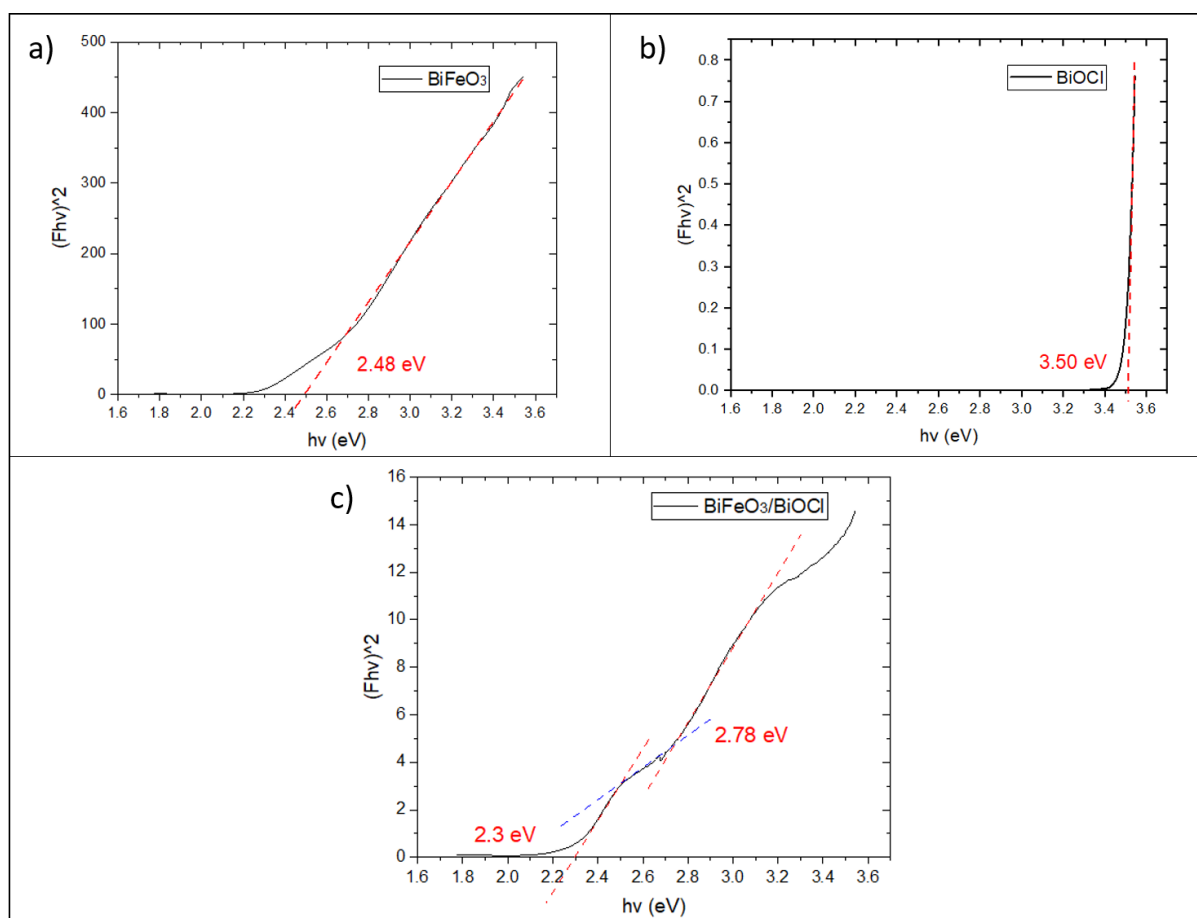
Figure 44. *Tauc plots for the band gap estimation of BiFeO₃, BiOCl and the hybrid catalyst BiFeO₃/BiOCl*

4.2. Design and fabrication of the reactors for photocatalytic and piezocatalytic tests

4.2.1. Photodegradation of TiO₂

To verify the wavelength range of the light source used in our reactors, we performed photodegradation experiments with RhB using titanium dioxide (TiO_2) in its anatase form as a catalyst. Since TiO_2 is activated only under ultraviolet (UV) light, its response can serve as an indicator of the presence of UV light. However, our results showed that, during the experiments,

the absorbance and concentration of RhB remained constant, suggesting that the catalyst was not activated (see Figure 45 a and b). These results are significant because they indicate that the light source in our reactors emits in the visible range 400 nm to 700 nm, not including UV light emissions that could activate TiO_2.
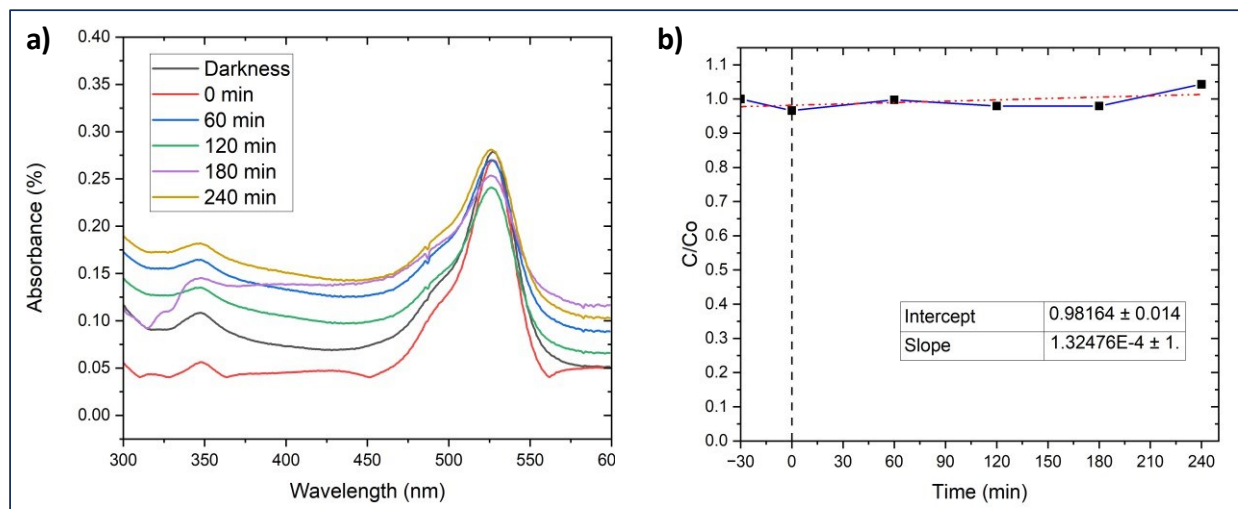
Figure 45. *Photocatalytic degradation of RhB with TiO$_2$*

4.2.2. Photolysis of RhB

To ensure that the light source used in our reactors alone was not responsible for the degradation of RhB through a photolysis process, we performed a control experiment in which RhB was exposed to the light source without the presence of a catalyst. The results obtained are represented in Figure 46 a) for the absorbance graph and Figure 46 b) for the concentration graph, which showed that both measurements remained constant throughout the exposure time. This result suggests that the light source, in the absence of a catalyst, had no degrading effect on RhB, thus indicating that no photolysis occurred.
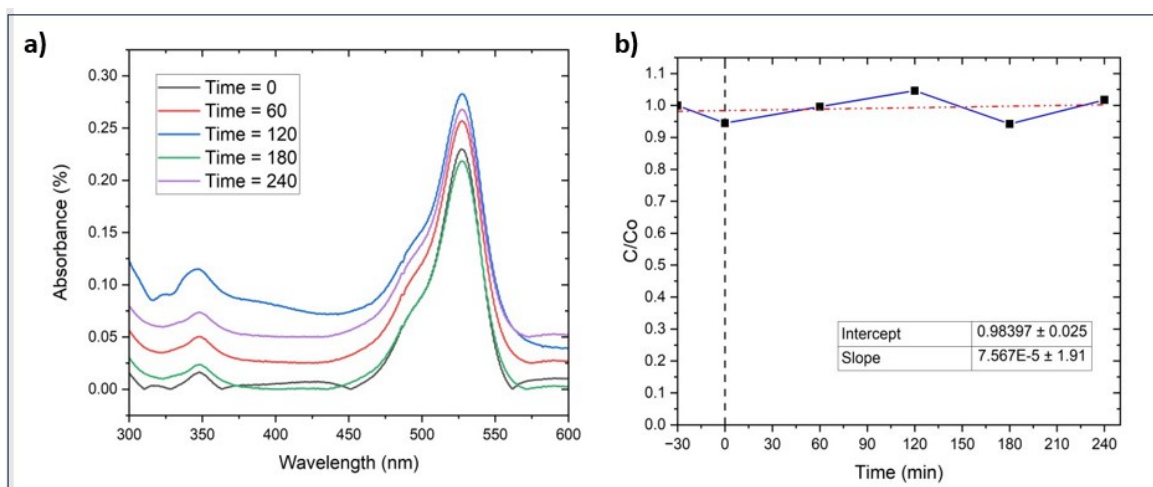
Figure 46. *Photolysis of RhB*

4.2.3. Characterization of the LED light source

The result of the emission spectrum of the lamp used in the photocatalytic reactor confirms that this light source operates only in the visible light range, with no emissions in the ultraviolet region. The analysis showed that the peak of maximum intensity is at approximately 450 nm, indicating that the emitted light has a predominantly blue hue. However, the combination of emissions in the blue, green and red regions generate the white color characteristic of this type of LED spotlight (Figure 47). This result has important implications for the design and use of the photocatalytic reactor, as it validates that the light source does not produce ultraviolet radiation, reducing the risk of activating UV-sensitive catalysts or causing unwanted effects. In addition, the emission of white light suggests that the reactor could be suitable for applications requiring this specific type of illumination.
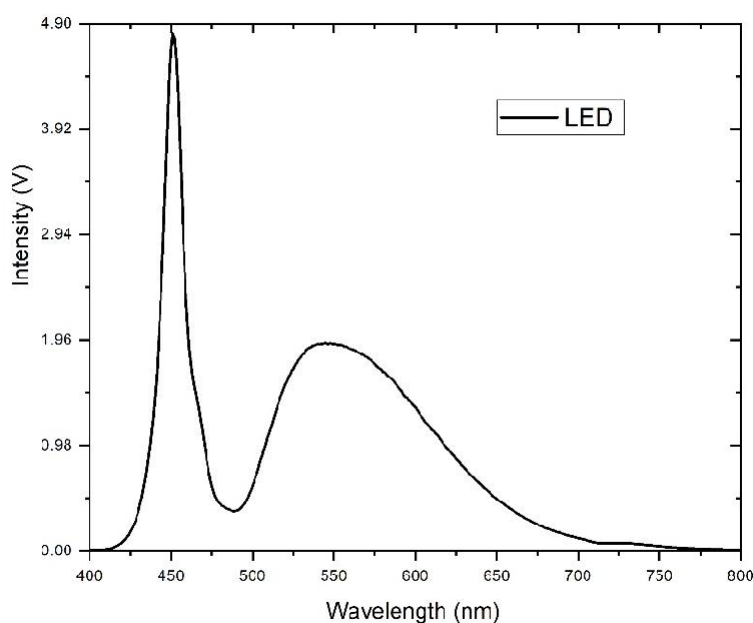
Figure 47. *LED light source emission spectrum*

4.3. Calibration curve with Rhodamine B (RhB)

The validation of the calibration curve was confirmed by applying a linear regression to the absorbance measurements versus the concentration of the calibration solutions. The high R^2 value obtained, which was 0.9919, indicated a correct and consistent fit of the data to the regression line. The resulting equation, $y = 1.2907x$, establishes the relationship between absorbance and RhB concentration (Figure 48). From this equation, it was possible to calculate the absolute C/C_0 concentration in the degradation plots in the subsequent sections, thus allowing an accurate interpretation of the behavior of the degradation process.
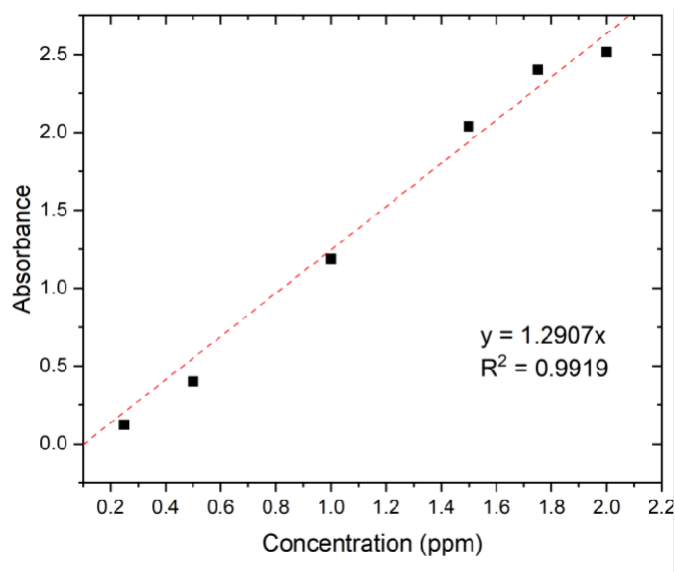
Figure 48. *Calibration curve of Rhodamine B (RhB)*

4.4. Photocatalytic activity test

4.4.1. Photocatalytic degradation of RhB with BiOCl and BiFeO₃/BiOCl (hybrid)

In this section, photocatalytic tests were carried out to evaluate the degradation efficiency of RhB at an initial concentration of 2 ppm, using two different catalysts: the photocatalyst and precursor BiOCl and the hybrid catalyst BiFeO₃/BiOCl. The ratio between the final concentration and the initial concentration (C/Co), obtained from the calibration curve of the previous section, was used to measure the progress of the degradation process, representing it in a graph as a function of time, which for the present process is 4 hours and 30 minutes.

During the first 30 minutes of agitation in complete darkness, a stage aimed at achieving adsorption-desorption equilibrium, no degradation occurs, but it was observed that BiOCl adsorbed part of the RhB, reducing the concentration from 1 to 0.65. That means a 35% of RhB remotion via adsorption. Then, when the light source was turned on to start the photocatalytic process, the degradation of RhB started and progressed, reaching a C/Co of 0.18 at the end of 4 hours of the experiment. Thus, BiOCl degraded 82% of RhB in 4 hours (see Figure 49).

On the other hand, the hybrid catalyst BiFeO₃/BiOCl also showed adsorption during the equilibrium period, reducing the RhB concentration from 1 to 0.61. That means a 39% of RhB remotion via adsorption. Then, after 4 hours of irradiation, the photocatalytic process degraded RhB to a C/Co of 0.11. Although the differences between the two catalysts were not drastic, the hybrid showed a slight higher efficiency in the degradation of RhB (89 % in 4 hours), suggesting that the combination of BiFeO₃ and BiOCl may be more effective for photocatalysis (Figure 49).

60
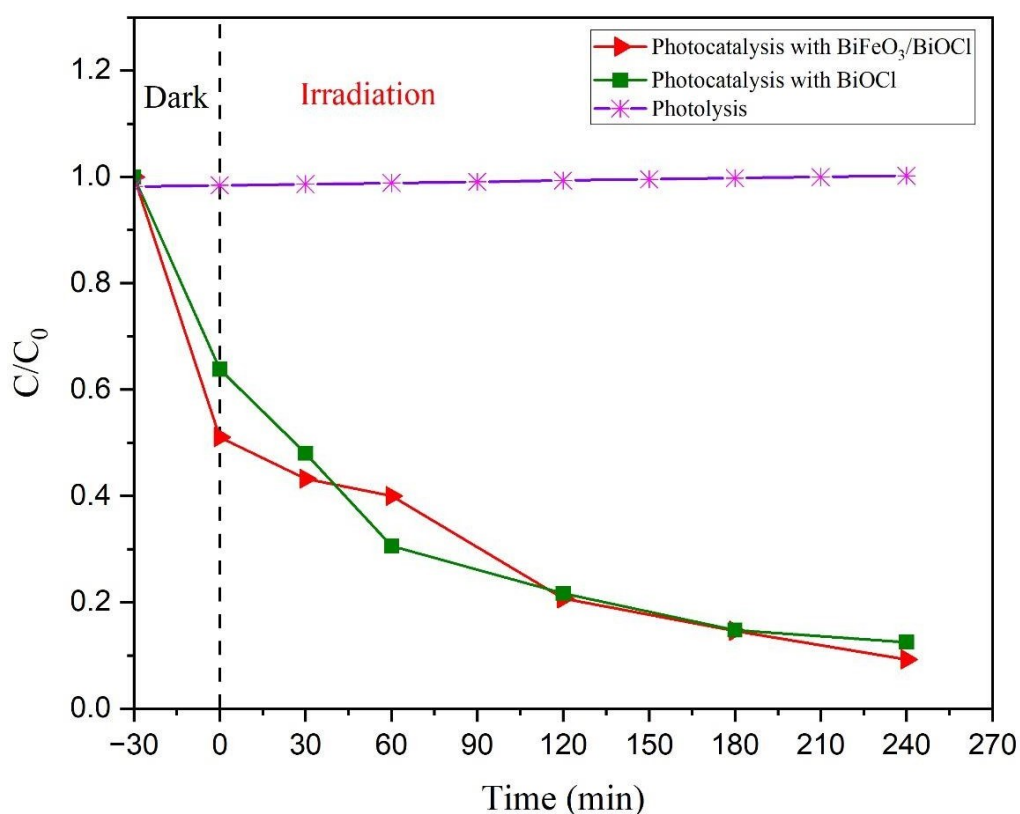
***Figure 49.** Photocatalytic degradation of RhB with BiOCl vs BiFeO₃/BiOCl*

4.5. Piezocatalytic activity test

4.5.1. Piezocatalytic degradation of RhB with BiFeO₃ and BiFeO₃/BiOCl (hybrid)

Analogous to the experimentation described above, the piezocatalysis reactions were performed. To compare the performance of the piezocatalyst to degrade the RhB dye at 2 ppm, the piezocatalyst $BiFeO_3$, a precursor of the hybrid catalyst, and the hybrid catalyst $BiFeO_3/BiOCl$ were used. The experiment started with 30 min of stirring in the dark to reach adsorption-desorption equilibrium, followed by activation of the ultrasound source to initiate the piezocatalysis process. During the adsorption-desorption period, the $BiFeO_3$ catalyst showed a decrease in RhB concentration from 1 to 0.92, suggesting a small adsorption capacity. After 4 hours of ultrasound activation, the catalyst reduced the RhB concentration to a C/Co of 0.5, managing to degrade 50% of the dye. This level of degradation is significant and demonstrates that $BiFeO_3$ alone has piezocatalytic properties, although its performance can be improved.

In contrast, the hybrid $BiFeO_3/BiOCl$ catalyst showed a higher adsorption capacity, reducing the RhB concentration from 1 to 0.58 during the adsorption-desorption equilibrium period (42%). Then, after 4 hours of ultrasound activation, the piezocatalytic process allowed a more efficient degradation, reaching a C/Co of 0.38, equivalent to 62% of the degraded RhB. This difference between the two catalysts suggests that the hybrid, with its combination of $BiFeO_3$ and BiOCl,

offers higher efficiency, possibly due to its ability to mobilize charges and facilitate the formation of hole-electron pairs. Although piezocatalysis, in general, is less efficient than photocatalysis, the hybrid catalyst demonstrated superior performance (Figure 50).
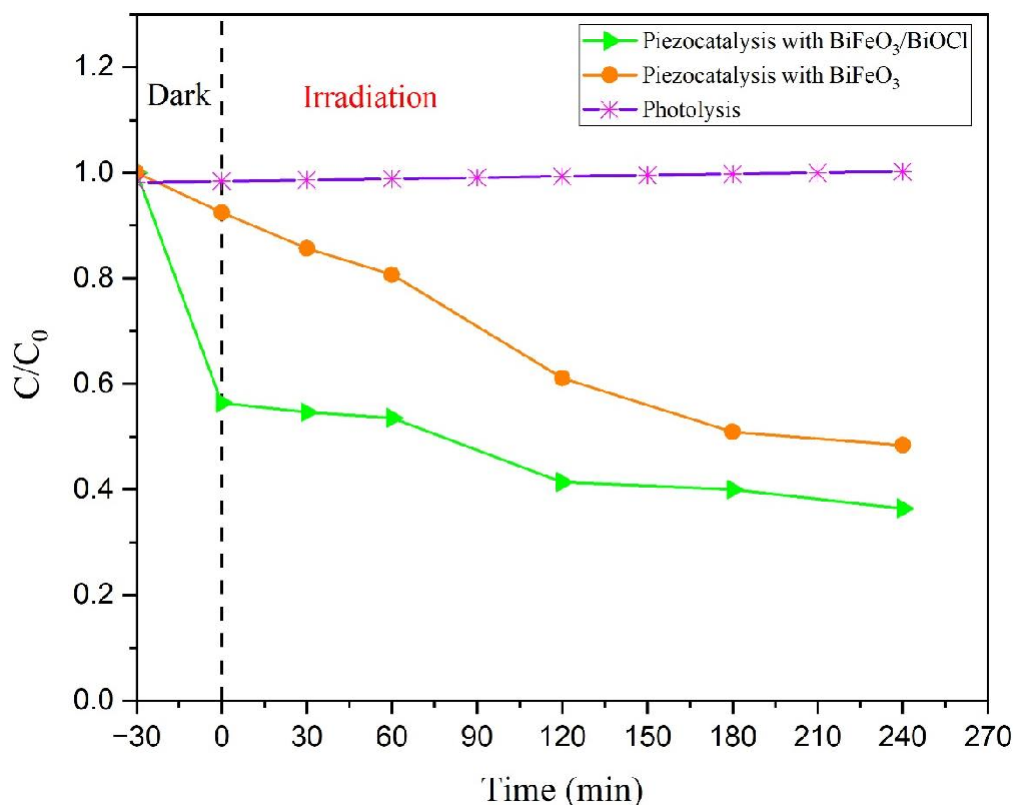
Figure 50. *Piezocatalytic degradation of RhB with BiFeO₃ vs BiFeO₃/BiOCl*

4.6. Photo-piezo catalytic activity test

4.6.1. Photo-piezo catalytic degradation of RhB with BiFeO₃/BiOCl (hybrid)

For the study of the catalytic photo-piezo activity with the hybrid catalyst BiFeO$_3$/BiOCl, the same experiment described in the previous sections was carried out. That is, to evaluate the degradation of the RhB dye at 2 ppm. The process started with a 30-min dark period to reach adsorption-desorption equilibrium, during which the hybrid showed significant adsorption capacity, reducing the RhB concentration from 1 to 0.6. Next, the visible light source and ultrasound were activated simultaneously to initiate the photo-peep catalysis process. Within the first hour of exposure, the hybrid succeeded in degrading RhB to a C/Co of 0.22. That is, 78% of RhB was degraded, evidencing a powerful catalytic photo-piezo effect. During the next three hours of activation, the degradation continued until it reached a C/Co of 0.0, which is equivalent to 95% degradation of RhB. This demonstrates the high efficiency of the BiFeO$_3$/BiOCl hybrid catalyst (Figure 51).
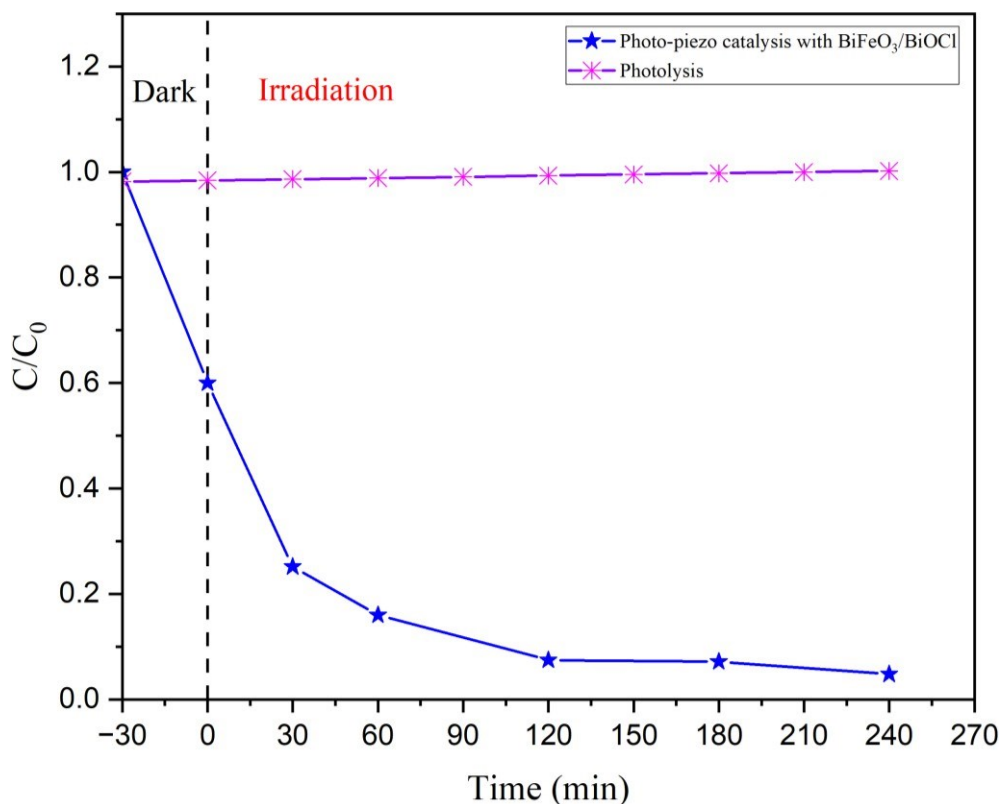
Figure 51. Photo-piezo catalytic degradation of RhB with BiFeO₃/BiOCl

4.7. Comparison of catalytic process with BiFeO₃/BiOCl hybrid

To compare the degradation efficiency, a graph combining the results of photocatalysis with BiOCl, piezocatalysis with BiFeO₃, and photo-piezo catalysis with the BiFeO₃/BiOCl hybrid catalyst was generated. Analogous to the previous results, the data in the graph are presented as C/Co as a function of time, reflecting the efficiency of each process in the degradation of RhB.

In the case of photocatalysis with BiOCl, a reduction of RhB concentration from 1 to 0.18 was observed, achieving 82% degradation after 4 hours and 30 minutes of experimentation. For piezocatalysis with BiFeO₃, degradation was less effective: after 4 hours of ultrasound activation, the concentration ratio reached a value of 0.5. That is, 50% of the dye was degraded. On the other hand, when performing the catalytic photo-piezo process with the hybrid catalyst BiFeO₃/BiOCl, the performance was significantly higher. After the initial 30 min adsorption period, the C/Co was reduced from 1 to 0.6. With simultaneous light and ultrasound activation for 4 hours, the degradation of RhB continued up to a C/Co of 0.05, which means that 95% of the dye was degraded (see Figure 52).

These results show a significant difference between the three methods. The BiFeO₃/BiOCl hybrid catalyst, by photo-piezo catalysis, achieved the highest degradation efficiency,

outperforming both BiOCl photocatalysis and BiFeO₃ piezocatalysis. The difference in performance is remarkable: photo-piezo catalysis achieved 13% more degradation than photocatalysis and 45% more than piezocatalysis. This may be due to the ability of the hybrid to mobilize charges (polarization) and the formation of hole-electron pairs, which enhances the catalytic activity. These results suggest that the hybrid is a promising option for applications requiring highly efficient degradation, such as dye and bacterial degradation.
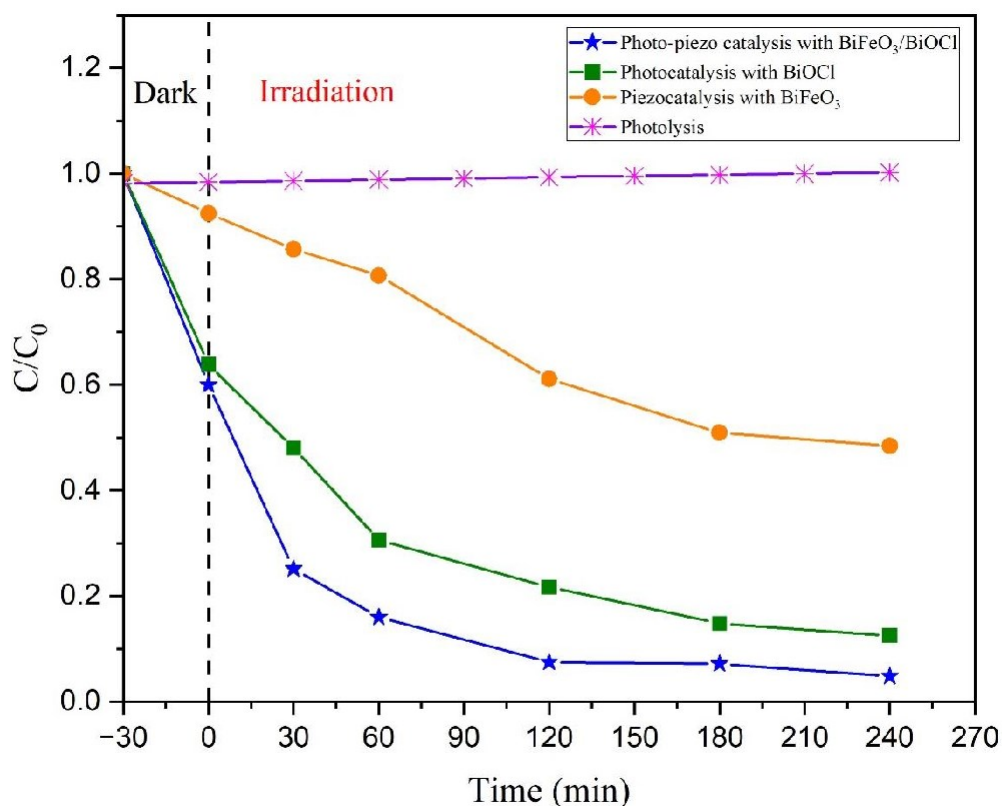
Figure 52. *Comparison of catalytic process of BiOCl and BiFeO₃ with BiFeO₃/BiOCl*

A graph was generated to compare the degradation efficiency of the RhB dye through photocatalysis, piezocatalysis and photo-piezo catalysis, using only the hybrid catalyst BiFeO₃/BiOCl. In the case of photocatalysis with the hybrid, it was observed that after 30 minutes of adsorption, the concentration ratio was reduced from 1 to 0.6. Then, during the 4 hours of irradiation with the light source, the degradation reached a value of 0.1, achieving a 90% degradation of the dye. On the other hand, in the piezocatalysis, after 30 minutes of adsorption, the C/Co was reduced to 0.56. Then, after 4 hours of ultrasound activation, the piezocatalytic process degraded RhB to a value of 0.42, representing 58% degradation.

Finally, in the photo-piezo catalysis process, the BiFeO₃/BiOCl hybrid showed the highest efficiency. After 30 minutes of adsorption, the C/Co was reduced to 0.53. Then, by combining

irradiation with visible light and ultrasound for 4 hours, the degradation of RhB reached a C/Co of 0.05, managing to degrade 95% of the dye. This level of performance exceeds both photocatalysis and piezocatalysis performed with the hybrid alone. The difference in performance is remarkable: the photo-piezo catalysis process achieved 5% more degradation than photocatalysis and 37% more than piezocatalysis (Figure 53).
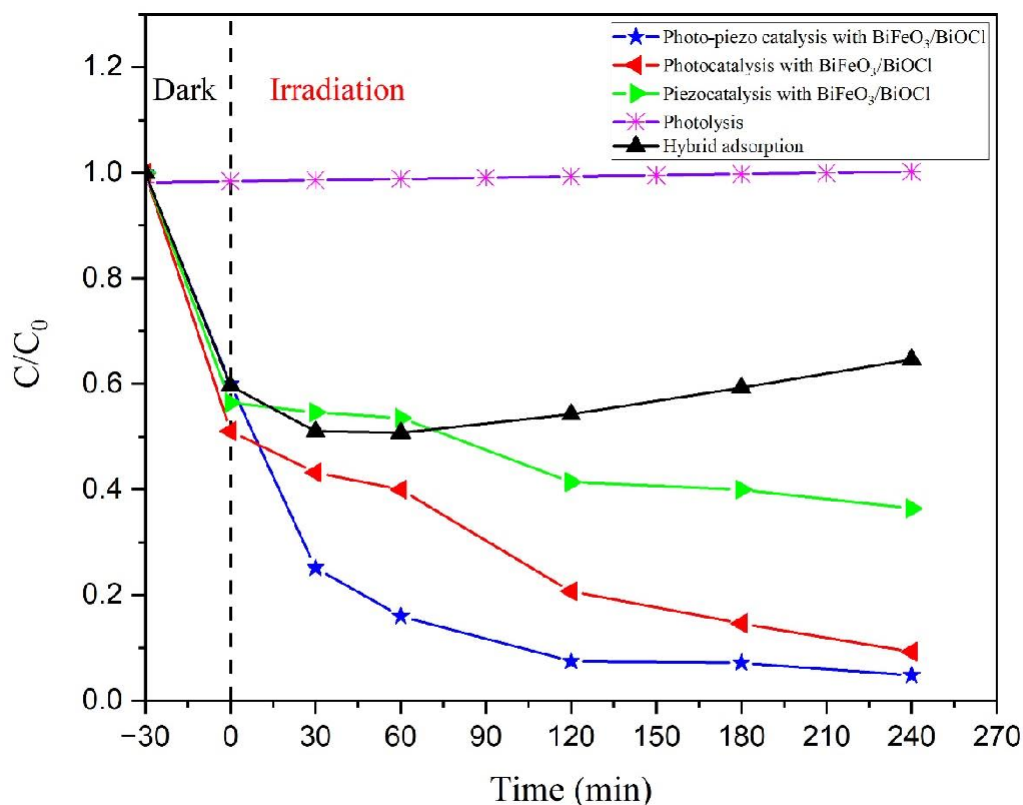
Figure 53. *Comparison of photocatalytic, piezocatalytic and photo-piezo catalytic process with BiFeO$_3$/BiOCl*

4.8. Point of zero charge

The point of zero charge (PZC) of the BiFeO$_3$/BiOCl hybrid catalyst was determined as pH 4, which means that at this pH level the surface of the material has no net charge, balancing positive and negative charges (see Figure 54). This value has important implications for the proper functioning of the catalyst, as it indicates how it will behave in different pH environments. That is, in solutions with a pH below 4, the catalyst will tend to have a net positive charge, which makes it more effective in adsorbing negatively charged species, such as some anionic contaminants like RhB. On the other hand, when the pH of the environment is above 4, the catalyst will have a net negative charge, making it more suitable for attracting and adsorbing positively charged species, such as metal cations. Thus, the result of the PZC at pH 4 suggests that the use of the hybrid catalyst BiFeO$_3$/BiOCl should be adapted according to the pH of the medium in which it is used and may

be useful to optimize its efficiency in applications such as water treatment or pollutant degradation.
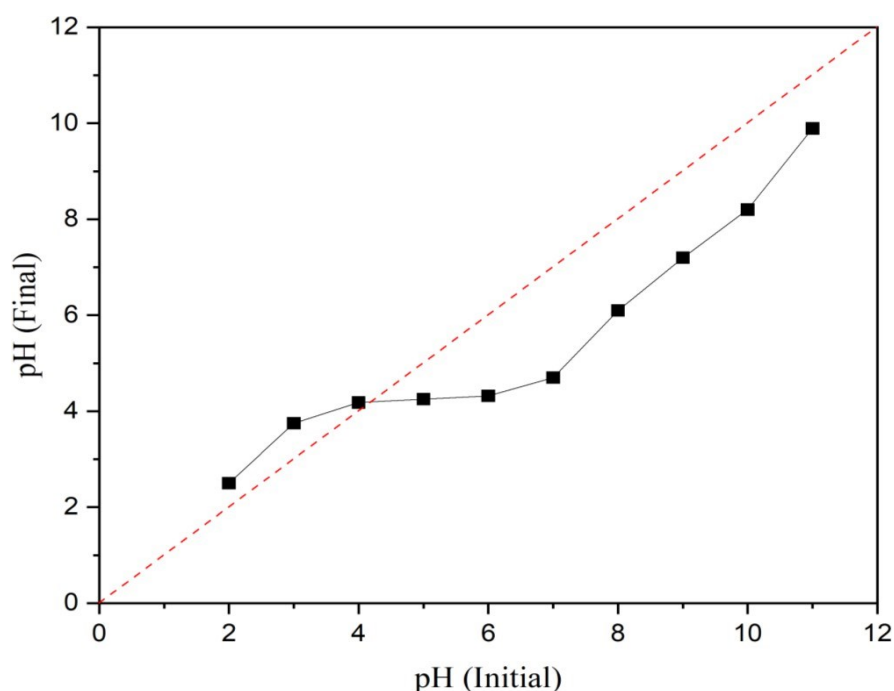
Figure 54. Point of Zero Charge (PZC) of the hybrid catalyst BiFeO₃/BiOCl

4.9. Antibacterial activity of BiFeO$_3$/BiOCl hybrid

4.9.1. Disk-diffusion assay

During the evaluation of bacterial disinfection using the Kirby-Bauer disk diffusion technique, extremely small inhibition halos were observed in several cases, while in others no inhibition halos were detected (see Figure 55). It is important to mention that the positive control generates adequate inhibition halos, therefore, the seeding and disk fixation process was successfully carried out. This observation is directly related to the nature of the culture medium used, specifically Mueller-Hinton (MH) agar, which has a semisolid consistency. Consequently, the diffusion capacity of the hybrid catalyst was affected, preventing its proper dispersion through the medium. Since, in photocatalysis, the oxidation and reduction process crucially depend on the formation of an interface between the catalyst and the medium, the limitation in the diffusion of the catalyst resulted in the absence or formation of significantly reduced inhibition halos. This phenomenon reveals the critical importance of proper diffusion of the catalyst in the culture medium for an accurate assessment of antibacterial activity. For this reason, there is a clear need to carry out the process in liquid media, which leads to the approach of a bacterial disinfection analysis by studying the turbidity of a liquid medium.

Figure 55. Antibacterial activity: Disk-diffusion assay

4.9.2. Absorbance analysis using UV-VIS spectroscopy

In the bacterial disinfection experiment using UV-Vis turbidity analysis, it is observed in Figure 56 that the culture medium in the presence of the hybrid catalyst (black color curve) shows a gradual increase in absorbance over time, reaching a value of 0.26 in a period of 5 hours. On the other hand, the positive control shows a more pronounced increase in absorbance (blue color curve), reaching 0.55 in the same period of time. With respect to the negative control (ampicillin), a total inhibition of growth is observed, except in the time interval from 120 minutes to 160 minutes. This is due to the fact that, in that time period, *E. coli* is at its maximum growth potential. This same phenomenon is observed in the positive control and in the hybrid catalyst medium. Finally, the negative control medium (green curve) shows that the medium is not contaminated, and therefore there is no increase in turbidity in any period.

This contrast in absorbance levels indicates that the hybrid catalyst significantly inhibits bacterial growth, with a reduction of 52.73% compared to the positive control. The mechanism of action of the catalyst demonstrates that the radicals formed in the culture medium diffuse until they interact with the DNA of the *E. coli* protozoan, causing its decomposition and, consequently, the death of the bacteria because they cannot regenerate. This result is highly promising, suggesting that the catalyst has an effective bactericidal effect.
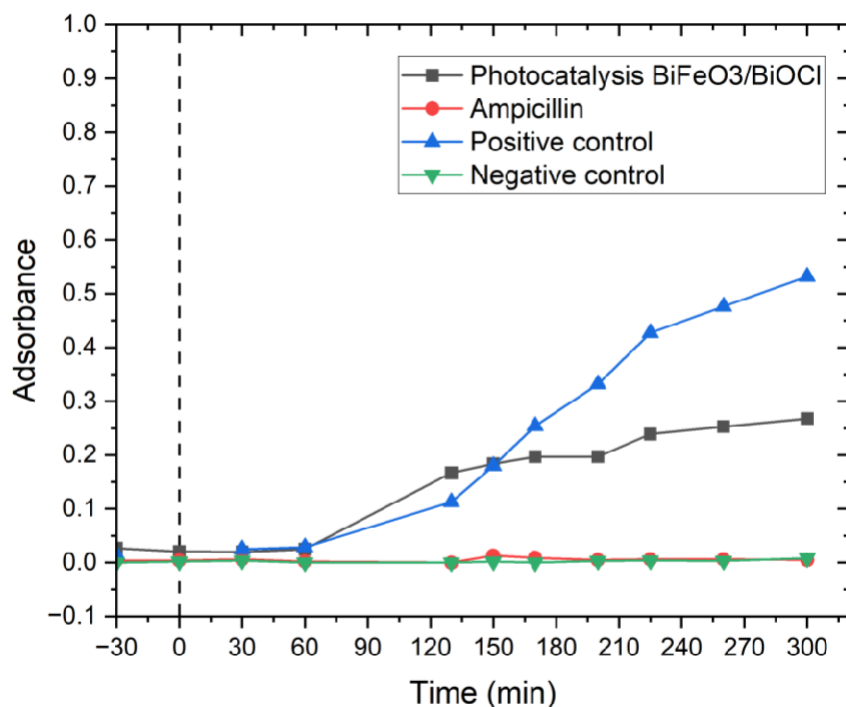
Figure 56. Antibacterial activity: Absorbance analysis using UV-VIS spectroscopy

After each set time point, samples of the culture medium were taken and micro dilutions were performed, followed by seeding on agar plates to observe bacterial growth. After an incubation period, it was observed that on none of the plates was the number of colonies greater than 30, indicating that the presence of these colonies is not significant. In other words, the bacterial disinfection is totally effective, where the bacterial count was reduced to 9.1×10^7 UFC, showing a total decrease in the number of bacteria present. This evidence confirms the efficacy of the hybrid catalyst treatment in bacterial degradation (Figure 57).

Figure 57. E. coli seeding by microdilutions from the degraded product

4.10. Cytotoxicity of the hybrid catalyst BiFeO$_3$/BiOCl

The results obtained from the present technique can be seen in Figure 58. It can be observed that the negative control showed the absence of contamination in all cases and validated the proper execution of the experiment, while the positive control showed normal cell growth, without the presence of external agents that inhibited such growth. However, the most interesting finding is that it was observed that the samples containing the hybrid catalyst, both activated and deactivated, exhibited even greater cell growth than the positive control. This phenomenon suggests that the hybrid catalyst does not exhibit cytotoxicity, as it cannot cross the cell membrane or the nucleus to degrade DNA. Instead, it is postulated that the catalyst acts as a mitogen, stimulating cell reproduction in a non-specific manner.

On the other hand, analyzing the samples containing the hybrid catalyst, a slight decrease in cell growth was observed in the presence of the irradiated catalyst, which could be attributed to the possible formation of chlorine during the process of decomposition of BiOCl. These results suggest that the hybrid catalyst could have promising applications in stimulating cell proliferation, although it is essential to consider possible side effects, such as chlorine formation, when using the irradiated catalyst.
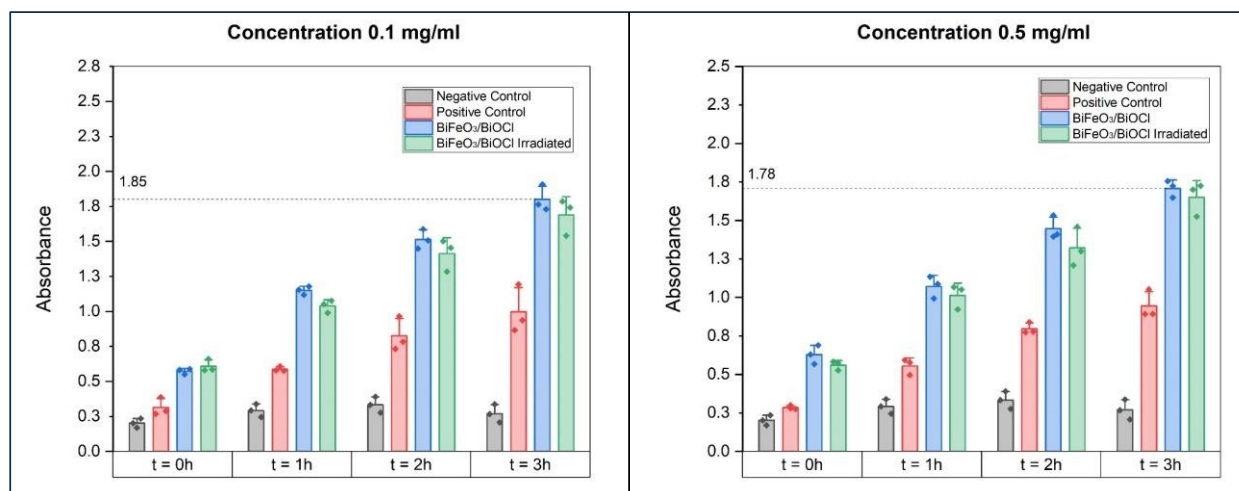
Figure 58. Cytotoxicity of the hybrid catalyst BiFeO$_3$/BiOCl

4.11. Determination of ROS species

The evaluation of ROS using scavengers has demonstrated that the photo-piezo catalysis reaction with the hybrid catalyst loses its effect when AgNO$_3$ and tert-butanol are used. These scavengers are specific for capturing electrons and superoxide radicals, respectively. This indicates that the reaction primarily occurs through the formation of superoxide radicals from oxygen molecules in the presence of electrons. On the other hand, the scavengers 2-propanol and

formic acid, which are specific for hydroxyl radicals and positive holes, respectively, show that hydroxyl radicals have a moderate involvement in the reaction. However, by inhibiting positive holes, the reaction rate improves, leading to the conclusion that the reaction does not proceed through positive holes or hydroxyl radicals.
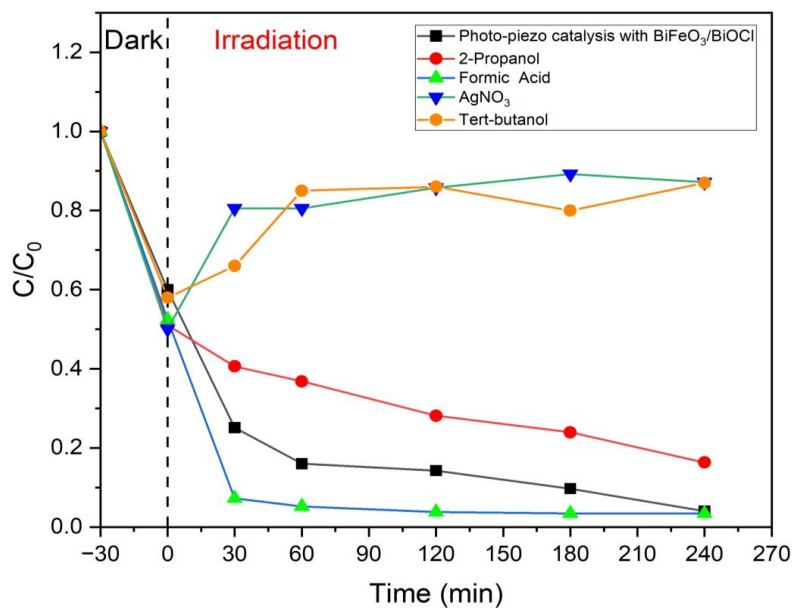
Figure 59. *Determination of ROS species by scavengers test.*

CHAPTER 5. CONCLUSIONS

- The applied characterization techniques validated the structure, morphology, and properties of both the precursors and the synthesized hybrid material. This thorough confirmation ensures that the developed hybrid possesses the necessary characteristics for the intended applications, affirming its suitability and potential effectiveness in real-world scenarios.

- The catalytic efficiency of the hybrid for Rhodamine B degradation was determined to be optimal at pH conditions below 4. This finding indicates that the hybrid catalyst is especially effective in acidic media, making it particularly suitable for applications where low pH conditions are prevalent, thereby expanding its utility in various industrial and environmental processes.

- The hybrid photo-piezocatalyst demonstrated significantly higher efficiency compared to its individual precursors. This result underscores the advantage of using a hybrid material, as the combination of different components enhances the overall catalytic performance, providing a more effective solution than the sum of its parts.

- The photo-piezo catalysis performed by the hybrid was found to be superior to both photocatalysis and piezocatalysis executed by the hybrid alone. This superiority highlights the synergistic effect achieved by integrating both catalytic processes into a single hybrid system, resulting in a more efficient and effective catalytic reaction.

- The hybrid material demonstrated effective antibacterial activity against *Escherichia coli*. This capability suggests its potential use in applications requiring antimicrobial properties, such as water purification, medical devices, and coatings, contributing to improved health and safety outcomes.

- Cytotoxicity testing revealed that the hybrid is not cytotoxic, which is crucial for its potential use in biomedical and environmental applications. The non-toxic nature of the hybrid material ensures its safety for use in various settings, including those involving direct or indirect contact with living organisms, thereby broadening its applicability and acceptance.

- The study shows that the photo-piezo catalysis reaction with the hybrid catalyst is primarily driven by superoxide radicals formed in the presence of electrons, with hydroxyl radicals

playing a minor role. The reaction rate improves when positive holes are inhibited, indicating they are not key agents in the reaction. Therefore, the main mechanism involves superoxide radicals, underscoring their importance in the catalytic process.

BIBLIOGRAPHY

[1]   M. A. Bañares and M. Daturi, 'Understanding catalysts by time-/space-resolved operando methodologies', *Catal Today*, vol. 423, 2023, doi: 10.1016/j.cattod.2023.114255.

[2]   Z.-Z. Shen, Y.-Z. Zhang, C. Zhou, R. Wen, and L.-J. Wan, 'Revealing the Correlations between Morphological Evolution and Surface Reactivity of Catalytic Cathodes in Lithium-Oxygen Batteries', *J Am Chem Soc*, vol. 143, no. 51, pp. 21604–21612, 2021, doi: 10.1021/jacs.1c09700.

[3]   K. P. Bhatt, S. Patel, D. S. Upadhyay, and R. N. Patel, 'In-depth analysis of the effect of catalysts on plasma technologies for treatment of various wastes', *J Environ Manage*, vol. 344, 2023, doi: 10.1016/j.jenvman.2023.118335.

[4]   R. Hu *et al.*, 'Recent advances of monoelemental 2D materials for photocatalytic applications', *J Hazard Mater*, vol. 405, 2021, doi: 10.1016/j.jhazmat.2020.124179.

[5]   I. Ahmad, M. A. Aftab, A. Fatima, S. D. Mekkey, S. Melhi, and S. Ikram, 'A comprehensivereview on the advancement of transition metals incorporated on functional magnetic nanocomposites for the catalytic reduction and photocatalytic degradation of organic pollutants', *Coord Chem Rev*, vol. 514, 2024, doi: 10.1016/j.ccr.2024.215904.

[6]   R. Asahi, T. Morikawa, T. Ohwaki, K. Aoki, and Y. Taga, 'Visible-light photocatalysis in nitrogen-doped titanium oxides', *Science (1979)*, 2001, doi: 10.1126/science.1061051.

[7]   Q. Yuan *et al.*, 'Selective Adsorption and Photocatalytic Degradation of Extracellular Antibiotic Resistance Genes by Molecularly-Imprinted Graphitic Carbon Nitride', *Environ Sci Technol*, vol. 54, no. 7, pp. 4621–4630, 2020, doi: 10.1021/acs.est.9b06926.

[8]   D. Chatterjee and S. Dasgupta, 'Visible light induced photocatalytic degradation of organic pollutants', *Journal of Photochemistry and Photobiology C: Photochemistry Reviews*, vol. 6, no. 2–3. 2005. doi: 10.1016/j.jphotochemrev.2005.09.001.

[9]   A. Ali, L. Chen, M. S. Nasir, C. Wu, B. Guo, and Y. Yang, 'Piezocatalytic removal of waterbacteria and organic compounds: a review', *Environ Chem Lett*, vol. 21, no. 2, pp. 1075– 1092, 2023, doi: 10.1007/s10311-022-01537-3.

[10]   X. Xue *et al.*, 'Piezo-potential enhanced photocatalytic degradation of organic dye using ZnOnanowires', *Nano Energy*, vol. 13, pp. 414–422, 2015, doi: 10.1016/j.nanoen.2015.02.029.

[11]   Y. Hu, C. Pan, and Z. L. Wang, 'Recent progress in piezo-phototronics with extended

materials, application areas and understanding', *Semicond Sci Technol*, vol. 32, no. 5, 2017, doi: 10.1088/1361-6641/aa642e.

[12] K. Wang, C. Han, J. Li, J. Qiu, J. Sunarso, and S. Liu, 'The Mechanism of Piezocatalysis: Energy Band Theory or Screening Charge Effect?', *Angewandte Chemie - International Edition*, vol. 61, no. 6. 2022. doi: 10.1002/anie.202110429.

[13] X. Li, J. Yu, and C. Jiang, 'Principle and surface science of photocatalysis', in *Interface Science and Technology*, vol. 31, 2020. doi: 10.1016/B978-0-08-102890-2.00001-4.

[14] H. Wang *et al.*, 'A review on heterogeneous photocatalysis for environmental remediation: From semiconductors to modification strategies', *Chinese Journal of Catalysis*, vol. 43, no.2. 2022. doi: 10.1016/S1872-2067(21)63910-4.

[15] S. Dubey *et al.*, 'Photo/piezo-catalytic performance of $0.5Ba(Zr_{0.2}Ti_{0.8})O_3$-$0.5(Ba_{0.7}Sr_{0.3})TiO_3$ ceramic', *Journal of MaterialsResearch and Technology*, vol. 23, pp. 1666–1679, 2023, doi: 10.1016/j.jmrt.2023.01.073.

[16] A. Hernández-Ramírez and I. Medina-Ramírez, *Photocatalytic semiconductors: Synthesis, characterization, and environmental applications*. 2015. doi: 10.1007/978-3-319-10999-2.

[17] M. Liu, Y. Yi, L. Wang, H. Guo, and A. Bogaerts, 'Hydrogenation of carbon dioxide to value-added chemicals by heterogeneous catalysis and plasma catalysis', *Catalysts*, vol. 9, no. 3, 2019, doi: 10.3390/catal9030275.

[18] V. Augugliaro, G. Palmisano, L. Palmisano, and J. Soria, 'Heterogeneous photocatalysis andcatalysis: An overview of their distinctive features', *Heterogeneous Photocatalysis: Relationships with Heterogeneous Catalysis and Perspectives*, no. January, pp. 1–24, 2019, doi: 10.1016/B978-0-444-64015-4.00001-8.

[19] P. Kumar *et al.*, 'Effect of Poling on Photocatalysis, Piezocatalysis, and Photo–Piezo Catalysis Performance of $BaBi_4Ti_4O_{15}$ Ceramics', *Global Challenges*, vol. 7, no. 2, 2023, doi: 10.1002/gch2.202200142.

[20] S. Garcia-Segura and E. Brillas, 'Applied photoelectrocatalysis on the degradation of organicpollutants in wastewaters', *Journal of Photochemistry and Photobiology C: PhotochemistryReviews*, vol. 31, pp. 1–35, 2017, doi: 10.1016/j.jphotochemrev.2017.01.005.

[21] K. Chen, J. Liang, Y. Wang, Y. Tao, Y. Lu, and A. Wang, 'A global perspective on microbialrisk factors in effluents of wastewater treatment plants', *J Environ Sci (China)*, vol. 138, pp.

227–235, 2024, doi: 10.1016/j.jes.2023.04.012.

[22]   K. Pullerits *et al.*, 'Impact of UV irradiation at full scale on bacterial communities in drinkingwater', *NPJ Clean Water*, vol. 3, no. 1, pp. 1–10, 2020, doi: 10.1038/s41545-020-0057-7.

[23]   D. Tuba-Guaman *et al.*, 'Photodegradation of Rhodamine B and Bisphenol A Over Visible-Light Driven Bi7O9I3-and Bi12O17Cl2-Photocatalysts Under White LED Irradiation', *TopCatal*, vol. 65, no. 9–12, pp. 1028–1044, Aug. 2022, doi: 10.1007/s11244-022-01689-0.

[24]   T. Soltani and M. H. Entezari, 'Sono-synthesis of bismuth ferrite nanoparticles with high photocatalytic activity in degradation of Rhodamine B under solar light irradiation', *Chemical Engineering Journal*, vol. 223, pp. 145–154, May 2013, doi: 10.1016/j.cej.2013.02.124.

[25]   L. Yang *et al.*, 'A P25/(NH4)xWO3hybrid photocatalyst with broad spectrum photocatalyticproperties under UV, visible, and near-infrared irradiation', *Sci Rep*, vol. 8, Apr. 2017, doi: 10.1038/srep45715.

[26]   H. Ma, Y. Ding, P. Wang, and S. Zhou, 'Efficient removal for antibiotic-resistant Escherichiacoli and antibiotic resistance genes from aquatic environment by BiOCl supported Ag quantum dots', *J Photochem Photobiol A Chem*, vol. 444, 2023, doi: 10.1016/j.jphotochem.2023.114998.

[27]   A. G. Rincón and C. Pulgarin, 'Photocatalytical inactivation of E. coli: Effect of (continuous-intermittent) light intensity and of (suspended-fixed) TiO 2 concentration', *Appl Catal B*, 2003, doi: 10.1016/S0926-3373(03)00076-6.

[28]   Y. Yang *et al.*, 'Damage dynamics and the role of chance in the timing of E. coli cell death', *Nat Commun*, vol. 14, no. 1, 2023, doi: 10.1038/s41467-023-37930-x.

[29]   A. K. Biń and S. Sobera-Madej, 'Comparison of the Advanced Oxidation Processes (UV, UV/H 2O 2 and O 3) for the Removal of Antibiotic Substances during Wastewater Treatment', *Ozone Sci Eng*, vol. 34, no. 2, pp. 136–139, Mar. 2012, doi: 10.1080/01919512.2012.650130.

[30]   C. Theresa Thomas, 'Photocatalytic treatment of biological organisms in water using graphene oxide doped TiO2 and BiVO4 nanocomposites'. [Online]. Available: https://theses.hal.science/tel-03666769

[31]   P. Fernández-Castro, M. Vallejo, M. F. San Román, and I. Ortiz, 'Insight on the fundamentals of advanced oxidation processes: Role and review of the determination

methods of reactive oxygen species', *Journal of Chemical Technology and Biotechnology*, vol. 90, no. 5. John Wiley and Sons Ltd, pp. 796–820, May 01, 2015. doi: 10.1002/jctb.4634.

[32] E. Domingues, M. J. Silva, T. Vaz, J. Gomes, and R. C. Martins, 'Persulfate process activated by homogeneous and heterogeneous catalysts for synthetic olive mill wastewater treatment', *Water (Switzerland)*, vol. 13, no. 21, 2021, doi: 10.3390/w13213010.

[33] X. Liu *et al.*, 'A review on percarbonate-based advanced oxidation processes for remediation of organic compounds in water', *Environ Res*, vol. 200, 2021, doi: 10.1016/j.envres.2021.111371.

[34] M. Náfrádi, T. Hlogyik, L. Farkas, and T. Alapi, 'Comparison of the heterogeneous photocatalysis of imidacloprid and thiacloprid – reaction mechanism, ecotoxicity, and the effect of matrices', *J Environ Chem Eng*, vol. 9, no. 6, 2021, doi: 10.1016/j.jece.2021.106684.

[35] S. Najafishirtari *et al.*, 'A Perspective on Heterogeneous Catalysts for the Selective Oxidation of Alcohols', *Chemistry - A European Journal*, vol. 27, no. 68, pp. 16809–16833, 2021, doi: 10.1002/chem.202102868.

[36] S. E. Braslavsky *et al.*, 'Glossary of terms used in photocatalysis and radiation catalysis (IUPAC recommendations 2011)', *Pure and Applied Chemistry*, 2011, doi: 10.1351/PAC- REC-09-09-36.

[37] F. Pita Oscar Alexander, M. Caetano, and A. Palma, 'UNIVERSIDAD DE INVESTIGACIÓN DE TECNOLOGÍA EXPERIMENTAL YACHAY TECH Escuela de Ciencias Químicas e Ingeniería Virtual Modeling and Design of an Optimal Light Emitting Diodes-based Photocatalyst Test System Trabajo de integración curricular presentado como requisito para la obtención del título de Petroquímico'.

[38] R. L. Doyle, I. J. Godwin, M. P. Brandon, and M. E. G. Lyons, 'Redox and electrochemical water splitting catalytic properties of hydrated metal oxide modified electrodes', *Physical Chemistry Chemical Physics*, vol. 15, no. 33. 2013. doi: 10.1039/c3cp51213d.

[39] M. E. Simonsen, 'Heterogeneous Photocatalysis', in *Chemistry of Advanced Environmental Purification Processes of Water: Fundamentals and Applications*, 2014. doi: 10.1016/B978-0-444-53178-0.00004-3.

[40] G. Mamba and A. K. Mishra, 'Graphitic carbon nitride (g-C3N4) nanocomposites: A new and exciting generation of visible light driven photocatalysts for environmental pollution remediation', *Applied Catalysis B: Environmental*, vol. 198. Elsevier B.V., pp. 347–377,

Dec. 05, 2016. doi: 10.1016/j.apcatb.2016.05.052.

[41] A. O. Ibhadon and P. Fitzpatrick, 'Heterogeneous photocatalysis: Recent advances and applications', *Catalysts*, vol. 3, no. 1. 2013. doi: 10.3390/catal3010189.

[42] J. Borsovszky *et al.*, 'Photodissociation of dicarbon: How nature breaks an unusual multiplebond', *Proc Natl Acad Sci U S A*, vol. 118, no. 52, 2021, doi: 10.1073/pnas.2113315118.

[43] S. K. Kuila, R. Sarkar, P. Kumbhakar, P. Kumbhakar, C. S. Tiwary, and T. K. Kundu, 'Photocatalytic dye degradation under sunlight irradiation using cerium ion adsorbed two- dimensional graphitic carbon nitride', *J Environ Chem Eng*, vol. 8, no. 4, 2020, doi:10.1016/j.jece.2020.103942.

[44] Y. Franco, G. Centeno Bordones, and J. Pereira, 'Estado del arte. Pinturas fotocatalíticas para la descontaminación del aire', *Revista Ingeniería UC*, vol. 29, no. 3, pp. 233–253, Apr.2023, doi: 10.54139/revinguc.v29i3.286.

[45] M. A. Bañares and M. Daturi, 'Understanding catalysts by time-/space-resolved operando methodologies', *Catal Today*, vol. 423, 2023, doi: 10.1016/j.cattod.2023.114255.

[46] K. P. Bhatt, S. Patel, D. S. Upadhyay, and R. N. Patel, 'In-depth analysis of the effect of catalysts on plasma technologies for treatment of various wastes', *J Environ Manage*, vol. 344, 2023, doi: 10.1016/j.jenvman.2023.118335.

[47] H. Ren, P. Koshy, W. F. Chen, S. Qi, and C. C. Sorrell, 'Photocatalytic materials and technologies for air purification', *Journal of Hazardous Materials*, vol. 325. Elsevier B.V., pp. 340–366, 2017. doi: 10.1016/j.jhazmat.2016.08.072.

[48] L. Zhang, Z. K. Tang, W. M. Lau, W. J. Yin, S. X. Hu, and L. M. Liu, 'Tuning band gaps and optical absorption of BiOCl through doping and strain: Insight form DFT calculations',*Physical Chemistry Chemical Physics*, vol. 19, no. 31, pp. 20968–20973, 2017, doi: 10.1039/c7cp03276e.

[49] J. Lu, W. Zhou, X. Zhang, and G. Xiang, 'Electronic Structures and Lattice Dynamics of Layered BiOCl Single Crystals', *Journal of Physical Chemistry Letters*, vol. 11, no. 3, pp. 1038–1044, Feb. 2020, doi: 10.1021/acs.jpclett.9b03575.

[50] H. Li *et al.*, 'A recyclable photocatalytic tea-bag-like device model based on ultrathin Bi/C/BiOX (X = Cl, Br) nanosheets', *Appl Surf Sci*, vol. 515, Jun. 2020, doi: 10.1016/j.apsusc.2020.145967.

[51]   Y. Wu *et al.*, 'Mechanism insights into the facet-dependent photocatalytic degradation of perfluorooctanoic acid on BiOCl nanosheets', *Chemical Engineering Journal*, vol. 425, Dec.2021, doi: 10.1016/j.cej.2021.130672.

[52]   M. Liu, H. Zhu, N. Zhu, and Q. Yu, 'Vacancy engineering of BiOCl microspheres for efficient removal of multidrug-resistant bacteria and antibiotic-resistant genes in wastewater', *Chemical Engineering Journal*, vol. 426, Dec. 2021, doi: 10.1016/j.cej.2021.130710.

[53]   Y. Zhang *et al.*, 'Unveiling the activity origin of ultrathin BiOCl nanosheets for photocatalytic CO2 reduction', *Appl Catal B*, vol. 299, Dec. 2021, doi: 10.1016/j.apcatb.2021.120679.

[54]   H. Yu and Q. Han, 'Effect of reaction mediums on photocatalytic performance of BiOX (X = Cl, Br, I)', *Opt Mater (Amst)*, vol. 119, Sep. 2021, doi: 10.1016/j.optmat.2021.111399.

[55]   F. Bößl and I. Tudela, 'Piezocatalysis: Can catalysts really dance?', *Current Opinion in Green and Sustainable Chemistry*, vol. 32. Elsevier B.V., Dec. 01, 2021. doi: 10.1016/j.cogsc.2021.100537.

[56]   G. Yang *et al.*, 'Cocatalyst Engineering in Piezocatalysis: A Promising Strategy for BoostingHydrogen Evolution', *ACS Appl Mater Interfaces*, vol. 13, no. 13, pp. 15305–15314, Apr. 2021, doi: 10.1021/acsami.1c01550.

[57]   Y. Wang *et al.*, 'Piezo-catalysis for nondestructive tooth whitening', *Nat Commun*, vol. 11, no. 1, Dec. 2020, doi: 10.1038/s41467-020-15015-3.

[58]   G. Yang *et al.*, 'Supporting Information Cocatalyst Engineering in Piezocatalysis: A Promising Strategy for Boosting Hydrogen Evolution'.

[59]   H. You *et al.*, 'Harvesting the Vibration Energy of BiFeO3 Nanosheets for Hydrogen Evolution', *Angewandte Chemie - International Edition*, vol. 58, no. 34, pp. 11779–11784, Aug. 2019, doi: 10.1002/anie.201906181.

[60]   S. Li, Z. Zhao, J. Zhao, Z. Zhang, X. Li, and J. Zhang, 'Recent Advances of Ferro-, Piezo-, and Pyroelectric Nanomaterials for Catalytic Applications', *ACS Applied Nano Materials*, vol. 3, no. 2. American Chemical Society, pp. 1063–1079, Feb. 28, 2020. doi: 10.1021/acsanm.0c00039.

[61]   F. Han *et al.*, 'Photocurrent and dielectric/ferroelectric properties of $KNbO_3$–$BaFeO_{3-\delta}$ ferroelectric semiconductors', *Ceram Int*, vol. 46, no. 10, pp. 14567–

14572, 2020, doi: 10.1016/j.ceramint.2020.02.256.

[62] G. S. Lotey and N. K. Verma, 'Synthesis and characterization of BiFeO<inf>3</inf> nanowires and their applications in dye-sensitized solar cells', *Mater Sci Semicond Process*,vol. 21, no. 1, pp. 206–211, 2014, doi: 10.1016/j.mssp.2013.11.029.

[63] A. Nourdine, M. Abdelli, N. Charvin, and L. Flandin, 'Custom synthesis of zno nanowires for efficient ambient air-processed solar cells', *ACS Omega*, vol. 6, no. 48, pp. 32365–32378, 2021, doi: 10.1021/acsomega.1c01654.

[64] M. Hassan, L. Jiaji, P. Lee, and R. S. Rawat, 'Catalyst free growth of ZnO thin film nanostructures on Si substrate by thermal evaporation', *Appl Phys A Mater Sci Process*, vol.127, no. 7, 2021, doi: 10.1007/s00339-021-04650-2.

[65] J. Wu, W. Li, S. Guan, X. Chen, H. Gao, and X. Liu, 'Study on the performance of vanadiumdoped NaNbO<inf>3</inf> photocatalyst degradation antibiotics', *Inorg Chem Commun*, vol. 131, 2021, doi: 10.1016/j.inoche.2021.108669.

[66] M. Cernea *et al.*, 'Structural, electrical properties and photoluminescence analyses of the terbium doped barium titanate', *J Alloys Compd*, vol. 878, 2021, doi: 10.1016/j.jallcom.2021.160380.

[67] E. B. Yakimov, E. E. Yakimov, and A. N. Redkin, 'Effect of Electron-Beam Irradiation on the Cathodoluminescence of a ZnO Nanorod Array', *Journal of Surface Investigation*, vol. 15, no. 6, pp. 1208–1211, 2021, doi: 10.1134/S1027451021050219.

[68] Y. Feng *et al.*, 'Enhanced Photocatalytic Degradation Performance by Fluid-Induced Piezoelectric Field', *Environ Sci Technol*, vol. 52, no. 14, pp. 7842–7848, Jul. 2018, doi: 10.1021/acs.est.8b00946.

[69] C.-H. Chou, S.-Y. Lee, and K.-S. Chang, 'High-density ZnSnO<inf>3</inf> nanowire arraysfabricated using single-step hydrothermal synthesis', *Journal of the American Ceramic Society*, vol. 103, no. 8, pp. 4129–4139, 2020, doi: 10.1111/jace.17100.

[70] H. You *et al.*, 'Harvesting the Vibration Energy of BiFeO3 Nanosheets for Hydrogen Evolution', *Angewandte Chemie - International Edition*, vol. 58, no. 34, pp. 11779–11784, Aug. 2019, doi: 10.1002/anie.201906181.

[71] M. Wang *et al.*, 'Remarkably Enhanced Hydrogen Generation of Organolead Halide Perovskites via Piezocatalysis and Photocatalysis', *Adv Energy Mater*, vol. 9, no. 37, Oct. 2019, doi: 10.1002/aenm.201901801.

[72] C. Hu, H. Huang, F. Chen, Y. Zhang, H. Yu, and T. Ma, 'Coupling Piezocatalysis and Photocatalysis in Bi4NbO8X (X = Cl, Br) Polar Single Crystals', *Adv Funct Mater*, vol. 30, no. 7, Feb. 2020, doi: 10.1002/adfm.201908168.

[73] H. You *et al.*, 'Harvesting the Vibration Energy of BiFeO3 Nanosheets for Hydrogen Evolution', *Angewandte Chemie - International Edition*, vol. 58, no. 34, pp. 11779–11784, Aug. 2019, doi: 10.1002/anie.201906181.

[74] Z.-B. Wang, A. Aldalbahi, T. Ahamad, S. M. Alshehri, and P. X. Feng, 'Preparation of BiFeO$_3$ and its photoelectric performance as photoanode of DSSC', *Ceram Int*, vol. 47, no. 19, pp. 27565–27570, 2021, doi: 10.1016/j.ceramint.2021.06.180.

[75] B. M. Al-Maswari *et al.*, 'Synthesis of perovskite bismuth ferrite embedded nitrogen-doped Carbon (BiFeO$_3$-NC) nanocomposite for energy storage application', *J Energy Storage*, vol. 44, 2021, doi: 10.1016/j.est.2021.103515.

[76] Y. Hu, C. Pan, and Z. L. Wang, 'Recent progress in piezo-phototronics with extended materials, application areas and understanding', *Semicond Sci Technol*, vol. 32, no. 5, Apr. 2017, doi: 10.1088/1361-6641/aa642e.

[77] S. Tu *et al.*, 'Piezocatalysis and Piezo-Photocatalysis: Catalysts Classification and Modification Strategy, Reaction Mechanism, and Practical Application', *Advanced Functional Materials*, vol. 30, no. 48. Wiley-VCH Verlag, Nov. 01, 2020. doi: 10.1002/adfm.202005158.

[78] S. Verma, M. Sharma, and R. Vaish, 'Photo-piezocatalysis in electrospun PVDF + WS2 membrane', *Environ Sci Nano*, vol. 9, no. 10, pp. 3885–3899, Sep. 2022, doi: 10.1039/d2en00699e.

[79] C. Yu *et al.*, 'Selective Enhancement of Photo-Piezocatalytic Performance in BaTiO3 Via heterovalent Ion Doping', *Adv Funct Mater*, vol. 32, no. 52, Dec. 2022, doi: 10.1002/adfm.202209365.

[80] C. Yu *et al.*, 'Selective Enhancement of Photo-Piezocatalytic Performance in BaTiO3 Via heterovalent Ion Doping', *Adv Funct Mater*, vol. 32, no. 52, Dec. 2022, doi: 10.1002/adfm.202209365.

[81] J. Liang *et al.*, 'Ultrasonic-enhanced photocatalysis through piezoelectric and cavitation effects for lignin depolymerization', *Int J Biol Macromol*, vol. 264, 2024, doi: 10.1016/j.ijbiomac.2024.130526.

[82]   S. Zhong *et al.*, 'Improved piezo-photocatalysis for aquatic multi-pollutant removal via BiOBr/BaTiO$_3$ heterojunction construction', *Chemical Engineering Journal*, vol. 488, 2024, doi: 10.1016/j.cej.2024.151002.

[83]   H. Gao *et al.*, 'Dissolved oxygen enhanced piezo-photocatalytic performance in Ag dots- modified BaTiO$_3$ nanoparticles for efficient degradation of multiple organic pollutants', *Sep Purif Technol*, vol. 346, 2024, doi: 10.1016/j.seppur.2024.127548.

[84]   L. Zhou *et al.*, 'Recent Advances in Piezocatalysts for Dye Degradation', *Adv Sustain Syst*, 2024, doi: 10.1002/adsu.202300652.

[85]   S. Li, X. Zhang, F. Yang, J. Zhang, W. Shi, and F. Rosei, 'Mechanically driven water splitting over piezoelectric nanomaterials', *Chem Catalysis*, vol. 4, no. 2, 2024, doi: 10.1016/j.checat.2024.100901.

[86]   A. Studer and D. P. Curran, 'Catalysis of Radical Reactions: A Radical Chemistry Perspective', *Angewandte Chemie - International Edition*, vol. 55, no. 1. 2016. doi: 10.1002/anie.201505090.

[87]   H. Li *et al.*, 'A recyclable photocatalytic tea-bag-like device model based on ultrathin Bi/C/BiOX (X = Cl, Br) nanosheets', *Appl Surf Sci*, vol. 515, 2020, doi: 10.1016/j.apsusc.2020.145967.

[88]   N. Adhlakha and K. L. Yadav, 'Structural, dielectric, magnetic, and optical properties of Ni 0.75Zn0.25Fe2O4-BiFeO3 composites', *J Mater Sci*, vol. 49, no. 13, pp. 4423–4438, 2014, doi: 10.1007/s10853-014-8139-x.

[89]   E. Abdelkader, L. Nadjia, B. Naceur, and L. Favier-Teodorescu, 'Thermal, structural and optical properties of magnetic BiFeO3 micron-particles synthesized by coprecipitationmethod: heterogeneous photocatalysis study under white LED irradiation', *Ceramica*, vol. 68, no. 385, pp. 84–96, 2022, doi: 10.1590/0366-69132022683853181.

[90]   Z. S. Seddigi *et al.*, 'Facile synthesis of light harvesting semiconductor bismuth oxychloridenano photo-catalysts for efficient removal of hazardous organic pollutants', *PLoS One*, vol. 12, no. 2, Feb. 2017, doi: 10.1371/journal.pone.0172218.

[91]   W. Tang, Y. Zhang, H. Guo, and Y. Liu, 'Heterogeneous activation of peroxymonosulfate for bisphenol AF degradation with BiOI0.5Cl0.5', *RSC Adv*, vol. 9, no. 25, pp. 14060–14071, 2019, doi: 10.1039/c9ra01687b.

[92]   E. J. Rivera *et al.*, 'Bismuth@US-tubes as a potential contrast agent for X-ray imaging

applications', *J Mater Chem B*, vol. 1, no. 37, pp. 4792–4800, Oct. 2013, doi:10.1039/c3tb20742k.

[93] C. C. Chen and T. Fan, 'Study on carbon quantum dots/BiFeO3 heterostructures and their enhanced photocatalytic activities under visible light irradiation', *Journal of Materials Science: Materials in Electronics*, vol. 28, no. 14, pp. 10019–10027, Jul. 2017, doi: 10.1007/s10854-017-6760-6.

[94] M. Arunkumar, S. Veerakumar, V. Mohanavel, J. Vairamuthu, V. Vijayan, and N. Senthilkumar, 'A Novel Visible Light-Driven p-Type BiFeO$_3$/n-Type SnS$_2$ Heterojunction Photocatalyst for Efficient Charge Separation and Enhanced Photocatalytic Activity', *J Clust Sci*, vol. 32, no. 5, pp. 1431–1439, 2021, doi: 10.1007/s10876-021-02114-4.

[95] G. S. Pawar and A. A. Tahir, 'Unbiased Spontaneous Solar Fuel Production using Stable la FeO$_3$ Photoelectrode', *Sci Rep*, vol. 8, no. 1, 2018, doi: 10.1038/s41598-018- 21821-z.

[96] J. Stephenson, V. Celorrio, D. Tiwari, S. R. Hall, D. C. Green, and D. J. Fermín, 'Photoelectrochemical properties of BiOCl microplatelets', *Journal of Electroanalytical Chemistry*, vol. 819, pp. 171–177, Jun. 2018, doi: 10.1016/j.jelechem.2017.10.024.

[97] A. P. Chowdhury and B. H. Shambharkar, 'Synthesis and characterization of BiOCl– Cu2ZnSnS4 heterostructure with enhanced photocatalytic activity', *Appl Water Sci*, vol. 8, no. 7, Nov. 2018, doi: 10.1007/s13201-018-0853-0.

ANNEX